UNIVERSITAT POLITÈCNICA
DE CATALUNYA
BARCELONATECH

Environmentally friendly nanocrystals synthesized and processed in ambient conditions for solution-processed solar cells

M. Zafer Akgul

Environmentally friendly nanocrystals synthesized and processed in ambient conditions for solution-processed solar cells

M. Zafer Akgul

ICFO - The Institute of Photonic Sciences
Barcelona, 2020

Environmentally friendly nanocrystals synthesized and processed in ambient conditions for solution-processed solar cells

M. Zafer Akgul

under the supervision of

Professor Gerasimos Konstantatos

submitted this thesis in partial fulfillment
of the requirements for the degree of

Doctor

by the

Universitat Politècnica de Catalunya
Barcelona, 2020

To my family and all the people,
who made this work possible

Abstract

Due to the continuously increasing energy demand and the environmental concerns about climate changes raised by international community, alternative energy resources have been put under intense investigation for the past decade. As a consequence, different technologies have been proposed, photovoltaics being a promising one among them. Till now, different structures and methods have been employed to fabricate photovoltaics for energy production. Traditionally, vacuum-based deposition methods have been used to form the stacks required for proper photovoltaic operation. Triggered by the advancements in colloidal synthesis methods, thin films of colloidal semiconductor nanocrystals (CNCs) have gained tremendous attention as cheap substitutes for vacuum-deposited layers. Up to date, various colloidal synthesis methods have been developed to produce semiconductor nanocrystals for applications in photovoltaics. Thanks to the high degree of controllability and high material quality, hot injection methods have been the way-to-go for the past decades. However, the application of CNC films in large-scale photovoltaics has been delayed due to the synthesis constraints originating from hot injection methods itself.

In this work, we demonstrate that it is possible to eliminate the need for air-free techniques by careful selection of the precursors and oxygen-aware design of reaction conditions. We use the semiconducting compound silver bismuth sulfide ($AgBiS_2$) as the prototype material to demonstrate the easiness and efficiency of the method. This semiconducting compound is selected as the prototype material thanks to its attractive optical properties for photovoltaics and the environmentally friendly nature of the constituent elements. Solar cells fabricated using CNCs synthesized at room temperature have yielded a power conversion efficiency of 5.5 %, demonstrating the promising potential of the method. The application of the method in the synthesis of $AgBiS_2$ CNCs results in a cost reduction of at least 60 % compared to the previous studies reporting similar photovoltaics-grade $AgBiS_2$ CNCs. Another important challenge in employing hot injection methods is the scalability. Due to the difficulties in maintaining the thermal fluctuations within the reaction volume low and in the maintenance of

inert atmosphere inside the reaction vessel, hot injection methods impose an inherent scale constraint on the synthesis. On the other hand, with the elimination of scale constraint by the use of an ambient condition synthesis method, the requirement for high temperature reaction and chemically inert reaction environment is eliminated, enabling us to achieve large-scale volume production of CNCs. This, in turn, can lower the production cost of CNCs further, hence the cost of photovoltaics that are based on CNCs. In addition, we show that the ambient condition method can be adapted for the synthesis of another metal chalcogenide, namely silver bismuth selenide CNCs ($AgBiSe_2$) with an extended absorption spectrum further into the near infrared down to ~ 0.9 eV. The resulting $AgBiSe_2$ CNC solar cells achieved a preliminary efficiency up to 2.6 %. Also, thanks to the structural similarity of these two compounds, the two methods that are developed for the synthesis of $AgBiS_2$ and $AgBiSe_2$ CNCs are combined and optimized to obtain alloyed quaternary AgBiSSe CNCs as a facile means of bandgap tuning in silver bismuth chalcogenide semiconductor family. The formation of AgBiSSe CNCs are verified through optical and structural characterization methods to show the formation of quaternary phase and also the phase purity of the obtained product. Overall, it is shown that the proposed ambient condition synthesis method is capable of providing photovoltaics-grade RoHS-compliant materials at a lower cost and higher throughput compared to the hot-injection based methods, opening a novel way for low-cost environmentally friendly photovoltaics.

Resumen

Debido al continuo aumento de la demanda de energía y las preocupaciones ambientales sobre el cambio climático planteadas por la comunidad internacional, los recursos energéticos alternativos han sido objeto de una intensa investigación durante la última década. Como consecuencia, se han propuesto diferentes tecnologías, siendo la fotovoltaica una prometedora entre ellas. Hasta ahora, se han empleado diferentes estructuras y métodos para fabricar células solares para la producción de energía. Tradicionalmente, se han utilizado métodos de deposición basados en vacío para formar las capas necesarias para el funcionamiento fotovoltaico adecuado. Debido a los avances en los métodos de síntesis coloidal, las películas finas de nanocristales semiconductores en solución coloidal (CNCs) han ganado una gran atención como sustitutos baratos de las capas depositadas al vacío. Hasta la fecha, se han desarrollado varios métodos de síntesis coloidal para producir nanocristales semiconductores para aplicaciones en energía fotovoltaica. Gracias al alto grado de controlabilidad y la alta calidad del material, los métodos de inyección en caliente han sido el camino a seguir durante las últimas décadas. Sin embargo, la aplicación de películas de CNCs en fotovoltaica a gran escala se ha retrasado debido a las propias limitaciones de estos métodos de síntesis.

En este trabajo, demostramos que es posible eliminar la necesidad de técnicas inertes mediante la selección cuidadosa de los precursores y el diseño de las condiciones de reacción conscientes del oxígeno. Usamos el compuesto semiconductor sulfuro de bismuto y plata ($AgBiS_2$) como material prototipo para demostrar la facilidad y eficiencia del método. Este compuesto semiconductor se ha seleccionado como material prototipo gracias a sus atractivas propiedades ópticas para la energía fotovoltaica y la naturaleza ecológica de los elementos constituyentes. Las células solares fabricadas con CNCs sintetizadas a temperatura ambiente han arrojado una eficiencia de conversión de energía del 5,5 %, lo que demuestra el potencial prometedor del método. La aplicación del método en la síntesis de CNCs de $AgBiS_2$ da como resultado una reducción de costes de al menos un 60 % en comparación con los estudios anteriores que reportaron CNCs

de $AgBiS_2$ de una calidad fotovoltaica similar. Otro desafío importante al emplear métodos de inyección en caliente es la escalabilidad. Debido a las dificultades para mantener bajas las fluctuaciones térmicas y la atmósfera inerte dentro del recipiente de reacción, los métodos de inyección en caliente imponen una restricción de escala inherente a la síntesis. Por otro lado, con la eliminación de la restricción de escala mediante el uso de un método de síntesis en condiciones ambientales, se elimina también el requisito de reacción a alta temperatura y entorno de reacción químicamente inerte, lo que nos permite lograr una producción en volumen a gran escala de CNCs. Esto, a su vez, puede reducir aún más el coste de producción de los CNCs, y en consecuencía el coste de las células fotovoltaicas que se basan en CNCs. Además, mostramos que el método en condiciones ambientales se puede adaptar para la síntesis de otro calcogenuro metálico, por ejemplo, CNCs de seleniuro de bismuto y plata ($AgBiSe_2$) con un espectro de absorción más extendido en el infrarrojo cercano, hasta ~ 0.9 eV . Las células solares de CNCs de $AgBiSe_2$ alcanzaron una eficiencia preliminar de hasta el 2,6 %. Además, gracias a la similitud estructural de estos dos compuestos, los dos métodos desarrollados para la síntesis de CNCs de $AgBiS_2$ y $AgBiSe_2$ se combinan y optimizan para obtener CNCs de la aleación cuaternaria AgBiSSe como un medio fácil de sintonización de bandgap en familia de semiconductores de calcogenuro de bismuto y plata. La formación de los CNCs de AgBiSSe se verifica mediante métodos de caracterización óptica y estructural para mostrar la formación de la fase cuaternaria y también la pureza de fase del producto obtenido. En general, se demuestra que el método de síntesis en condiciones ambientales propuesto es capaz de proporcionar materiales fotovoltaicos compatibles con RoHS a un coste menor y un mayor rendimiento en comparación con los métodos basados en inyección en caliente, lo que abre un camino novedoso para la energía fotovoltaica ecológica de bajo coste.

Acknowledgements

I am thankful to many people for this pleasant journey at ICFO. I have learned and improved myself a lot thanks to helpful and cheerful ICFOnians during the last 5 years. I want to use this opportunity to present my deepest gratitude to people who made this work possible directly or indirectly. This work would be incomplete without your contributions.

My deepest and most sincere gratitude goes to my supervisor, Gerasimos Konstantatos. Thanks to his deep knowledge, and of course patience toward non-working experiments, I always felt motivated. His guidance and patience made this project an enjoyable experience instead of a burden. Thanks for giving me this opportunity to discover the universe of photovoltaics!

Dear FON people, thanks for your continuous help and enlightening conversations. I would like to thank Nicky, Maria and Santanu for having introduced me to the curious universe of photovoltaics. To Alex, Ignasi, Yongjie and Zhouran and Alberto, who are/were my companions in facing the challenges in $AgBiS_2$ project. Thank you guys for always fruitful discussions and enlightening ideas. To Mariona, Shanti, Shuchi, Yu, Onur, Francesco, Iñigo, Guy, Biswajit, Sotirios and Nengjie for interesting lab talk and funny lunch conversations. To Shuchi, Niels, Anika, Niek, Callum and Richard, thanks for the endless fun and adventure at the weekend excursions. I will certainly miss that! I am grateful to my past and present office mates David, Jianjun, Alberto, Avijit, Shanmukh and Gaurav for making the office an enjoyable place to work. Special thank goes to Nima and Avijit for giving feedback for this thesis and to Mariona for helping me with the *Resumen*.

I am grateful to all ICFOnians making ICFO an insiping and enjoyable place. The thesis would be much more difficult without the help of NFL people, the electronic and mechanical workshops. I am also thankful to HR, KTT, frontdesk and purchasing departments.

Ve evreni eğlenceli bir karnaval alanina dönüştüren Uçan Spagetti Canavarina.

Sayin Barselona tayfasi, sizi unutmadim! Şimdiye kadar beraber geçirdiğimiz geleneksel cumartesi akşamlari için çok teşekkür ediyorum. Barselona bir başka güzel hale geldi o akşamlar sayesinde. Beraber geçirdiğimiz zamanlar özlenmeye değer olacak daima. Ve beraber gerçekleştirdiğimiz daha nice aktiviteler için tekrardan teşekkür ederim.

Ayrica, bu tezin tamamlanmasindaki büyük moral desteklerinden ötürü aileme ve yakin arkadaşlarima içten teşekkürlerimi sunarim. Sizin manevi desteğiniz olmadan bu işin tamalanmasi mümkün olmazdi.

Başka bir projede daha görüşmek dileyiğle efendim,

M. Zafer Akgül, September 2020, Barcelona

Contents

List of Figures

List of Tables

Acronyms and Symbols

FF Fill-factor

V$_{OC}$ Open-circuit voltage

V$_{MPP}$ Voltage at the maximum power point

J$_{SC}$ Short-circuit current density

J$_{MPP}$ Current density at the maximum power point

PCE Power Conversion Efficiency

IQE Internal Quantum Efficiency

EQE External Quantum Efficiency

NIR Near-Infrared region of the spectrum (750-1400 nm)

VIS Visible region of the spectrum (380-750 nm)

UV Ultraviolet region of the spectrum ($<$ 380 nm)

SEM Scanning Electron Microscopy

TEM Transmission Electron Microscopy

STEM Scanning Transmission Electron Microscopy

XRD X-Ray Diffractometry

XPS X-Ray Photoelectron Spectroscopy

UPS UV Photoelectron Spectroscopy

RoHS Restriction of Hazardous Substances

1

Introduction

Behind any advanced civilization lies the machinery of energy production to support the ever-growing needs of the population to prosper.

1.1 Motivation

In this modern era, the use of optoelectronic devices is gaining speed thanks to the value which they provide both daily life and scientific advancement. The applications of optoelectronics are diverse and span a range starting from the generation, detection and manipulation of light - as in lighting, digital cameras and fiber optics communication equipment - to energy production - as in electricity production using photovoltaics. A field that has such an enormous application zone has its own restrictions due to the strict requirements that need to be addressed. For photovoltaics industry, the toxicity, efficiency, abundance and unit cost are major factors contributing to the success of the respective technology (Figure 1.1). However, the production cost plays a profound role in the success of the respective photovoltaics technology. This results from the very competitive price per kilowatt-hour of electricity that is offered by the already existing alternatives in use, such as thermal power plants.

The current fossil fuel-based power plants can supply plentiful cheap electricity; however, the heavy usage of these power plants brings critical risks for the future of the planet. Recent studies have revealed that the immense utilization of the fossil fuels has already caused a noticeable shift in the thermal balance of the world by introducing greenhouse gases into atmosphere. It has been observed that fossil fuel-related CO_2 emission has reached a share of 86 % in global CO_2 emission in the last decade because of the increased industrial activities. [1] As a result, global warming already passed the stage of being a mere prediction and has become a daily observation due to the extra heat captured by greenhouse gasses. [2, 3] Further predictions about the future effects of fossil fuel-based energy production to the environment push governments towards more environmentally friendly methods of energy production as the total energy demand increases steadily since the industrial revolution and it is expected to reach 50 Gtoe/year in 2050. [4]

Renewable energy resources can offer a viable solution to the energy demand of the world. Yet, the price tag on the renewable energy presents a noteworthy challenge for this transition. Although photovoltaics-based renewable energy resources have an immense potential owing to abundant sun light reaching the surface of the earth, [5] the use of this unlimited energy resource is hindered by the cost of solar cell manufacturing. Particularly, single-junction GaAs solar cells can achieve efficiency over 27 % as of now. [6] Considering that the theoretical efficiency of an ideal single-junction solar cell is limited to 34 %, the performance of GaAs photovoltaics is impressive. [7] Furthermore, the efficiency of GaAs modules can be boosted up to 47.1 % with the use of advanced structures, as in the case of multi-junction solar cells with concentrators. [8] Yet, GaAs solar cells have not been able to find widespread use in solar power plants. The utilization of this type of solar cell has been restricted to the applications where the space and weight are considered the major limiting factors - such as in space applications - rather than the cost. Due to the considerable cost associated with this technology, it is not expected to have large-scale GaAs solar power plants to be installed in near future. On the other hand, Si solar cells - being the most commercially available photovoltaics technology today - offer modest efficiency for much lower price thanks to comparatively lower material and processing related cost. Albeit the manufacturing cost is lower than alternatives, the overall module cost of Si photovoltaics still makes competing with thermal power plants a significant challenge due to low prices offered by the mature thermal power plant technology ($< \$0.05$ / kWh). [9] Despite an active research is ongoing on Si photovoltaics technology, the purification of silicon from sand, wafer production and solar cell fabrication processes require a significant amount of energy. Therefore, the potential cost reduction through

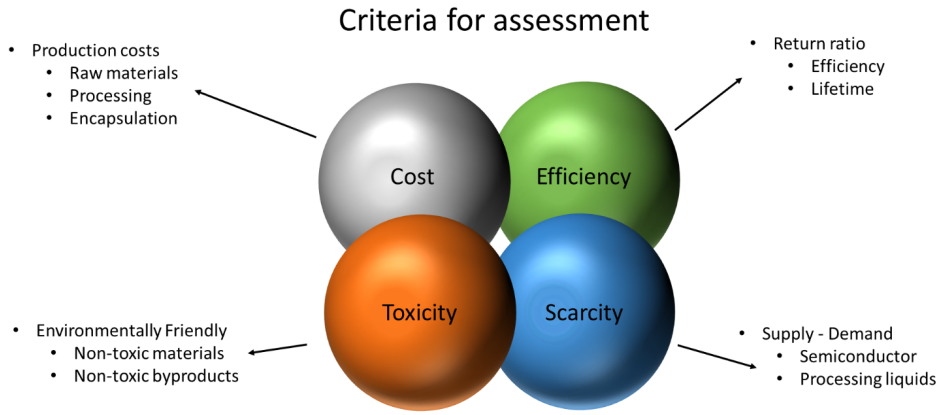

Figure 1.1: Criteria for the assessment of a photovoltaics technology

optimization of the processing conditions is limited by the current production methods utilized in Si photovoltaics. [10] Also, the installation capacity of current Si solar panels is limited ubiquitously due to their rigid and heavy form factor. This reduces their application to areas where a strong weight support can be provided, such as solar farms and rigid rooftops. Nevertheless, the demand for flexible and wearable photovoltaics is increasing and alternative photovoltaics technologies are sought to meet the ever-expanding utilization span of photovoltaics. At this point, colloidal nanocrystals (CNCs) that can be deposited using mild processing methods with low temperature treatment offer a unique solution as it enables the use of temperature-sensitive and fragile substrates (such as cellulose and PET) [11, 12] that can lead to low-cost flexible devices.

As another restriction, the presence of toxic elements in some photovoltaics technologies, such as arsenic in GaAs and cadmium in CdTe solar cells, raises some concerns about the safety of these technologies for large area deployment. The presence of RoHS (Restriction of Hazardous Substances)-incompliant [13] compounds in photovoltaics brings two main issues. First, the production of these solar cells has to be strictly controlled due to the risk of improper disposal of the contaminated waste into the environment. Second, it also makes the recycling of the modules that reach the end of their lifetime more costly and attention requiring as any spillage from an unattended damaged module into the environment can pose a serious health risk to the population. [14,15] Thus, the proper choice of the materials to be used in solar cells constitutes an important step in the development of a reliable photovoltaics technology.

Apart from cost and toxicity, the constituent elements have to be commercially present in abundance for large-scale production. In spite of their capacity to yield high

power conversion efficiency, the scarcity of the constituent elements in some compounds renders their use in photovoltaics inaccessible for large-scale energy production. One of these compounds is copper indium gallium selenide (CIGS). Despite this material can yield a PCE of 23 % and only contains elements with no/low toxicity, the scarcity of indium in the earths crust makes this material not a reliable option for the future of photovoltaics. [16]

Furthermore, solar modules need to provide an acceptable lifespan to guarantee, at least, the return of the capital investment. This means that the efficiency-lifetime product of the solar modules has to be sufficiently large to render the large-scale deployment of the solar modules an economically viable solution. For economical self-sustaining, the photovoltaics technology has to offer attractive profits. In this way, the investors of the private sector can be encouraged to switch from fossil fuel-based power plants to photovoltaics-based power plants.

For the aforementioned reasons, it has utmost importance to design and develop novel ways for the large-scale production of low-cost, non-hazardous materials using abundant elements to limit the negative impact of energy production for the true realization of the renewable and environmentally friendly energy production using photovoltaics.

1.2 A brief history of photovoltaics

Although sun light has been in use for various purposes since the beginning of the civilization, the idea of direct conversion of light energy into electricity was pioneered by a curious experiment involving an electrochemical cell under light exposure. After this experiment had led to a direct observation of the photovoltaic effect by Becquerel in 1839, the possibility of manipulating the electronic properties of materials with light attracted considerable attention in the scientific community as an interesting phenomenon. Later in 1873, it was shown on a piece of selenium that the conductivity of solids could be manipulated with light exposure in a similar manner. [17] In the following years, an observation of electricity generation in solid selenium-metal junctions was published by Adams and Day, laying the foundations of the field of solid-state photovoltaics. [18] However, the exact working mechanism was not completely understood till the Einsteins famous work on the photovoltaic effect. [19] Following the available experimental observations and Einsteins explanation of the photoelectric effect, the conversion of light energy directly into electricity in a practical way was demonstrated by Bell labs in 1954. [20] Using the relatively mature silicon processing technology of the time, a monocrystalline silicon solar cell with a power conversion efficiency (PCE)

around 6 % was presented to the public for the first time. Thanks to this achievement, photovoltaics has become an important tool today for the utilization of sunlight for energy production.

1.3 Fundamentals of solar cells

Similar to other energy converters, solar cells function by transforming one kind of energy into another. In a simple solar cell, the conversion process begins with the capture of the energy of a photon in a semiconductor to excite an electron from a lower to an upper energy level, leaving behind a "hole", a positively-charged quasiparticle (Figure 1.2a-b). After the generation of electron-hole pair, electron and hole are separated from each other and collected at different electrodes by making use of selective contacts (Figure 1.2d). Then, the potential difference of electrons and holes that are collected at different electrodes can drive an external load to perform a useful task.

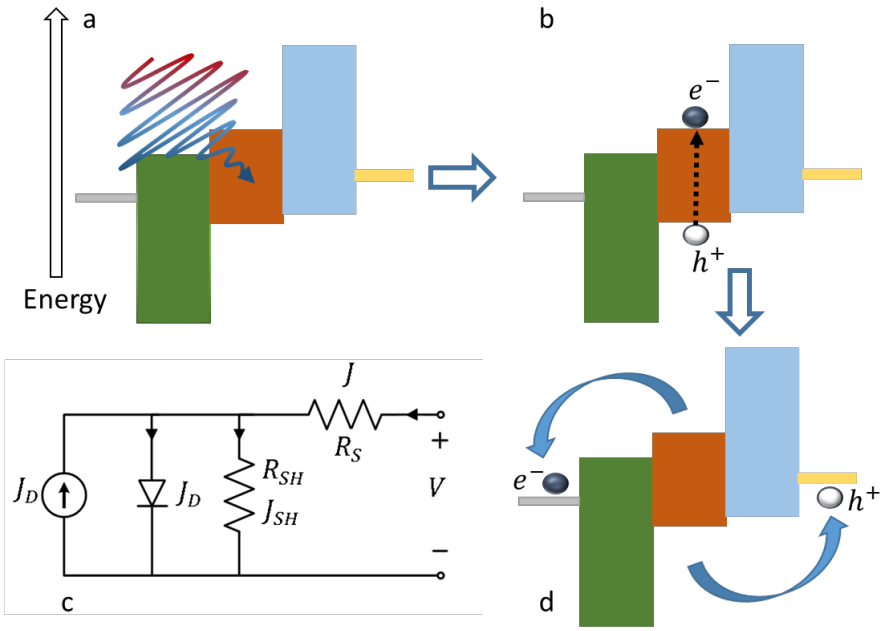

Figure 1.2: Basic operation of a typical solar cell depicting the electron - hole pair generation by photon absorption and carrier collection processes (a, b and d) and a simplified electrically equivalent solar cell circuit (c).

In a simplified solar cell model, the internal current pathways in a solar cell can be modeled as a combination of a series resistance (R_S), a parallel resistance (R_{SH}), an internal diode (J_D) and a current source (J_L) (see Figure 1.2c). Following this

circuit diagram, the equations governing the current paths in the solar cell can be derived as given in Eq. 1.1a-c. Different element in this simplified solar cell model can be attributed to different processes occurring in the solar cell. According to the given set of equations, there are two main paths in which the current generated due to the photon absorption can be lost. The first path is governed by the internal diode that is present in p-n and Schottky junction solar cells. The effect of this diode is such that a high J_0 results typically from high minority carrier density in the quasi-neutral regions of the junction (n_p/p_n denotes the electron/hole density in the p/n-side of the junction. D_n/D_p and L_n/L_p are the diffusivity and diffusion length of electrons/holes. See Section 1.3.2 for further details.). [21] As this diode acts as a current sink in the device, it causes a drop in maximum obtainable voltage and current (V_{OC}, J_{SC}) from the device (Eq. 1.1b).

$$
\begin{aligned}
&(a) \qquad J = J_D + J_{SH} - J_L \\
&(b) \qquad J_D = J_0[e^{\frac{q(V-JR_S)}{nkT}} - 1], \quad J_0 = q[n_p \frac{D_n}{L_n} + p_n \frac{D_p}{L_p}] \\
&(c) \qquad J_{SH} = \frac{V-JR_S}{R_{SH}}
\end{aligned}
\tag{1.1}
$$

The second loss path is related to presence of the parasitic resistors in the solar cell (Eq. 1.1c). The resistors R_{SH} and R_S denote the imperfections in the device and represent the current shorts between the anode and cathode of the solar cell and the hindrance of charge carrier transport between layers in the device, respectively. The main effect of the R_{SH} is observed under open-circuit conditions as finite R_{SH} causes a reduction in V_{OC} ($J = 0$, but $J_{SH} > 0$ thus $J_D < J_L$). R_S, on the other hand, has a pronounced effect on short-circuit current (J_{SC}) as nonzero R_S causes J_L be shared between the internal diode, R_{SH} and R_S due to parallel connection of the internal diode and these two resistors under short-circuit condition. The fill factor of the solar cell, which is explained in Section 1.4.1, is measured to be lower than its ideal value due to the combined effect of these two parasitic resistors within the device. Thus, it is desirable to have a small R_S while keeping R_{SH} as high as possible to obtain the best performance from a given solar cell.

In the design of a photovoltaic cell, there are numerous factors to be considered, starting from the design of the photovoltaic stacks from an optical point of view to the band alignment and surface passivation of the semiconductors used in the solar cell. In the following sections, we will briefly discuss about the important parameters

of the semiconductors acting as the photon absorbers in a solar cell due to their direct impact on the performance of the device. Later, we will provide an informative section about the experimental methods that can be carried out to quantify these parameters to show how they affect the performance of the solar cells.

1.3.1 Optical key properties of semiconductors

Absorption process is highly dependent on the characteristics of the semiconductors, such as the semiconductor´s strength of absorbing photons, which is given in terms of the absorption coefficient of the material. As the effectiveness of absorption is related to material absorption coefficient, it is beneficial to use a semiconductor with high absorption coefficient to absorb as many photons as possible for a certain absorber thickness. From this perspective, it is advantageous to use a direct bandgap semiconductor as the absorber, since direct bandgap semiconductors exhibit higher absorption coefficients compared to the indirect bandgap semiconductors. This results from the misalignment of the conduction and valence band edges in energy - momentum space for indirect bandgap semiconductors. As a result of the misalignment, the momentum of electron requires a change by the involvement of a another species in the absorption process to enable the indirect transition. This change in momentum is typically provided by the lattice vibrations, the so-called "phonons", in crystalline semiconductors. Because of the involvement of phonons in the absorption process, the probability of indirect transitions is low, leading to lower absorption coefficient in indirect bandgap semiconductors with respect to their direct bandgap counterparts. Thus, due to lower absorption coefficient, solar cells that are made of indirect bandgap semiconductors, such as crystalline Si, have typically hundreds of microns thick absorber layer. This is a direct result of fact that thin layers of indirect bandgap absorber would allow a considerable amount of photons to pass through, particularly in the long wavelength regime (e.g., near infrared) where the absorption coefficient diminishes significantly. [22, 23] On the other hand, solar cells made of direct bandgap semiconductors can yield high efficiency with very thin absorber layer. This has multiple benefits in terms of device manufacturing. First, the effective distance that must be traveled by the charge carriers is reduced due to reduced absorber thickness. This permits the use of relatively cheaper semiconductors with low lifetime-mobility product (See Section 1.3.2). Second, it enables efficient use of expensive absorber material as well as the production of thin, flexible and lightweight photovoltaics. [24–26]

1.3.2 Electronic key properties of semiconductors

After the formation by the absorption of photons, the electron-hole pairs need to be dissociated for collection of electrons and holes at the opposite sides of the junction.

The collection process is achieved by two major forces. The built-in electric field exerted on the charge carriers in the space-charge region (established by the inherently present Schottky or p-n junction in a typical solar cell) causes a drift current to form. The force acting upon the charge carriers during this transport can be expressed as given in Eq. 1.2a.

$$\begin{aligned} &(a) \qquad \nu = \mu\varepsilon \\ &(b) \qquad L_{Drift} \cong \tau_C \nu = (\tau_C \mu)\varepsilon \end{aligned} \tag{1.2}$$

In Eq. 1.2b, ν, μ, τ_C and ε denote the velocity, mobility and effective lifetime of the charge carrier and the electric field at the location of the charge carrier, respectively. If we assume that the electric field and mobility are constant in the region of interest, then it can be deduced that charge carriers can drift, as a first-order approximation, by a length that is determined by the lifetime and mobility of the charge carrier and the strength of the electric field before the charge carriers are lost due to recombination.

$$L_{Diff} = \sqrt{\frac{kT}{q}\mu\tau_C} \tag{1.3}$$

However, the internal electric field diminishes in regions sufficiently far away from the p-n junction of the solar cell (quasi-neutral region), giving rise to negligible drift current. At this operation zone, another mechanism becomes the dominant driving force in carrier transport within the device. The formation of electron - hole pairs by the absorption of the incoming photons creates a non-zero carrier density gradient in the solar cell. As a result of the non-zero carrier density gradient, electrons and holes can move from high density to low density zones to establish a uniform carrier density within the device and a diffusion current is created. Owing to the nature of the diffusion mechanism, the diffusion length of the charge carriers (L_{Diff}) in a photovoltaic device, hence the device photocurrent that is a function of the diffusion length, is highly dependent on the electronic properties of the absorber layer such as the lifetime and mobility of the carrier as well as the temperature of the absorber (Eq. 1.3; q and T denote the electronic charge and absolute temperature, respectively). [27] As seen in Eq. 1.2 and Eq. 1.3, low mobility-lifetime product of the absorber can act as a bottleneck in achieving high efficiency photovoltaics by limiting both

L_{Drift} and L_{Diff}. In the following discussion, we are going to keep the focus of the section on the recombination mechanisms that lower lifetime-mobility product of carriers in semiconductors to provide the readers with the required background for the subsequent chapters. A more detailed discussion about the charge carrier dynamics in semiconductors can be found elsewhere. [21]

The mobility-lifetime product of charge carriers in a semiconductor can be diminished by different types of recombination processes. Three major recombination processes in semiconductors can be listed as the radiative (band to band) recombination, Auger recombination and Shockley-Read-Hall (SRH) recombination. [28] In the radiative recombination, an electron in the conduction band and a hole in the valence band of a semiconductor recombine and the resulting energy is released in the form of a photon. While this process is the main mechanism that the operation of LEDs and lasers relies on, the radiative recombination diminishes the performance of solar cells, since it may decrease the number of electrons and holes that can be harvested by the electrodes. [29] Apart from the radiative recombination, Auger recombination results from the presence of excess charge carriers in the conduction and valence bands of the semiconductor. In Auger recombination mechanism, an electron-hole pair recombines and its energy is given to a third charge carrier, instead of being emitted as a photon. As the energy of the free charge carriers is typically lost through fast thermalization, [30,31] this process also causes a reduction in the solar cell performance. [32] In the SRH recombination, unlike radiative and Auger recombination, the charge carrier loss occurs via recombination centers (or trap states) that are present in the bulk or on the surface of the semiconductor. [33]

The presence of the recombination centers in a semiconductor has two main effects on the performance of the solar cell. As the primary effect, the recombination centers decrease the lifetime of the charge carriers within the semiconductor by increasing the non-radiative recombination rate. The effective carrier lifetime in a semiconductor can be expressed as in Eq. 1.4.

$$
\begin{aligned}
&(a) \quad \frac{1}{\tau_C} = \frac{1}{\tau_R} + \frac{1}{\tau_{SRH}} + \frac{1}{\tau_{Auger}} \\
&(b) \quad \frac{1}{\tau_R} = R_{Radiative} = \beta(np - n_i^2) \\
&(c) \quad \frac{1}{\tau_{SRH}} = R_{SRH} = \frac{(np - n_i^2)}{\tau_p(n + n_i e^{\frac{E_T - E}{kT}}) + \tau_n(p + n_i e^{\frac{E - E_T}{kT}})} \\
&(d) \quad \frac{1}{\tau_{Auger}} = R_{Auger} = (C_{ehh}n + C_{eeh}p)(np - n_i^2)
\end{aligned}
\tag{1.4}
$$

Here τ_R, τ_{SRH} and τ_{Auger} denote the radiative, SRH and Auger lifetime of a charge carrier. The parameters $R_{Radiative}$, R_{SRH}, R_{Auger}, n, p, n_i, β, τ_n, τ_p, E_T, C_{eeh} and C_{ehh} stand for the radiative, SRH and Auger recombination rate, the electron, hole and intrinsic carrier density, the radiative recombination rate constant, electron lifetime, hole lifetime, energy of the trap state, Auger constant for 2 electron-1 hole recombination and Auger constant for 1 electron-2 holes recombination, correspondingly. [34] If the charge harvesting cannot be carried out fast enough compared to the effective carrier lifetime in a given semiconductor, a significant portion of the charge carriers can be lost due to recombination. As the secondary effect, the presence of the recombination centers, which can also be introduced by ionized impurities, generally accompanied by the electric field non-uniformity in semiconductors. Due to these deviations in the electric field, the movement of the charge carriers are hindered by scattering, which reduces the charge carrier mobility in the layer. [35–37] As both the diffusion and drifts currents have strong dependence on mobility of the charge carriers, the device performance degrades with the use of a defective semiconductor. Thus, selection of a semiconductor that can support long carrier lifetime and high carrier mobility simultaneously is advantageous in the design of a high performance solar cell.

1.4 Characterization methods for solar cells

Although there are vast number of characterization methods that focus on different parameters of the solar cells, we will cover only the most important ones in this Chapter, including power conversion efficiency, external quantum efficiency, light intensity- and time-dependent current-voltage scanning and capacitance-voltage scanning, to provide the reader with sufficient background for subsequent chapters.

1.4.1 Power conversion efficiency (PCE)

The first and the most basic method to measure the power conversion efficiency of the solar cells makes use of a light simulator that can mimic the spectral density of sunlight in a lab environment. In this setup, the current density-voltage (J-V) curves of a solar cell are measured under light bias (Figure 1.3a). Then, the power conversion efficiency (PCE) of the device is calculated as the ratio of electrical power given by the device to the optical power impinging on the device. The maximum power output from a solar cell is obtained at a specific point, which is properly called maximum power point, (J_{MPP}, V_{MPP}) that lies between the short-circuit current density (J_{SC}, 0) and

open-circuit voltage (0, V_{OC}) points on the J-V curve of the device under light.

$$PCE = \frac{V_{MPP}J_{MPP}}{P_{Optical}} = FF\frac{V_{OC}J_{SC}}{P_{Optical}} \tag{1.5}$$

As seen in Eq. 1.5, a parameter, the so-called fill factor (FF), takes part in the efficiency equation. For an ideal photovoltaic cell, FF takes the value of unity, signifying that the product of J_{SC} and V_{OC} determines the efficiency instead of the product of J_{MPP} and V_{MPP} (the area of the dash-dotted square versus of the dashed square in Figure 1.3a). This constant determines how closely the device under test resembles to an ideal photovoltaic cell. Due to the non-idealities present in real photovoltaic devices (as few of them is explained in Section 1.3.2); however, FF is always found to be smaller than unity.

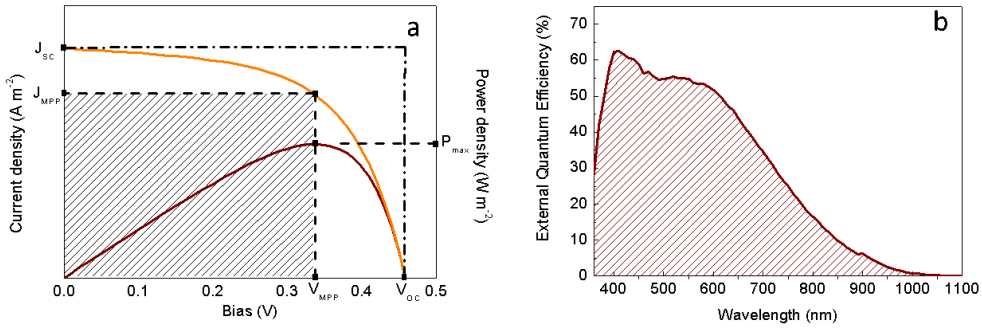

Figure 1.3: Typical solar cell characterization methods. (a) Current density-voltage (J-V) and power density-voltage curves, (b) External quantum efficiency (EQE) - wavelength curve.

1.4.2 External quantum efficiency (EQE)

The second most commonly employed method uses a relatively weak monochromatic light to probe the spectral response of the device under test within the spectrum of interest (Figure 1.3b). For this measurement, generally short-circuit current of the device is recorded with respect to the wavelength of the light impinging on the device. The resulting curve demonstrates the effectiveness of the device in utilization of the solar irradiance spectrum for carrier generation and collection. In mathematical terms, this measurement can be expressed as given in Eq. 1.6, where h, c, q, ϕ_{photon} and λ denote Planks constant, the speed of light, elementary charge, photon flux on the

device and the wavelength of the excitation source.

$$EQE(\lambda) = \frac{hc}{q\lambda} = \frac{J_{ph}}{\phi_{photon}(\lambda)} \tag{1.6}$$

In addition, as J_{SC} is the maximum current density a solar cell can provide under 1 Sun light bias, EQE and J_{SC} are interrelated and this relation can be expressed for a photovoltaic cell, under the assumption that the device does not posses significant light intensity-dependent performance characteristics, as Eq. 1.7.

$$J_{SC} \cong J_{EQE} = \int q\phi_{photon}(\lambda)EQE(\lambda)d\lambda \tag{1.7}$$

Thus, the integral of the external quantum efficiency of a solar cell over the solar irradiance spectrum gives information about the maximum obtainable J_{SC} for a given device. Thanks to this link between two measurement methods, EQE spectrum can provide additional information about the presence of light intensity-dependent processes as an increase in charge carrier recombination will result in a J_{SC} lower than J_{EQE} due to higher intensity of the light source, thus higher carrier density within the device. [38]

Light intensity-dependent voltage - current scan

Although J-V scan under standard operating conditions can yield device performance, it cannot provide information about the charge carrier density-dependent characteristics of the solar cell. In light intensity-dependent J-V scan, the voltage and current density of a photovoltaic cell are measured with respect to the intensity of the light impinging on the device. As the carrier lifetime depends on the density of the carriers in the device, the light bias-dependent J-V measurements can pin down the recombination mechanism that is dominant in the solar cell.

$$J = J_0[e^{\frac{qV}{nkT}} - 1] - J_L, J_L = \alpha\phi^m \tag{1.8}$$

The current density of an ideal p-n junction photovoltaic cell under light can be expressed as in Eq. 1.8. Here, J, J_L, q, n, k, T, α, ϕ and m denote the external current density measured by an I-V profiler, photocurrent density induced by the

light bias, elementary charge, ideality factor, Boltzman constant, absolute temperature, proportionality constant, light intensity and power factor, respectively. If the device is measured under short-circuit conditions (V = 0V), then the above equation simplifies to Eq. 1.9.

$$J_{SC} = -\alpha\phi^{m} \longrightarrow ln(J_{SC}) = mln(\phi) + constant \tag{1.9}$$

A log - log plot of J_{SC} versus light intensity can give information about the presence of different recombination pathways that are dependent on the light intensity impinging on the device. For an ideal solar cell, the parameter m is expected to be unity. However, in the presence of light intensity-dependent recombination processes the value of m will deviate from unity and the amount of deviation reflects a quantitative analysis of the performance of the solar cell.

$$V_{OC} = \frac{n_{ID}kT}{q} ln(\phi) + constant \tag{1.10}$$

The expression for the light intensity-dependent open-circuit voltage can be written in a similar way. In Eq. 1.10, the parameter n_{ID} denotes the diode ideality factor that is a function of the charge carrier recombination pathways present in the device. The diode ideality factor assumes distinct values depending on the contribution of different recombination processes to the carrier loss in the device. The link between the diode ideality factor and the recombination processes can be expressed as given in Eq. 1.11.

$$n_{ID} = \frac{2}{\gamma} \tag{1.11}$$

In Eq. 1.11, γ represents the reaction order of the recombination rate. Hence, a diode ideality factor that is close to unity suggests that the recombination rate has a second order characteristics, which is the case for radiative (band to band) recombination under high injection ($p \cong n >> n_i$). On the other hand, a diode ideality factor that is close to 2 hints about the control of the recombination rate by the density of the minority carrier, which can be related to SRH recombination and radiative recombination under low injection conditions in doped semiconductors for which only the density of

the minority carrier can limit the recombination rate. If Auger recombination becomes the dominant process in the charge carrier loss path, diode ideality factor approaches to 2/3 due to the involvement of three carriers in this recombination mechanism. [29, 39] Thus, light intensity-dependent V_{OC} and J_{SC} measurements can be used to obtain useful insights about the recombination processes occurring in the solar cell.

Capacitance - voltage scan

Another useful method for the characterization of the photovoltaic devices uses the change in the depletion width of a junction with respect to the applied voltage bias to measure the carrier density and built-in voltage of the junction. [40–42] As a conventional solar cell has either a p-n junction or a Schottky junction within the device structure, the effective charge carrier densities in the photovoltaic stack can be determined via voltage-dependent capacitance measurement. In this section, we present an analysis method for a conventional p-n junction solar cell for all the results that are presented in this thesis have been obtained from p-n junction solar cells. Yet, the same equations can be used to analyze a Schottky junction solar cell if modified using the knowledge that the charge carrier density in one side of the junction is typically much higher than that of the other side ($N_n >> P_p$ or $N_n << P_p$). The relation of capacitance of a p-n heterojunction to the applied voltage can be describes as given in Eq. 1.12.

$$\frac{A^2}{C^2} = \frac{2(\epsilon_n N_n + \epsilon_p N_p)}{q\epsilon_0 \epsilon_n \epsilon_p N_n N_p}(V_{bi} - V - \frac{2kT}{q}) \tag{1.12}$$

In the above equation, (ϵ_n and N_n) and (ϵ_p and N_p) are material specific parameters and they denote the dielectric constant and carrier density of the n- and p-type parts of the heterojunction, respectively. If these values are known for one side of the junction, the values of the other side of the junction can be easily obtained by employing the following equation that is obtained by differentiating Eq. 1.12 with respect to V.

$$N_n = \frac{-2\epsilon_p N_p}{q\epsilon_0 \epsilon_n \epsilon_p N_p \frac{\partial}{\partial V}(\frac{A^2}{C^2}) + 2\epsilon_n} \tag{1.13}$$

Also, inherently having a junction, solar cells have built-in potentials that is expressed by the parameter V_{bi} in Eq. 1.14 (V_{cross} represents the intersection point of

the tangent line of $\frac{A^2}{C^2}$-V with the voltage axis.).

$$V_{bi} = V_{cross} + \frac{2kT}{q} \tag{1.14}$$

As the maximum voltage that can be obtained is limited by the built-in voltage of a p-n junction solar cell, C-V scans can give useful information about the performance-limiting factors in the device, such as band level misalignments and high carrier density in the absorber layer.

Time-dependent $\mathbf{V}_{OC}/\mathbf{J}_{SC}$

In this thesis, we follow a method published in the literature to measure the density of trap states in the absorber layer. [43] The measurement of the density of trap states (DOTS) within the bandgap of an absorber can be carried out with the use of time-dependent measurement techniques, such as transient photovoltage (TPV) and transient photocurrent (TPC). TPV and TPC are useful methods as they can be employed to probe the trapping/detrapping of the charger carriers within the bandgap. Basically, TPV and TPC curves are recorded under different light bias. The intensity of the bias light is changed to adjust the electron and hole Fermi levels in the device as the positions of the Fermi levels depend on the concentration of the carriers, [21] hence on the intensity of the applied light bias. TPV and TPC techniques typically employ a short laser pulse to induce a temporary increase in the electron and hole densities in the device. Then, the recombination of the excess carriers is recorded with respect to time, which can be carried out through oscilloscope measurement.

For TPV measurement, the device is connected to a high impedance input of an oscilloscope to record the V_{OC} of the device with respect to applied light bias.

$$V(t) = A_{OC} exp(\frac{-t}{\tau_{OC}}) + V_{OC} \tag{1.15}$$

The obtained voltage trace is fitted against Eq. 1.15 to extract the amplitude of differential voltage, which gives information about the Fermi level splitting in the device.

For TPC measurement, the device is connected to a low impedance input of an

oscilloscope to record the J_{SC} of the device with respect to applied light bias.

$$I(t) = A_{SC} exp(\frac{-t}{\tau_{SC}}) + I_{SC} \tag{1.16}$$

The obtained voltage trace is fitted against Eq. 1.16 to extract the values of A_{SC} and carrier lifetime. The above procedure given for TPV and TPC measurements is repeated for different values of the applied light bias to scan the density of trap states within the bandgap. After extraction of A_{SC}, and A_{OC} the differential capacitance (C_D) resulting from the trapping/detrapping of the charge carriers in the bandgap is calculated using Eq. 1.17. Here, it is worth to mention that C_D is not the static capacitance originating from the physical structure of the device; it is rather a dynamic value with its origin in the trapping/detrapping of the charge carriers within the semiconductor.

$$C_D(V_{OC}) = \frac{Q_D(V_{OC})}{V_D(V_{OC})} = \frac{A_{SC}(V_{OC})\tau_{SC}(V_{OC})}{A_{OC}(V_{OC})} \tag{1.17}$$

As the last step in this calculation, the differential capacitance resulting from Eq. 1.17 is divided by the volume of the absorber (A and d are the area and the thickness of the semiconductor, respectively.) to obtain the density of trap states in the bandgap of the semiconductor with respect to V_{OC} as provided in Eq. 1.18.

$$DOTS(V_{OC}) = \frac{C_D(V_{OC})}{qAd} = \frac{A_{SC}(V_{OC})\tau_{SC}(V_{OC})}{qAdA_{OC}(V_{OC})} \tag{1.18}$$

DOTS - V_{OC} method is quiet useful as it gives both the energetic position and the density of the charge traps in the bandgap, thus enabling the use of a passivation scheme targeting a specific trap type.

1.5 Current solar cell technologies

The solar cells can be divided into two main categories depending on their approach towards the fabrication process, namely bulk and thin-film solar cells. In this part, we will provide a brief discussion of each type to emphasize the pros and cons of the respective approaches.

1.5.1 Bulk Solar Cells

Bulk solar cells are the first successful type of solar cells. A definitive feature of this group is the use of the semiconductor both as an absorber layer and as a mechanical support for the whole device, similar to the typical Si-based chips. This is enabled by the high mobility (10^2 - 10^3 cm^2 V^{-1} s^{-1}) and large range of both n-type and p-type doping for Si as these properties make possible to form all-Si p-n homojunctions. [44] Currently there are two main routes followed in Si-based photovoltaics of this type. For monocrystalline Si solar cells, a single crystal Si wafer is used as a substrate to produce the solar cell. In this process, either a p-type or n-type Si wafer is doped with suitable ions to form a p-n homojunction. The efficiency of the current monocrystalline Si cells can be as high as 26 % with the utilization of proper passivation methods. [23] The polycrystalline Si solar cells exploit a similar process flow, but a polycrystalline Si wafer is used instead of a monocrystalline one in the fabrication and the efficiency of a polycrystalline Si solar cell can reach 21.9 % with the use of proper passivation schemes. [45]

Excessive use of the absorber (Si in this case) is one of the main issues related to this type of solar cells for the material that acts as a mechanical support for the device does not contribute to the photovoltaic performance of the device. To reduce the amount of absorber, a less expensive substrate can be utilized instead of photovoltaics-grade Si. In the next part, this approach will be discussed with examples to show the possible routes that are employed in the field to reduce the cost.

1.5.2 Thin-film solar cells

Although the production of bulk solar cells is straightforward and well established, the limited material availability for bulk solar cell production and the cost involved in the process shed doubts about their widespread usage. In addition, it is known to be a difficult process to produce single crystal wafers of all materials with low defect density due to their complicated and less understood crystal nucleation and growth mechanisms. Thin-film solar cells are proposed to overcome these issues. In this type of solar cell, the active layers are grown onto a mechanically supporting substrate to form the photovoltaic cell, typically a glass substrate. As the mechanical integrity of the device is provided by a relatively cheap substrate instead of the semiconductor itself, the thickness of the active layers can be reduced significantly, giving an opportunity for better utilization of the costly active materials.

There are currently two routes that are in use for the production of thin-film solar cells. In the first route, the layers in the solar cell structure are deposited sequentially onto a substrate via vacuum-based deposition methods. [46, 47] In the latter, the

active layers are formed via solution processing method, such as spin coating and dip coating. [48, 49] Although the first route yields better results as of now, a significant research effort has been dedicated to the latter to improve the performance of solution-processed solar cells in order to alleviate the cost and scalability problems resulting from the use of vacuum deposition methods.

Vacuum-deposited thin-film solar cells

As of now, various types of thin-film solar cells have already been introduced into the literature. For example, thin-film Si solar cells, which are built on a glass substrate, can yield over 10 % efficiency. [50] As another example, thin-film copper indium gallium sulfide selenide (CIGS) solar cells can reach a PCE of 23 % thanks to its suitable bandgap and electronic characteristics for photovoltaics. [51] Besides, copper zinc tin sulfide (CZTS) has raised curiosity among researchers thanks to its structural similarity to CIGS and zinc being present in larger quantities than indium in the earth crust. [16] Thanks to the deep understanding of defect passivation in this material, a study on a CZTS solar cell with a PCE of 10 % has already been reported. [52] In addition, another chalcogenide family semiconductor, cadmium telluride (CdTe), has been shown to be a mature thin-film solar cell technology with a PCE of 22 % with commercial success. [53]

Solution-processed thin-film solar cells

Due to the high cost associated with vacuum deposition methods, the heavy use of vacuum deposition methods in photovoltaics production puts a hard-lower limit to the overall cost of the modules. To address the cost problem, solution-processing methods have been proposed as alternatives to the vacuum deposition methods. Even though promising, there exist some challenges to be addressed for successful utilization of these methods in photovoltaics production. For example, any solid material has to be converted into liquid phase for these methods to function properly. While this is not easily achievable for all types of materials, successful demonstrations of this methodology have already been reported in the literature. [54,55] As one of the solution-processable semiconductors, organic semiconducting polymers have been put into use in solar cells to overcome the problem with both abundance, processing difficulty and toxicity. Thanks to the advances in polymer science, it has been shown that it is possible to engineer the bandgap, electronic properties and solubility of polymers through proper design of the carbon backbone and side groups. Recent advances in this field have resulted in a polymer solar cell with a PCE of more than 17 %. [56] However, organics being inherently more vulnerable to environmental factors and offering inferior electronic properties compared to inorganic counterparts ($\mu \leq 10^2$ cm^2 V^{-1} s^{-1} for

the best performing organic semiconductors to date [57] versus $\mu \geq 10^4$ cm^2 V^{-1} s^{-1} for GaAs, a typical inorganic semiconductor used for high-efficiency photovoltaics [58]) still postpones the use of this technology for commercial energy production. As another advancement in the field, a semi-solid structure has been utilized in solar cell design, so called dye-sensitized solar cell (DSSC), to lower the module cost by making better use of the absorber material and enabling the use of lower quality absorbers by facilitating the charge carrier collection via an electrolyte. The current world record for this type of solar cell has reached 13 %. [59]

As another example, inorganic and hybrid solution-processed perovskite solar cells hold great promise towards high-performance and low-cost photovoltaics thanks to the use of much simpler and cheaper solution-prosessing methods. Recent advances in understanding the crystal formation and defect passivation mechanisms in Pb-perovskites have led to development of all solution-processed photovoltaics and has already boosted the attainable PCE to more than 20 %, [60–62] demonstrating the high-capability of solution-processed materials for photovoltaics. However, the stability and the presence of significant amount of Pb in these solar cells shed doubt about their widespread deployment in energy production and push researches towards more environmentally-friendly alternatives.

1.6 Colloidal nanocrystal photovoltaics

Nanocrystals are very small-sized crystallites, generally with a diameter of less than 100 nm. Vacuum-deposited nanocrystals are in use in the photovoltaics field for the last few decades thanks to their distinctive features, such as bandgap tunability and the formation of intermediate-level energy bands. [63,64] However, they have not been able to find a widespread use because of the cost associated with the utilization of high-cost deposition methods. Due to this reason, alternative deposition methods have been investigated to lower the overall cost of the emerging photovoltaics technologies. Colloidal nanocrystals (CNCs) synthesized via wet chemistry methods are expected to have a special role in low-cost photovoltaics industry as they offer an elegant solution to the expensive film deposition process by eliminating high energy consumption and high vacuum conditions typically demanded by complex deposition systems. This is enabled by providing alternative means with softer processing conditions, consequently minimizing the processing requirements and cost.

In addition to lower cost, CNCs can exhibit interesting optical and electronic properties thanks their small size. [65] Especially, the quantum confinement effect, which originates from a crystallite radius comparable to exciton Bohr radius (Eq. 1.19),

opens new ways to alter the optoelectronic properties of the nanocrystals without changing their chemical structure. In Eq. 1.19, r_B, ϵ_r, m, μ and α_B denote the exciton Bohr radius, the dielectric constant of the material, the mass, the reduced mass and the hydrogen Bohr radius ($\sim$ 0.053 nm), respectively. Quantum confinement effect has already been utilized to tune the absorption and emission characteristics of the colloidal nanocrystals for various types of devices, including photodetectors, LEDs, [66, 67] lasers, [68–70] and solar cells. [71]

$$r_B = \epsilon_r \frac{m}{\mu} \alpha_B \tag{1.19}$$

1.6.1 Current trends and prospects on colloidal nanocrystal photovoltaics

With reports from lead sulfide (PbS) and Pb-perovskite solar cells already exceeding 10 % and 15 % PCE, respectively, colloidal nanocrystal solar cells have already proved to be promising alternatives to vacuum-deposited solar cells. [72, 73] Nonetheless, the presence of significant amount of Pb in these compounds raises concerns about Pb spillage into the environment. [74] These concerns, in return, push researchers to look for alternatives as it is well known that Pb^{2+} salts are generally water soluble and can easily mix into underground water supplies in case of an uncontrolled leakage. [75] Due to this problem, the research efforts in this field has been directed toward other solution-processable inorganic materials that contain more environmentally-friendly elements. Among them, tin sulfides [76] and tin perovskites [77–81] have had success in showing PCE approaching 10 %. In addition, ternary I-III-VI_3 and quaternary I_2-II-IV-VI_4 metal chalcogenide compounds have drawn attention due to their favorable optical properties comparable to Pb-containing counterparts. Among nanocrystal-based technologies, copper indium disulfide (CIS), copper zinc tin sulfide (CZTS) and derivatives have fueled the solution-processed photovoltaics research and have given a PCE in excess of 10 %, opening an opportunity for exploration of other possible RoHS-compliant alternatives in CNC-based photovoltaics. [82–88]

While the use of non-toxic elements and solution-processing methods in photovoltaics fabrication resulted in significant cost reduction and relieved the environmental concerns originating from the presence of toxic elements, air-free techniques that are required for the colloidal synthesis of the nanocrystals still remains as a difficult challenge to elucidate. There has been few attempts to eliminate the need for high temperature reaction for the formation of these CNCs; however, no high performance solar cells

based on these CNCs has been shown to the best of our knowledge. [89–91] Furthermore, CIS and CZTS CNCs generally require high temperature annealing under selenium-rich atmosphere after CNC deposition for high efficiency operation. This increases both the complexity and the overall cost of the photovoltaic devices based on these CNCs and severely limits the available options as substrate. [92–95]

In addition to the toxicity of the constituent elements, the scalability of the synthetic methods is an important challenge to be addressed to achieve economically-viable CNC-based photovoltaics. Despite the hot-injection methods are the most widely used ones in lab-scale synthesis of CNCs, the scalability of the hot-injection methods is typically complicated. This stems from the fact that the quality of the nanocrystals synthesized via hot-injection methods depends on the rapid and homogeneous mixing of the precursors at elevated temperatures to control the nanocrystal nucleation. However, the injection becomes slower and less predictable as the batch volume increases, which results in variation of CNC properties as the synthesis volume is increased. To eliminate the need for strict control on the speed of injection and mixing time of the precursors in the reaction mixture, various methods have been proposed. One typical example of these methods is the heat-up method. [96] In the heat-up synthesis of colloidal nanocrystals, all the ingredients, including the precursors and the reaction solvent, are loaded into the reaction flask before putting the whole system under inert atmosphere and heating. The nanocrystal nucleation is initiated by the gradual thermal activation of the precursors instead of rapid introduction of the precursor into a hot reaction mixture. Thanks to the elimination of injection-related variations, high quality nanomaterials on large scales with little or no batch-to-batch variation can be achieved. Another example is liquid-solid-solution (LSS) method. [97] In LLS method the control over nucleation and growth of nanocrystals is achieved through precursor concentration and temperature. Despite both of these methods can yield nanocrystals with narrow size distribution, the requirement of strict control over reaction temperature to obtain high quality nanocrystals should still be addressed for low-cost large-scale deployment of these methods.

To alleviate the condition of strict control over reaction temperature, room-temperature synthesis methods have been put under investigation. Antisolvent co-precipitation strategy in ambient conditions enabled the room-temperature synthesis of lead perovskite CNCs with high photoluminescence quantum yield (PLQY). [98, 99] In addition to lead perovskite CNCs, the synthesis of metal chalcogenides, such as CdSe, PbS, PbSe and HgTe CNCs, has been demonstrated at room temperature in air-free environment. [100–104] Despite the progress in the field, the realization of an efficient and non-toxic all solid-state nanocrystal solar cell which does not require inert fabrication

environment and/or high temperature sintering still stands as a major challenge for the future of the low-cost photovoltaics. [105, 106]

In the next part, we will look into the wet chemistry methods used for colloidal nanocrystal synthesis to give some insight about how it works and how it can be optimized to lower the material cost further.

1.6.2 Synthesis of colloidal nanocrystals

For a typical wet chemistry synthesis of colloidal nanocrystals, three different groups of ingredients are required. The first type of ingredient is called the precursors and these compounds contain the elements required to form the desired compound. As the second group, a suitable solvent is used as the reaction medium in which the nucleation and growth of nanocrystals take place. The last group of ingredient is called the ligands and these are the molecules responsible from the stabilization of colloidal dispersions in a host solvent. The ligand molecules generally have two ends to satisfy their function. One of the ends has a functional group that is capable of attaching onto the surface of the nanocrystals, among which carboxylates and thiolates are the most commonly used ones. The other end of the ligand may or may not have functional groups depending on the nature of the solvent to be used for the preparation of processing liquids. If the reaction medium is a nonpolar solvent, a general approach is to use a long chain hydrophobic hydrocarbon end to stabilize the nanocrystals during growth (e.g., the long hydrocarbon chain of oleic acid). [107] On the other hand, a polar reaction medium requires the use of a polar functional group, such as the carboxylate group of a thioglycolic acid molecule. [108, 109]

A typical Schlenk line that is used for hot-injection synthesis of CNCs is given in Figure 1.4 to illustrate the experimental setup. Schlenk line is a well-known synthesis setup as it offers simultaneous control over both temperature and chemical environment in which the reaction takes place. A heating mantle connected to an electronic controller generally provides the temperature control. The chemical environment within the flask can be manipulated using the valves connected to vacuum and gas lines. In addition, the use of transparent glass makes it possible to observe the reaction by eye, giving the chemists an opportunity to detect any changes in the reaction mixture easily.

In a hot-injection synthesis of CNCs, a solution of either anionic or cationic precursor in a mixture of solvent and ligand is loaded into the reaction flask. After the temperature is raised to the required level, a solution containing the other precursor is injected into the reaction flask to initiate the nanocrystal nucleation. As there are many tunable parameters in this system, such as injection and growth temperatures, precur-

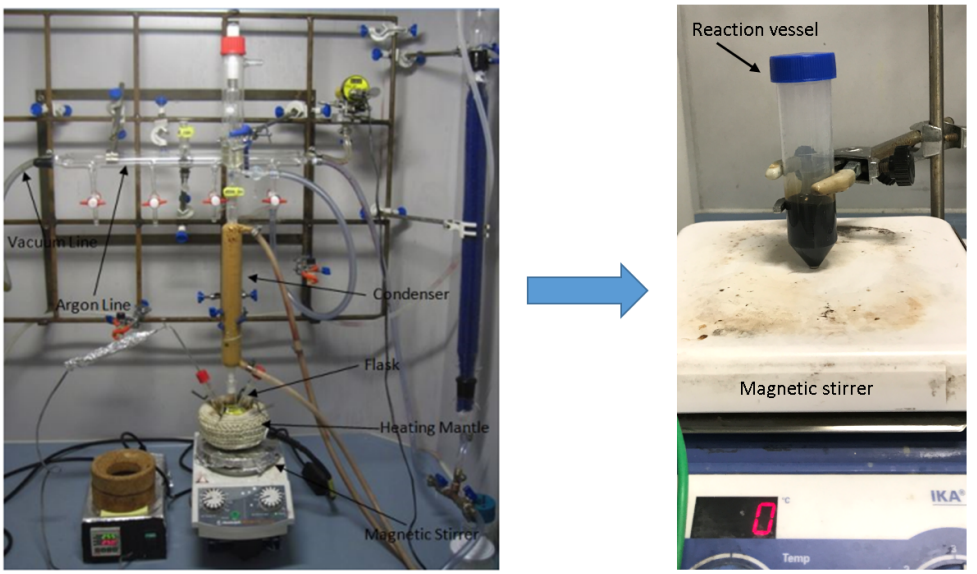

Figure 1.4: Side-by-side comparison of a typical Schlenk-line setup and the proposed ambient condition synthesis setup for the production of colloidal nanocrystals.

sors ratios, precursor concentration and the growth time, this type of synthesis can offer a good degree of control over the nanocrystal properties. However, hot-injection methods can offer limitied capacity in satisfying the requirements of low-cost large-scale photovoltaics. This originates from the high cost due to the labor-intensive synthesis and limited batch size that result from the use of Schlenk line setup.[111]

An ambient condition synthesis scheme can be devised as an alternative to Schlenk line setup. As the synthesis of nanocrystals are carried out at room temperature in the proposed reaction route, the oxidation of the chemicals and nanocrystals can be slowed down sufficiently to eliminate the need for chemically inert reaction environment. With the elimination of high reaction temperature and vacuum/gas lines, the proposed synthesis method requires only a reaction container and a means of stirring the solution to enable the homogeneous distribution of the reactants. Such a simple reaction setup can be seen in Figure 1.4. In addition to the simplicity brought by this route, the reaction at room temperature makes it possible to use inexpensive containers as reaction vessels. In our experiments, we make use of a plastic centrifuge tube as the reaction vessel as can be seen in Figure 1.4.

1.7 Thesis objectives

The objectives of this thesis is to devise and optimize a synthetic method for the production of silver bismuth chalcogenides for use in photovoltaics applications. To achieve this goal, the devised synthetic method has to possess the following properties:

Simple and fast: As any photovoltaics technology is expected to be capable of providing abundant photovoltaic units to the market, the simplicity and speed of CNC synthesis play an important role. This stems from the increased cost that results from the usage of slow and complex, thus labor-intensive, synthetic methods. In this work, we provide a synthetic method that can be carried out within minutes using a very minimalistic synthesis setup.

Scalable: Due to the high material demand of photovoltaics industry, a successful synthetic method needs to provide sufficiently large amounts of CNCs per batch to offer a competitive alternative to the other methods. We show that this condition can be satisfied through elimination of heating and the need for chemically inert reaction atmosphere from the synthesis setup, which is accomplished by the use of chemicals with no/low air-sensitivity compared to widely-used counterparts.

Cost-effective: As the main bottlenecks of photovoltaics industry, unit cost has utmost importance in determining the success of a photovoltaics technology. This thesis presents a method that does not necessitates expensive precursors to function. With low-cost precursors, it is shown that the synthesis-related cost can be reduced significantly.

Environmentally friendly: Toxicity of the elements in a semiconducting compound exhibits another major challenge in photovoltaics industry. This originates from the larger area deployment of photovoltaics modules that is necessary to satisfy the ever-increasing energy demands of the society. Here, we show that it is possible to lower the impact of photovoltaics on the environment by using elements with no/low toxicity in photovoltaics instead of their toxic counterparts, such as cadmium, mercury and lead.

1.8 Thesis outline

In Chapter 2, an ambient condition method for the synthesis of colloidal $AgBiS_2$ CNCs is presented. A study on the reaction time of $AgBiS_2$ CNCs under ambient conditions at room temperature is provided to show the speed and simplicity of the proposed synthesis scheme. A detailed study on the formation dynamics is given to demonstrate that the ternary $AgBiS_2$ is the thermodynamically-favored product of this reaction. The

results of optical spectroscopy and x-ray diffractometry indicated that the product is not contaminated by metallic or binary phases to a detectable limit by these techniques. In the last part of Chapter 2, the effects of the ligands, which are employed during the synthesis, on the properties of the nanocrystals are evaluated and a reaction path is proposed by the examination of the reaction byproducts.

In Chapter 3, we present a detailed ligand exchange study to shed light on the effects of the ligands that are used in the deposition of $AgBiS_2$ CNCs. The results indicate that the photovoltaic performance of $AgBiS_2$ CNC devices can be altered noticeably by the usage of different thiol molecules. It is also demonstrated that the ambient condition synthesis can yield CNCs capable of giving up to 5.5 % efficient solar cells with the use of short chain alkyl thiols.

In Chapter 4, a room-temperature ambient condition synthesis method is given for the synthesis of $AgBiSe_2$ CNCs. $AgBiSe_2$ CNC solar cells with PCE reaching 2.6 % have been fabricated in a similar way to the case of $AgBiS_2$ CNC solar cells. In the last part of the chapter, a hybrid method is presented for the synthesis of alloyed quaternary AgBiSSe CNCs. It is shown that the optical properties of the alloyed quaternary CNCs can be tuned simply by changing the selenium-to-sulfur precursor ratio.

2

Synthesis of $AgBiS_2$ CNCs under Ambient Conditions

$AgBiS_2$ has been proposed as a promising non-toxic material for solution-processed solar cells thanks to its attractive optical properties, such as a high absorption coefficient (10^3 - 10^5 cm^{-1}) and a suitable bandgap for single-junction solar cells ($\sim$ 1.3 eV). [110] Early reports based on Successive Ionic Layer Adsorption and Reaction (SILAR) [75] and spray deposition [82] of $AgBiS_2$ as a light harvesting layer in solar cells could yield a maximum PCE of 1.7 %. With the utilization of hot injection method for the synthesis, PCE of $AgBiS_2$ CNC solar cells has been boosted to 6.3 %, proving to be a promising contender for non-toxic solution-processed solar cells. [110]

Despite $AgBiS_2$ is a non-toxic and relatively abundant material, the requirement for costly chemical precursors (such as HMS - hexamethyldisilathiane) along with the use of high temperature, vacuum and noble gases in the synthesis remain as an effort-demanding problem to solve. This problem has to be tackled for the commercial viability of this technology as the synthesis-related cost is a major bottleneck for the successful commercialization of solar cells based on colloidal quantum dots/nanocrystals. [111]

Thus, it is evident that a cost-effective synthesis and processing approach has to be devised for a commercially reliable photovoltaics technology. The main objective of this Chapter is to present a low-cost versatile synthesis method for $AgBiS_2$ CNCs that benefits from the air-insensitive precursors and low reaction temperatures under ambient conditions to overcome the issues related to the traditional colloidal synthesis methods that require Schlenk-line setup.

Although it is not easy to circumvent the requisite of protective reaction environment for every kind of nanocrystals due to oxidation and degradation, $AgBiS_2$ CNCs offer a unique opportunity thanks to their inertness under ambient conditions. [112] By taking advantage of the inertness of $AgBiS_2$ CNCs, there has been few attempts showing ambient synthesis of $AgBiS_2$ CNCs. Lei et al. demonstrated the possibility of synthesizing very small $AgBiS_2$ colloids at room temperature using polyethylenimine as the ligand for in vivo imaging and photothermal therapy. [113] Later, Mak et al. published a study on graphene transistors sensitized with $AgBiS_2$ CNCs synthesized under ambient conditions, although the preparation of the precursor solution still required a temperature of 120 °C. [114] However, the production of solar cell-grade $AgBiS_2$ CNCs performed entirely at room temperature and under ambient conditions has remained elusive. In this thesis, we concomitantly address the aforementioned challenges by developing a solution-processed solar cell that is based on environmentally friendly $AgBiS_2$ CNCs that are produced via low-cost, readily up-scalable synthetic chemistry under ambient conditions at room temperature using only commercially available precursors.

As the previously reported hot-injection synthesis requires a high reaction temperature and an air-sensitive sulfur precursor to achieve photovoltaics-quality nanocrystals, the use of a protective environment becomes obligatory. To overcome the limitation for inert reaction environment, we sought to use air-stable precursors that can be activated at room temperature. There are various strategies that have been employed in previous studies to overcome the limitations enforced by air-sensitive sulfur precursors. A very common strategy utilized in the literature is to use a solution of elemental sulfur in amines [115–117] as it is less harmful and less sensitive to ambient conditions compared to alternatives such as dialkyldithiocarbamates, carbon disulfide (CS_2) and thioacetamide. [118–120] Moreover, it is advantageous to utilize cheap, abundant and non-toxic materials as precursors to lower the cost and the environmental risks related to manufacture and disposal of the photovoltaics. Because of the benefits of this sulfur precursor, we designed our synthesis approach around the reaction paths offered by the sulfur-amine chemistry.

Despite the main role of amines in the designed reaction is the activating agent for

the elemental sulfur, they can also act as soft ligands during the synthesis to prevent nuclei from coalescing; hence, no other chemicals are needed for the nucleation and growth of the CNCs, providing a way for simpler reaction mechanisms due to the involvement of less chemical moieties in the reaction environment.

In this Chapter, we present a synthesis method for $AgBiS_2$ CNCs that does not necessitate air-free reaction medium or heating. In the first part, we show the effect of the synthesis duration on $AgBiS_2$ CNCs to demonstrate the speed of the proposed synthesis route. The second part of this Chapter focuses on the purity of the obtained $AgBiS_2$ CNC dispersion with a special emphasis on the formation of secondary products, such as metallic or binary phases. In addition, a study on the conversion of metallic and binary phases to $AgBiS_2$ is provided to demonstrate that $AgBiS_2$ is the most thermodynamically-favored product of the proposed synthesis scheme. In the following section, the proposed reaction route is examined in detail in terms of its response towards the use of different alkyl amines that act as both the reaction medium and the ligand during nanocrystal nucleation and growth. It is shown via TEM and XRD results that the CNC size can be reduced by the use of longer alkyl amines, which demonstrates that the tailoring of the nanocrystals size is possible in this method. In the last part of this Chapter, we give some insights into the proposed reaction mechanism utilizing n-octylamine with elemental sulfur and metal iodide salts.

2.1 Room-temperature synthesis of $AgBiS_2$ CNCs

As the first step in designing the synthesis method, we checked the effect of reaction time on the nanocrystal properties. For this purpose, four different $AgBiS_2$ CNC batches were prepared using the same amount of precursors, but under different reaction times. After the end of the reaction, the nanocrystals were purified via addition of an antisolvent and centrifugation (see Appendix A for further details). For characterization, TEM and absorption spectroscopy were utilized to monitor the effect of the reaction time on the size and absorption characteristics of the resulting nanocrystals (Figure 2.1). The results demonstrated that the synthesis of $AgBiS_2$ CNCs at room temperature did not require long reaction duration thanks to fast reaction among amine-sulfur complex and silver/bismuth iodide salts. This type of fast reaction at room temperature was presented for $AgBiS_2$ CNCs in the literature previously. [113] One of the main observations of this experiment was that the nanocrystals did not exhibit any pronounced difference in the absorption spectra for varying reaction times. A slight increase in nanocrystal size was observed for reaction times of 5 and 20 minutes (average nanocrystal size was measured to be 3.25 and 3.47 nm for the synthesis duration of 5 and 20 minutes,

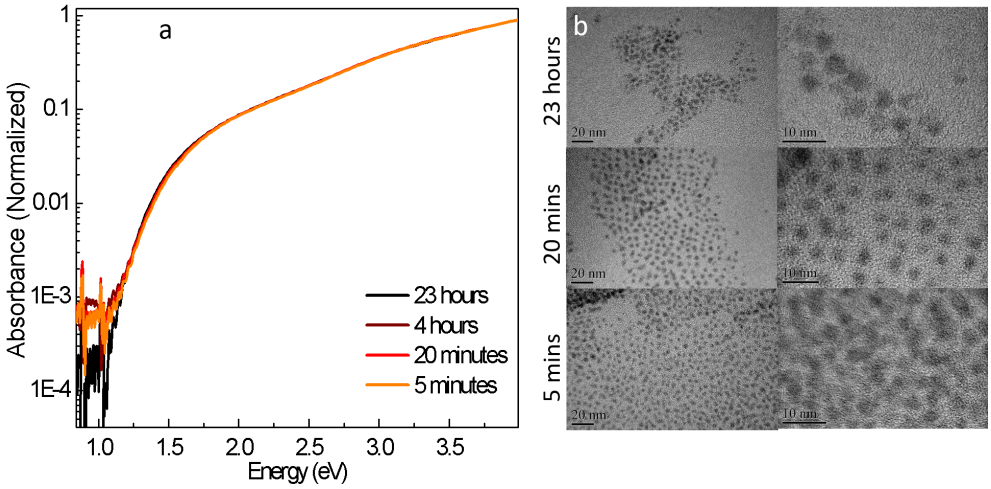

Figure 2.1: Effect of the reaction time on nanocrystal growth. (a) Absorption spectra and (b) TEM images of $AgBiS_2$ CNCs under different reaction times.

respectively.). However, a noticeable increase of irregularity in nanocrystal shape was detected when the reaction time was increased to 23 hours, giving an average size of 2.87 nm with a noticeably broader size distribution as visible in Figure 2.1. Although shape and size changed from 5 minutes to 23 hours, no noticeable change was observed in the absorption spectra of these nanocrystals, possibly due to very small Bohr radius of $AgBiS_2$.

2.2 Existence of binary and metallic phases in $AgBiS_2$ CNC dispersions

As the second part in understanding the reaction of silver and bismuth iodides with amine-sulfur complex, we performed experiments to determine the relative stability of binary phases versus the ternary $AgBiS_2$ phase. As the first trial, silver and bismuth precursors were prepared by dissolving respective iodide salts in amines. Then, a sulfur solution in amines was added into one of the precursor solutions to initiate the nucleation of nanocrystals. As the next step, the other precursor solution was added into the mixture to convert the binary CNCs into ternary $AgBiS_2$ CNCs. Aliquots were taken after additions to check the progress of the reaction (Figure 2.2a). In the first experiment, we started with the synthesis of colloidal Ag_2S CNCs. The addition of the sulfur precursor into AgI solution initiated the formation Ag_2S CNCs, which could be easily observed via darkening of the color of the mixture. The absorption spectrum of the solution after the addition of sulfur precursor showed the successful

formation of Ag_2S nanocrystals with a relatively small bandgap of around 1 eV. This is expected as the reaction of silver salts with amine-activated elemental sulfur at room temperature is a well-known synthesis method for Ag_2S CNCs. [121, 122] After the addition of the bismuth precursor, the absorption spectrum changed and the optical bandgap increased to 1.2 eV (Figure 2.2a-b). This observation may be taken cautiously as there is another possible route for the interaction of the bismuth precursor with Ag_2S CNCs in the mixture, such as Bi_2S_3 shell-coating on Ag_2S CNCs. Yet, it is known that Ag_2S CNCs exhibit a pronounced quantum confinement effect thanks to the large exciton Bohr radius of Ag_2S, thus any change in nanocrystal size can be easily detected via a change in optical bandgap as long as the nanocrystal radius is comparable to its exciton Bohr radius. It has been reported that Ag_2S CNCs with a size of 2.8 nm have a PL peak around 1.2 eV whereas the ones with a size of 14 nm have PL peak around 1.0 eV. [123] Hence, any Bi_2S_3 shell-coating on the surface of the existing Ag_2S CNCs should have resulted in a bandgap lower than that of the starting Ag_2S nanocrystals (1 eV in this case) due to larger overall nanocrystal size. Thus, the increase in bandgap cannot be attributed to the deposition of a Bi_2S_3 shell on Ag_2S CNC surface, but to the conversion of Ag_2S CNCs into $AgBiS_2$ CNCs. Although conversion from a binary phase to ternary phase at room temperature and under ambient conditions seems unlikely at first glance, a study published in 2016 presented a similar reaction in which a mere addition of an indium salt and a mediating agent into the nanocrystal dispersion under similar conditions was sufficient for complete conversion of Ag_2S CNCs into $AgInS_2$ CNCs. [123]

When the same experiment was repeated in reverse order, first Bi_2S_3 CNCs with a bandgap close to 1.4 eV were formed at the initial stage (Figure 2.2a). The absorption spectrum of these CNCs was found to have a distinctive feature around 600 nm, which is not present in the absorption spectrum of colloidal $AgBiS_2$ CNCs. [110, 124] After the addition of the silver precursor, the absorption profile of the CNC dispersion shifted towards longer wavelengths, coinciding with that of $AgBiS_2$ CNCs. Yet, this small change in absorption spectrum, due to similar bandgaps of Bi_2S_3 and $AgBiS_2$ CNCs, was found to be insufficient to support the claim that the conversion of Bi_2S_3 into $AgBiS_2$ CNCs was possible. To verify the conversion process, XRD spectra of the samples were collected after the purification of the resulting nanocrystals. XRD results indicated that the conversion was successful even at room temperature under ambient conditions (Figure 2.2c). This result is in accord with a recently published study that has shown that the conversion of Bi_2S_3 CNCs into $AgBiS_2$ CNCs is possible with the use of Ag-thiol chemistry at slightly elevated temperatures. [125] Here, it should be also noted that no traces of initial CNC populations was encountered in XRD spectra

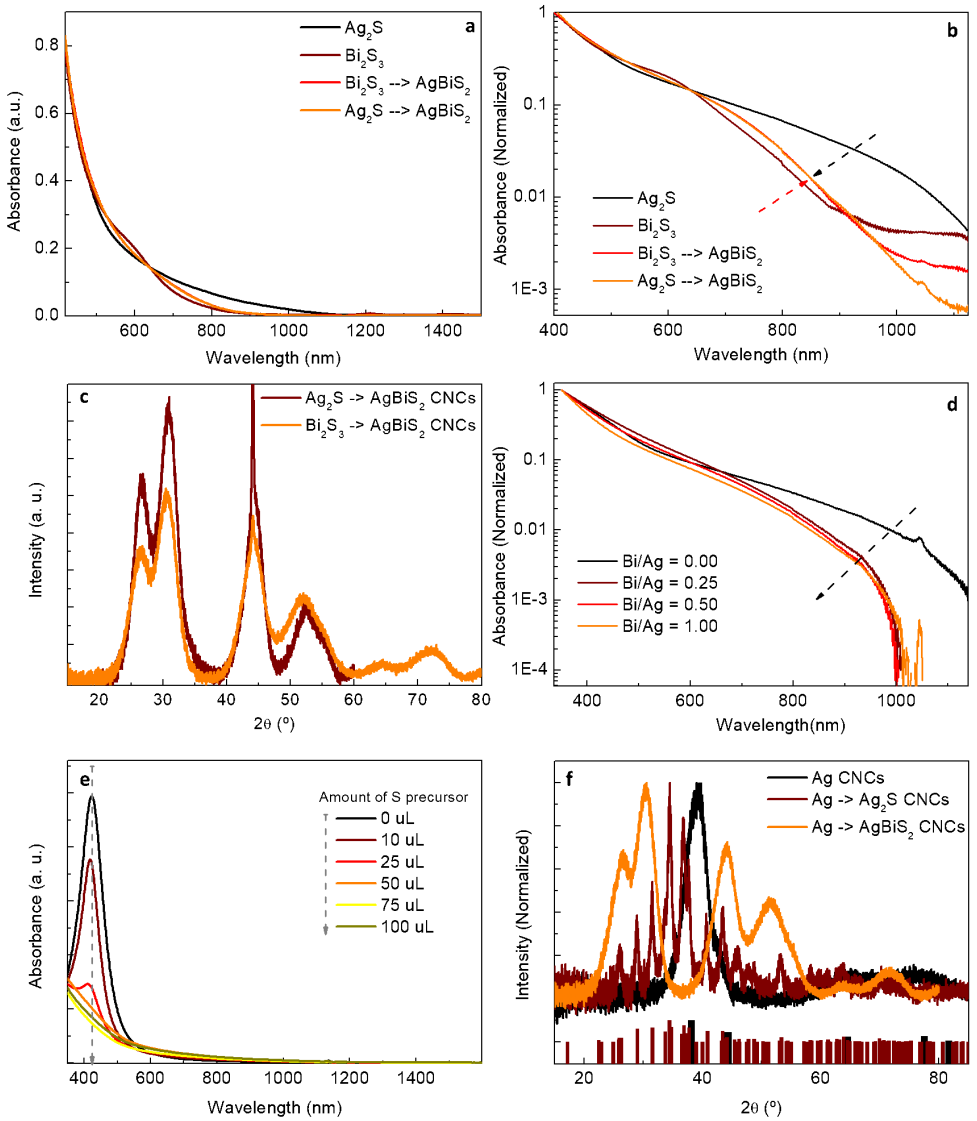

Figure 2.2: Conversion of metallic and binary phases into ternary phase. (a)Absorption spectra of solutions after the addition of each precursor into the first metal precursor solution in linear scale (Black: S into AgI forming Ag_2S CNCs, Brown: S into BiI_3 forming Bi_2S_3 CNCs, Red: AgI into Bi_2S_3 CNCs and Orange: BiI_3 into Ag_2S CNCs). (b) The same plot (a) given in logarithmic scale to emphasize the change in the long wavelength range after each process. (c) XRD spectra demonstrating the conversion of the Ag_2S and Bi_2S_3 CNCs into $AgBiS_2$ CNCs with the addition of the required precursors into the reaction mixture. (d) Absorption of the solutions after the addition of each portion of bismuth precursor into Ag_2S CNCs dispersion. (e) Absorption of the commercial Ag CNC dispersion before (black) and after the addition of various amounts of sulfur (brown) and bismuth + sulfur (orange) precursor. (f) XRD spectra of Ag CNCs before and after the addition of the respective precursors (Brown bars: peaks of Ag_2S in bulk, black bars: peaks of Ag in bulk).

after conversion and cleaning steps, which shows the benign nature of this method for the synthesis of $AgBiS_2$ CNCs.

In the second part, a supplementary experiment was performed to show the gradual conversion of Ag_2S CNCs into $AgBiS_2$ CNCs by addition of bismuth precursor in small portions instead of adding all at once to have a better insight into this conversion process. Our results demonstrated that the change in absorption spectrum was observable even for a Bi/Ag ratio of 0.25 (Figure 2.2d). This suggests that the ternary $AgBiS_2$ phase is more thermodynamically-favorable and more probable to form in this reaction compared to the binary Ag_2S and Bi_2S_3 phases. This shows that the ternary phase is the major product of this synthesis method as long as there is sufficient amount of both of the metal precursors in the reaction mixture to promote the formation of ternary CNCs.

In the last part, we explored the possibility of having Ag CNCs in the final dispersion as a side product of this reaction. Ag CNCs are known to the scientific community for a long time and their optical properties are very well-known. [126, 127] The strong plasmonic feature in their absorption spectrum makes it easy to detect their presence in a colloidal dispersion by optical spectroscopy. Although no plasmonic peak was observed in the absorption spectrum of our $AgBiS_2$ CNCs within the detection limit of the instruments used, we decided to verify that Ag CNCs, which may have formed via any side reactions, cannot stay as metallic nanoparticles thanks to the highly reactive nature of the sulfur-amine complex used in our synthesis method. For this purpose, a commercial Ag CNCs solution in hexanes was utilized as the starting material. After repeated purification cycles via the addition of an antisolvent and centrifugation, Ag CNCs were dispersed in toluene and their absorption spectrum was recorded (Figure 2.2e). Ag CNCs had a very strong plasmonic peak around 420 nm before the addition of the sulfur precursor. When a solution of sulfur in amine was added to Ag CNCs dispersion in portions, this strong peak at 420 nm blue-shifted and disappeared gradually in minutes and an absorption spectrum, which is very similar to that of Ag_2S CNCs, was observed. This change in absorption characteristics indicates that Ag CNCs can be converted into Ag_2S CNCs with the addition of sulfur-amine precursor at room temperature. Furthermore, the conversion of Ag CNCs into $AgBiS_2$ CNCs were confirmed by addition of bismuth and sulfur precursors into Ag CNCs in amines. XRD spectra showed that the conversion of Ag CNCs into Ag_2S and $AgBiS_2$ CNCs could be easily achieved with the addition of suitable amount of Bi and S precursors into Ag CNC dispersion (Figure 2.2f). These findings corroborate that our synthesis methodology is not prone to the formation of either Ag CNCs or binary

phases thanks to more thermodynamically-favorable $AgBiS_2$ CNCs compared to other possible products of this synthesis route.

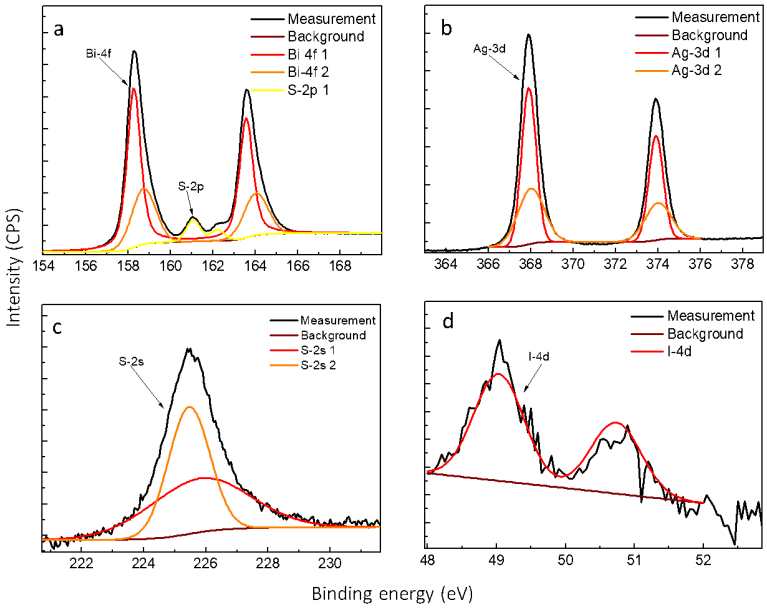

Figure 2.3: XPS analysis of $AgBiS_2$ CNCs synthesized with chloride salts of silver and bismuth and treated with a mixture of thiol and TMAI ligands (a : Bi-4f, b : Ag-3d, c : S-2s, d : I-4d).

2.3 Synthesis of $AgBiS_2$ CNCs with alternative metal salts

As another study, we checked if it was possible to synthesize $AgBiS_2$ CNCs using different halides of silver and bismuth. For this purpose, we utilized silver and bismuth chlorides as the starting materials. After dissolving chlorides of silver and bismuth in n-octylamine, a sulfur solution in amines was injected and the mixture was stirred for homogeneous reaction. Then, $AgBiS_2$ CNCs were purified in a similar way used for $AgBiS_2$ CNCs synthesized using iodide salts. After the synthesis and purification, $AgBiS_2$ CNC films were deposited on clean ITO coated glass via solid-state ligand exchange approach using a mixture of thiol and TMAI as the ligand for X-Ray Photoelectron Spectroscopy (XPS) analysis (Figure 2.3). For the CNCs synthesized from chloride salts, two Bi-4f doublets were observed for the bismuth, one located at 158.3 eV and another at 158.7 eV. In addition, a S-2p doublet at 161.1 eV was detected between Bi-4f doublets. Two doublets were used to fit the spectrum of Ag-3d, with locations of

367.9 and 368.0 eV. For sulfur, two singlets (at 225.5 and 226.0 eV) were used to fit S-2s spectrum. XPS analysis yielded an elemental ratio of Bi/Ag and S/Ag of 1.96 and 1.92, respectively. The presence of both Ag and Bi indicates that chloride salts can form $AgBiS_2$ CNCs as it has been already demonstrated in the previous section that the ternary phase is the most thermodynamically-favored product in this synthesis route. Yet, it was observed that the chloride salts caused an increase in bismuth content of $AgBiS_2$ CNCs (Table 2.1). In addition, a very weak I-4d signal was detected with a I/Ag ratio of 0.04, which is possibly due to the residue left by TMAI ligand used in the film deposition process. This is an expected result since the surface of $AgBiS_2$ CNCs are terminated by thiols after the reaction and TMAI ligands cannot replace thiols attached on the surface of the nanocrystals in a simple solid-state ligand exchange process performed under ambient conditions.

Table 2.1: Elemental ratios (normalized to Ag-3d) of $AgBiS_2$ CNCs synthesized using chloride salts of silver and bismuth and treated with a mixture of thiol and iodide ligands.

Ag	Bi	S	I
1.00	1.96	1.92	0.04

2.4 Effect of ligands on $AgBiS_2$ CNCs

Up to this point, we explored the synthesis conditions in terms of reaction time and observed that $AgBiS_2$ CNCs could be formed even with a reaction time of as short as 5 minutes at room temperature. We confirmed experimentally that the ternary phase is the main product of the ambient condition synthesis. We also verified that other metal halides could also be used as the metal precursors. Thus, there remains one parameter to be checked for a complete exploration of the parameter space for this synthesis route. In the current synthesis method, amines are used both as the reaction medium and as the ligands during the formation of the nanocrystals. As the ligands used during the nucleation and growth of nanocrystals can have an effect on the nanocrystal size and shape, we performed the synthesis of $AgBiS_2$ CNCs using amines with different chain length to probe the effect of the ligands. Thanks to the solubility of the silver and bismuth iodides in amines, we could successfully cover a wide range of n-alkyl amines with varying chain length, starting from 4-carbon n-butylamine up to 18-carbon oleylamine. For all amines utilized in this study, colloidal $AgBiS_2$ nanocrystals could be obtained (Figure 2.4a). Transmission electron microscopy (TEM) images indicated that the size of the nanocrystals can be increased by employing shorter chain amines, as expected, thanks to the lower steric hindrance effect of shorter carbon backbone. [128]

The crystal size of the respective $AgBiS_2$ CNCs dispersions was also confirmed via X-Ray Diffraction (XRD) measurements using Sherrer equation.

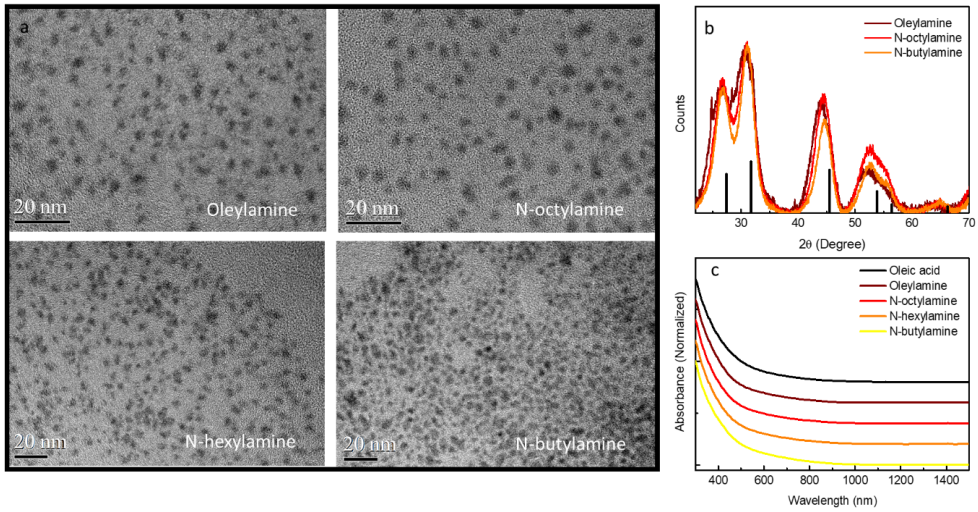

Figure 2.4: Structural and optical characterization of room-temperature $AgBiS_2$ nanocrystals. (a) TEM images showing the shapes of nanocrystals synthesized using different amines (upper left: oleylamine, upper right: n-octylamine, lower left: n-hexylamine and lower right: n-butylamine), (b) XRD spectra of $AgBiS_2$ nanocrystals synthesized via our new room-temperature technique using different amines (Brown: oleylamine red: n-octylamine, orange: n-butylamine) (Black bars show the peak positions of the bulk $AgBiS_2$) and (c) Comparison of the absorbance spectra of $AgBiS_2$ nanocrystals in octane which are synthesized via different methods (Black: via Schlenk-line; brown, red, orange and yellow: room-temperature method using oleylamine, n-octylamine, n-hexylamine and, n-butylamine respectively. Curves are plotted with offset for ease of viewing.).

$$d = \frac{K\lambda}{\beta \cos(\theta)} \tag{2.1}$$

Here, d is the crystal size, K is a dimensionless shape factor (0.9), λ is the wavelength of the X-ray source (0.15046 nm), β is the full-width at half maximum in radians and θ is the Bragg angle. The tuning range of the nanocrystal size was found to be 2.5-3.3 nm for oleylamine and n-butylamine, respectively (Table 2.2 and Figure 2.4b).

Table 2.2: Size comparison of $AgBiS_2$ nanocrystals synthesized via Schlenk-line and room-temperature methods using different amines with metal iodide precursors. The nanocrystal size decreases with increasing chain length of the amine.

Sample	Nanocrystal Size (XRD) [nm]	Nanocrystal Size (TEM) [nm]	Standard Deviation (TEM) [nm]
Oleic acid	4.34	4.6	0.94
N-butylamine	3.11	3.26	0.93
N-octylamine	2.53	2.96	0.90
Oleylamine	2.55	2.54	0.82

As it can be seen from Figure 2.4c, the absorption characteristics of the $AgBiS_2$ CNCs measured in solution are very similar for hot-injection and room-temperature synthesis methods. A bandgap of 1.2 eV is extracted from the Tauc plot for room-temperature nanocrystals, which is suitable for single-junction photovoltaics (Figure 2.5). Although it is possible to perform synthesis with all the ligands listed above, we found that n-octylamine was the best among the amines utilized in this study for the synthesis of $AgBiS_2$ CNCs. This choice was made thanks to the combined advantages of commercial availability, low cost, low evaporation rate and suitable viscosity of n-octylamine at room temperature, which makes this ligand less costly and easier to work with (Table 2.3). For this reason, we optimized the rest of our processes for the fabrication of photovoltaic devices using the nanocrystals synthesized in n-octylamine with elemental sulfur and metal iodide precursors.

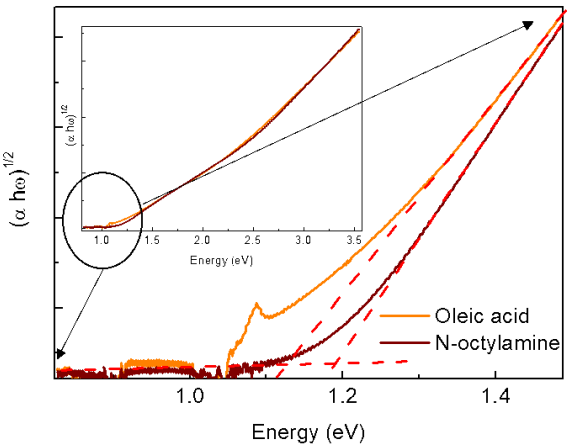

Figure 2.5: Tauc plots of Schlenk-line (Orange: oleic acid) and room temperature (Brown: n-octylamine with metal iodide precursors) $AgBiS_2$ nanocrystals. Although in the high-energy portion of the spectrum both curves overlap, they show noticeable difference in the low-energy region. Room-temperature nanocrystals have a sharper decrease compared to Schlenk-line nanocrystals towards longer wavelength.

Table 2.3: Boiling point, vapor pressure and price of n-butylamine, n-hexylamine, n-octylamine and oleylamine.

Ligand	Boiling Point (°C)	Vapor Pressure (mmHg)	Cost (/ml)
N-butylamine (99 %)	78	68 @ 20 °C	0.026
N-hexylamine (99 %)	131	7.95 @ 20 °C	0.229
N-octylamine (99 %)	175	1 @ 20 °C	0.116
Oleylamine (98 %)	350	8 @ 135 °C	0.142

Table 2.4: XPS analysis (Normalized to Ag-3d peaks) of $AgBiS_2$ nanocrystals synthesized via Schlenk-line (oleic acid, treated with TMAI) and room temperature (n-octylamine with metal iodide precursors, treated with ethanethiol) methods. The results show that Schlenk-line method gives Ag-rich nanocrystals whereas room-temperature method yields Bi-rich nanocrystals.

Sample	Ag (3d)	Bi (4f)	S (2p)
Oleic acid	1.00	0.78	1.05
N-octylamine	1.00	1.30	1.49

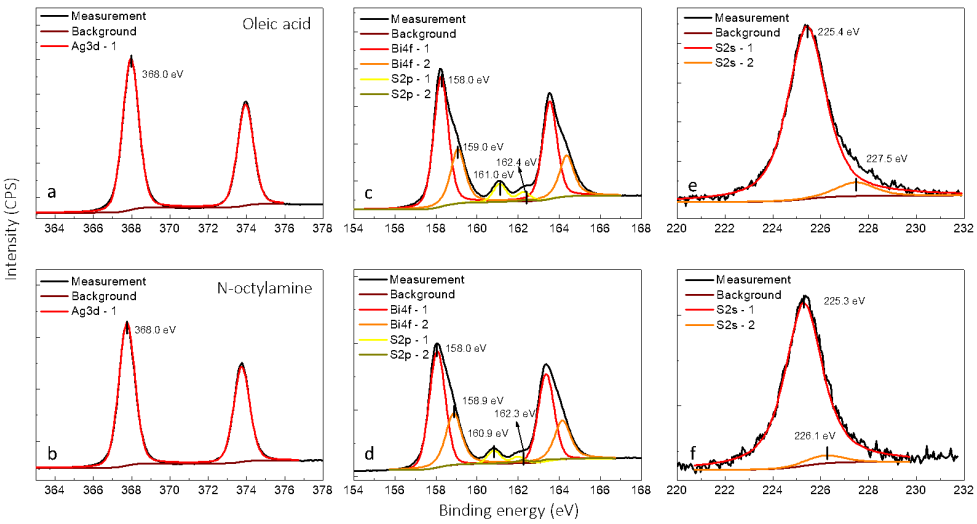

Figure 2.6: XPS scans of $AgBiS_2$ nanocrystals synthesized via Schlenk-line (a: Silver-3d, c: Bismuth-4f and e: Sulfur-2s) and room temperature (b: Silver-3d, d: Bismuth-4f and f: Sulfur-2s) methods. All the major peaks were found to have very similar binding energies for room temperature and Schlenk-line $AgBiS_2$ nanocrystals.

XPS analysis showed that $AgBiS_2$ nanocrystals synthesized at room-temperature with iodide salts were bismuth-rich (1:1.30) unlike Ag-rich $AgBiS_2$ nanocrystals ob-

tained via hot-injection method (1:0.78) (Table 2.4). [110] Ag-3d gave a single doublet (at 368.0 eV, Figure 2.6a-b) for both types of nanocrystals. Two doublets were required to fit the bismuth-4f peaks (at 158.0 & 159.0 eV, the ratios of the areas of the doublets were 0.53 for room temperature and 0.46 for Schlenk-line nanocrystals, Figure 2.6c-d). The main component of S-2s signal of room-temperature nanocrystals showed a small shift from that of Schlenk-line nanocrystals (225.3 and 225.4 eV. See Figure 2.6e-f). Moreover, the sulfur content of the room-temperature nanocrystals was found to be higher than that of Schlenk-line nanocrystals (1.49 vs. 1.05), which may result from the presence of thiols on the surface.

2.5 Proposed reaction mechanism for room-temperature synthesis of $AgBiS_2$ CNCs

The activation of elemental sulfur by amines is a key step in the synthesis of metal sulfide nanocrystals at room temperature. According to a study published in the literature, elemental sulfur forms alkylammonium polysulfides when dissolved in amines at low temperatures. [129] Although elemental sulfur is not sufficiently reactive towards silver and bismuth iodides at room temperature, alkylammonium polysulfides can react with these metal iodides under ambient conditions. As the solubility of Ag-sulfide and Bi-sulfide monomers is negligible in amines, the nucleation of $AgBiS_2$ occurs, which is manifested by gradual darkening of the reaction mixture. After the reaction, in-situ formed iodine/iodide is dissolved by the amines, possibly iodine forming a charge transfer (CT) complex with amines as described in a previous study. [130] Our findings support that alkyl ammonium iodide salts are formed as the byproduct of this reaction (Figure 2.7).

To gain insight into the nature of this reaction, we first probed the interaction of cation precursors with amines. Fourier-transform Infrared (FTIR) spectroscopy was performed on samples prepared by spin coating AgI (0.4 M), BiI_3 (0.4 M) and AgI-BiI_3 (0.2 M each) solutions in n-octylamine onto clean double side polished silicon wafers. Our findings showed that AgI did not cause any significant alteration in the FTIR spectrum of n-octylamine, indicating that AgI did not interact with n-octylamine strongly (Figure 2.7a). BiI_3 caused a small shift of the N-H peak probably due to a stronger interaction of BiI_3 with the nitrogen of the n-octylamine molecule (from 3331 cm^{-1} for only n-octylamine to 3319 cm^{-1} for 0.4 M BiI_3). This redshift of N-H peak is very similar to the observations reported previously on PbS-butylamine [72] and $MAPbI_3 \cdot DMSO$ [131] systems. Although BiI_3 interacts with n-octylamine, this interaction could be easily overcome by slight heating of the film. After a mild heat treatment at 90 °C, no signal from n-octylamine was detected, indicating the

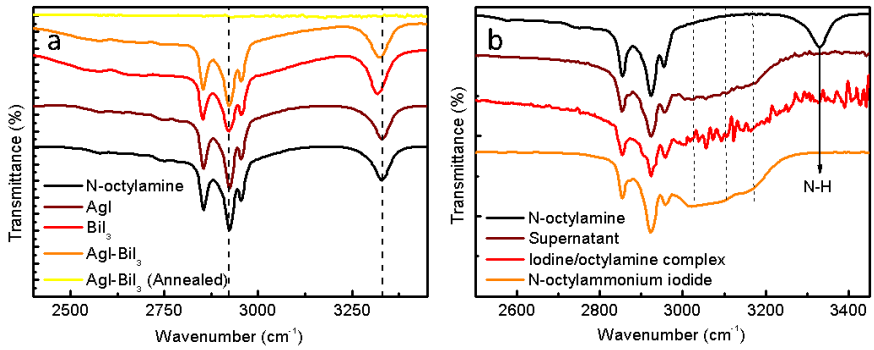

Figure 2.7: FTIR examination of precursors and reaction byproducts. (a) FTIR response of the metal iodide precursors spun coated from n-octylamine (black: n-octylamine, brown: AgI, red: BiI_3, orange: AgI-BiI_3 mixture and yellow: AgI-BiI_3 mixture after annealing), (b) FTIR analysis of the reaction byproducts (brown), of iodine-amine complex (red) and of n-octylammonium iodide (orange) showing the resemblance of the FTIR spectrum of the reaction byproducts to those of iodine/n-octylamine CT and n-octylammonium iodide salt (Curves are plotted with offset for ease of viewing.).

complete removal of the organics from the film. To verify our proposed reaction path, the supernatant obtained during the purification of nanocrystals was used to examine the reaction byproducts. The obtained supernatant was directly spun coated on to a clean silicon wafer and annealed. After heat treatment, free n-octylamine evaporated and left behind a solid residue on the substrate. The absence of a strong N-H peak around 3300 cm^{-1} for this residue indicated that this compound was formed by the interaction of nitrogen of the n-octylamine with the precursors or with the byproducts of the reaction (Figure 2.7b). However, from Figure 2.7a it is evident that AgI - BiI_3 - amine interaction can be easily ruptured by a mild heat treatment, liberating free amines. Hence, the disappearance of the N-H peak cannot be attributed to the interaction of amines with the metal iodides. To investigate this mechanism further, an iodine-amine solution was prepared under ambient conditions and spun coated on a silicon wafer. The difference in the FTIR spectra before and after heat treatment indicated the formation of a stable iodine-amine interaction, which was demonstrated by the formation of a shoulder around 3050 cm^{-1} and disappearance of the N-H peak around 3330 cm^{-1}. The resemblance of the spectrum of the iodine-amine complex to the spectrum of the supernatant suggests that iodine-amine complex is a byproduct of this reaction. Here, it should also be noted that iodine-amine complexes are prone to transformation into alkylammonium iodide salts in the presence of moieties which are naturally present in ambient air, such as moisture, [132] and that alkylammonium iodide salts possess an infrared response similar to that of the iodine-amine complexes (Figure 2.7b). Given

that the solvents were used without drying and that all the synthesis, purification and sample preparation steps were carried out in air, it is likely that the iodine-amine complex present in the supernatant was transformed into alkylammonium iodide salt during the course of the reaction, thus making alkylammonium iodide salts a major byproduct of this reaction.

3

$AgBiS_2$ CNC Photovoltaics via Ambient Synthesis Method

In Chapter 2, the parameter space for the reaction of metal halide salts with elemental sulfur in amines was discussed in detail. Under the light of the findings of Chapter 2, it was found advantageous to employ elemental sulfur, metal iodide salts and n-octylamine as the precursors and reaction medium for the ambient condition synthesis of $AgBiS_2$ CNCs, respectively. This Chapter focuses on the optoelectronic studies performed on $AgBiS_2$ CNCs obtained via this synthesis route to show the promising features of this new method.

Although long ligands are effective in forming colloidally-stable nanocrystal dispersions, it is required to have shorter ligands on the surface of the nanocrystals to facilitate the charge transfer in a photovoltaic device. In a study reported previously, [110] a tetramethylammonium iodide (TMAI) treatment was utilized to exchange long oleate groups on the surface of $AgBiS_2$ CNCs with iodide ions. However, the deposition of multiple layers of $AgBiS_2$ CNCs with TMAI treatment alone is not possible in our case due to the high chemical affinity of 1-octanethiol towards silver and bismuth cations

compared to the iodide anions. To overcome this issue, we developed a new ligand exchange strategy based on alternative ligands for the removal of long and insulating 1-octanethiol from the nanocrystal surface. To show the importance of our findings, a detailed study on different ligand exchange strategies is presented to demonstrate the change in device performance with respect to the ligand used in the CNC film formation. To highlight the origin of the difference, we make extensive use of optoelectronic characterization methods, such as current-voltage (J-V) measurements under dark and light bias and external quantum efficiency (EQE) measurements. Then, a more detailed characterization of the optimized structure is provided via utilization of advanced techniques, such as light intensity dependent J-V measurements, transient photovoltage (TPV) and transient photocurrent (TPC). In addition, we present information about the morphology of the devices using both planar and cross-sectional scanning electron microscopy (SEM) images to show the quality of the room-temperature $AgBiS_2$ CNC thin films.

In the first part of this Chapter, a ligand study for $AgBiS_2$ CNCs that are prepared via ambient synthesis method is presented. First, we show through both FTIR and optoelectronic studies that the 1-octanethiol molecules bound to the CNC surface can be removed partially with the use of ZnI_2 treatment. ZnI_2-treated $AgBiS_2$ CNC solar cells yielded a PCE of only 3.1 %, possibly due to the incorporation of zinc into the film. In the second part, we focus our attention onto thiol ligands as they are chemically less aggressive towards $AgBiS_2$ CNCs. The solar cells that were prepared by treatment with different alkyl thiols showed higher PCE compared to the solar cells that were prepared with ZnI_2 treatment. Among all the thiol ligands studied in this part, ethanethiol-treated $AgBiS_2$ CNC solar cells gave the highest PCE of 5.5 %, which is close to the record PCE of 6.3 % for the best-performing $AgBiS_2$ CNC solar cell upto date. [110] In the following part of this Chapter, we provide the reader with the results of the optoelectronic characterization that were performed on the ethanethiol-treated solar cell. Through use of optoelectronic characterization techniques, we show that the ethanethiol treatment plays an important role in reducing the trap-assisted recombination by passivating the surface defects of $AgBiS_2$ CNCs synthesized in ambient conditions. In the last part of this Chapter, a simple calculation is provided to show the lower cost of this method compared to the hot-injection methods thanks to the replacement of costly precursors with the cheaper and more air-stable alternatives.

3.1 ZnI_2 as a ligand for $AgBiS_2$ CNC solar cells

As ligand exchange constitutes an important part of CNC film formation that can affect optoelectronic properties of the resulting device, an extensive study was carried out to choose the best ligand to achieve the optimum photovoltaic performance from $AgBiS_2$ CNC solar cells. For this purpose, we tried different molecules from different ligand families, such as metal iodides and thiols. Among different iodide ligands, including tetramethylammonium iodide (TMAI), zinc iodide (ZnI_2) and bismuth iodide (BiI_3), only ZnI_2 was found to yield an acceptable efficiency of more than 3 % (Figure 3.1). In addition to an acceptable PCE of 3.1 % thanks to the replacement of thiols with iodide, it was discovered that ZnI_2 treatment introduced Zn into the $AgBiS_2$ CNC film, possibly due to a partial cation exchange with Bi on the surface of the CNCs. The incorporation of cation of the ligand into the film can be explained with the higher reactivity of ZnI_2 compared to other iodide ligands, such as TMAI. From this perspective, it behaves different from the other iodide ligands in terms of chemical behavior. [133] Because of these reasons, we found beneficial to include the results of solar cells prepared via ZnI_2 treatment into this study to provide the reader with a more profound understanding of the ligand chemistry of these nanocrystals for further improvement of the device performance.

FTIR measurements demonstrated that ZnI_2 could replace some of 1-octanethiol on the surface of the nanocrystals (Figure 3.1a). However, the presence of the peaks in the range 2800-3000 cm^{-1} hinted that the ligand exchange process was not complete as these peaks correspond to C-H modes that are present in 1-octanethiol molecules. [134] The best result obtained through the use of ZnI_2 ligand was 3.1 %, with a V_{OC} of 0.46 V, a J_{SC} of 11.5 mA cm^{-2} and a fill factor of 0.58 (Figure 3.1b). Although V_{OC} of 0.46 V is close to the value reported before, a J_{SC} of 11.5 mA cm^{-2} falls very short of the best J_{SC} reported previously, thus raising questions about the effectiveness of this ligand for $AgBiS_2$ CNCs. [110] EQE curve showed that these solar cells could absorb photons effectively in the visible spectrum, however, near infrared photons were not absorbed to a significant degree due to diminishing absorption of the film in this spectral region (Figure 3.1c). In addition, the peak in the 600 - 650 nm region in EQE spectrum was suppressed compared to the one reported for Schenk-line $AgBiS_2$ CNCs. This also hinted at reduced carrier transport efficiency within the $AgBiS_2$ CNC layer. The calculated J_{SC} from EQE curve was found to be 13.8 mA cm^{-2}, which was more than the measured value of 11.5 mA cm^{-2}. This also supports that some of the carriers were lost in the transport process, possibly due to limited mobility-lifetime product in these films. The device statistics showed that the majority of the devices gave an efficiency in the 2.5 - 3.0 % range when the devices were prepared with ZnI_2 (Figure

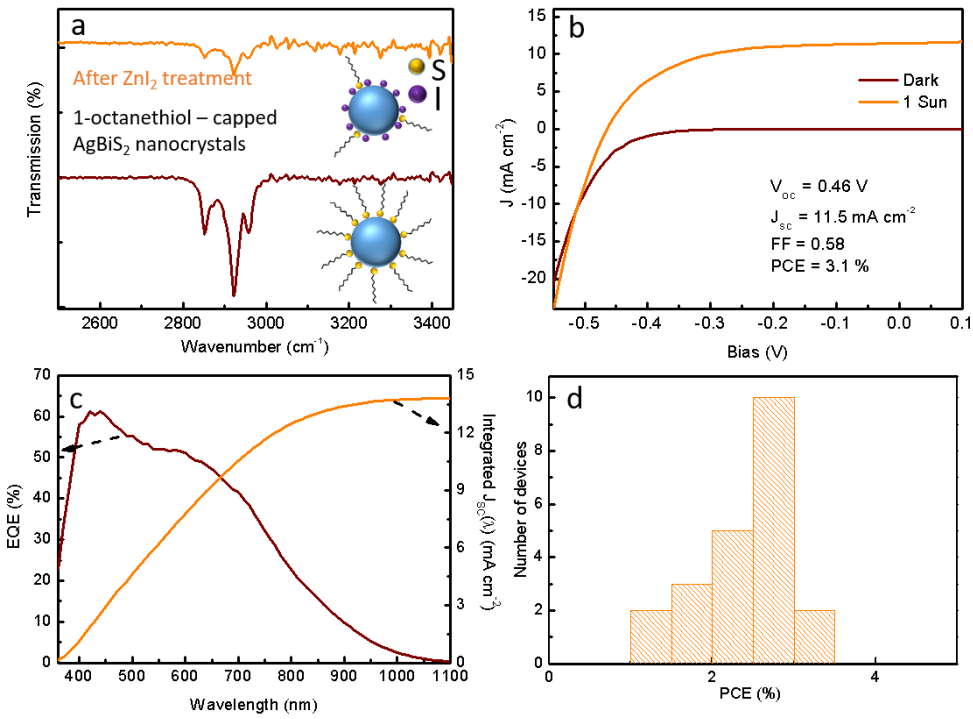

Figure 3.1: Effect of ZnI_2 on device characteristics of $AgBiS_2$ CNCs. (a) FTIR study showing the incomplete removal of 1-octanethiol from the surface of the nanocrystals treated with ZnI_2, (b) J-V curves in dark and under 1 Sun light bias, (c) EQE curve and (d) devices statistics of $AgBiS_2$ CNC solar cells treated with ZnI_2.

3.1d).

Table 3.1: Elemental content of $AgBiS_2$ NCs treated with ZnI_2 (Normalized to Ag-3d).

Ag	Bi	S	I	Zn
1.00	1.08	1.06	0.46	0.11

XPS analysis revealed that the films of $AgBiS_2$ CNCs prepared with ZnI_2 contained significant amount of I although the film was rinsed with methanol (an effective solvent for ZnI_2) after ligand treatment (Table 3.1). This suggests that ZnI_2 can replace 1-octenthiol on the surface of these CNCs, although this replacement is not complete as shown by FTIR results previously. Moreover, the results demonstrated that Bi/Ag ratio was close to ideal 1.0 as opposed to 1.3 for $AgBiS_2$ CNCs treated with thiol ligands and that Zn was present in the film. Thus, ZnI_2-treatment caused a reduction in the bismuth content of CNCs by replacement of Bi cations on the surface of CNCs with Zn cations (Zn/Ag = 0.11), possibly forming an incomplete ZnS shell on $AgBiS_2$

CNCs. This was also supported by the observation that a higher V_{OC} and a lower J_{SC} were obtained when devices were prepared via ZnI_2 treatment compared to the thiol treated devices (Section 3.2). As ZnS has a relatively larger bandgap and it can form a type-I junction with $AgBiS_2$ CNCs due to position of its energy levels, [135] it is expected that a shell of ZnS can provide better surface passivation, which can yield high V_{OC}. Yet, it can show stronger impedance to charge transport due to its higher bandgap, which may result in lower J_{SC} compared to the devices without ZnS shell.

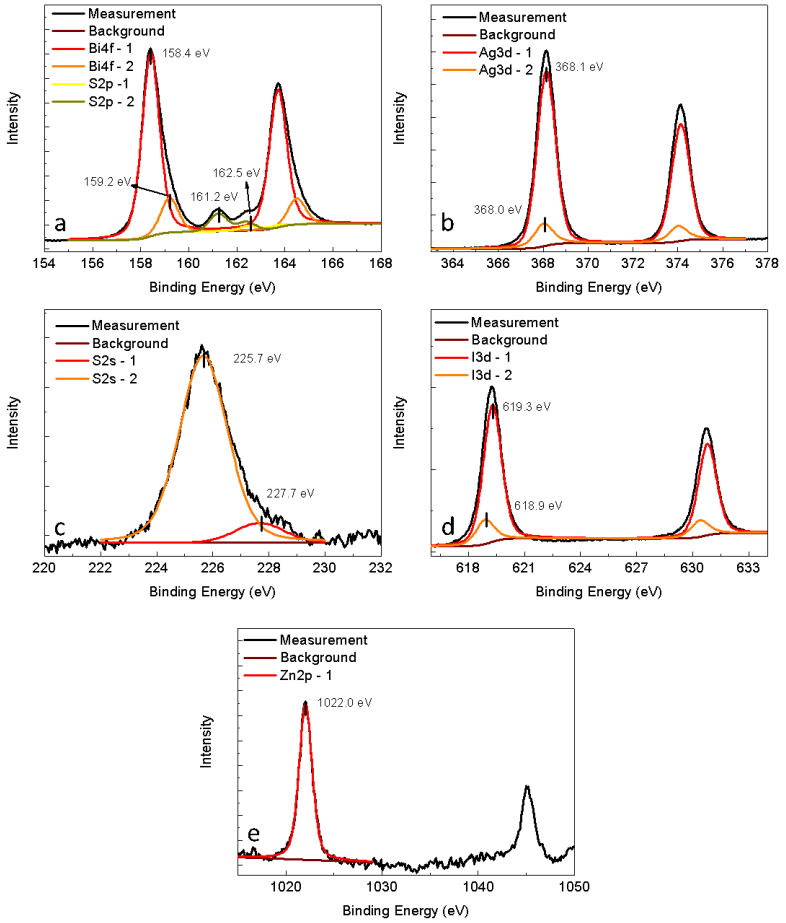

Figure 3.2: XPS analysis of $AgBiS_2$ CNCs treated with ZnI_2 ligand (a: Bi-4f, b: Ag-3d, c: S-2s, d: I-3d and e: Zn-2p spectrum).

In terms of peak positions, XPS spectra did not show any unexpected behavior (Figure 3.2). The peak positions of two Bi-4f doublets were found to be 158.4 and 159.2

eV, respectively. Two doublets resulting from Ag-3d orbitals are located at 368.0 and 368.1 eV. The majority of the S-2s spectrum could be fitted using two singlets (at 225.7 and 227.7 eV), although the contribution of the second peak is very small compared to the main S-2s peak. The fitting of I-3d spectrum required two doublets located at 618.9 and 619.3 eV. The Zn-2p spectrum could be fitted only with one doublet located at 1022.0 eV.

3.2 Thiols as ligands for $AgBiS_2$ CNC solar cells

As $AgBiS_2$ CNCs are already covered by long 1-octanethiol after the synthesis, it is required to choose another ligand that can replace the bound 1-octanethiol molecules to facilitate charge transport within $AgBiS_2$ CNC layer. However, the chosen ligand cannot be very reactive to prevent the surface modification of the CNCs, as in the case of ZnI_2, for it can cause stoichiometric deviations via cation-selective etching. For this reason, it was found advantageous to utilize an organic thiol molecule that is less damaging to the surface of the nanocrystals. It is known that thiols can act as soft ligands for colloidal nanocrystals and this observation has been exploited in many applications. [136, 137] It has been also shown that certain types of nanocrystals can achieve acceptable device performance when treated with short chain thiols to form thin films. [138–140] Thus, we decided to follow this approach and studied the effects of different thiol molecules with different chain length on the photovoltaic performance of $AgBiS_2$ CNC solar cells. First, ligand solutions with equal concentrations were prepared using the following thiols: ethanethiol (ET - 2 carbon), 1-propanethiol (PropSH - 3 carbons), 1-butanethiol (ButSH - 4 carbons) and thiophenol (PhSH, 6 carbons in the form of a benzene ring). Then, solar cells were prepared using these ligand solutions with the same processing parameters to ensure a fair comparison. The chemical structures of these ligands are provided in Figure 3.3 to highlight the differences among these molecules.

Our results indicated that the device performance exhibited a steady decrease with longer carbon backbone of the thiol used for film formation (Table 3.2). For the shortest thiol with 2-carbon backbone (ET), the power conversion efficiency reached a promising value of 4.85 % whereas the device efficiency exhibited a noticeable drop to 4.53 % for the longest carbon backbone ligand (ButSH) used in this study. This shows that the chain length of the ligand has a direct effect on the device performance. This results from the fact that long alkyl groups are inherently electronic insulators. Thus, the existence of these molecules can impede the charge transfer and this can reduce the

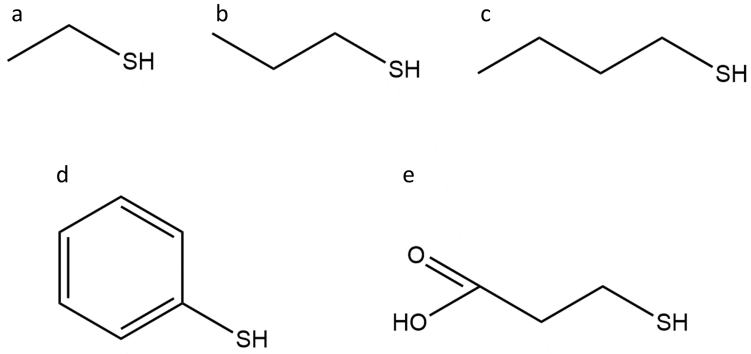

Figure 3.3: Thiol ligands utilized in this study. (a) ethanethiol (ET - 2 carbons), (b) 1-propanethiol (PropSH - 3 carbons), (c) 1-butanethiol (ButSH - 4 carbons) , (d) thiophenol (PhSH, 6 carbons in the forms of a benzene ring) and (e) 3-mercaptopropionic acid (MPA - 3 carbons).

device performance with an efficiency suppressing capacity depending on their length and concentration in the film. In our experiment, we found that the alkyl thiols with relatively short chain length (compared to 1-octanethiol that was already present on the surface of the nanocrystals) were effective in forming photovoltaic-quality $AgBiS_2$ CNC films for efficient photovoltaics.

Table 3.2: Effect of different thiols on the performance of $AgBiS_2$ NC solar Cells.

Ligand	Efficiency (%)	V_{OC} (V)	FF	J_{SC} (mA cm^{-2})	$J_{SC,EQE}$ (mA cm^{-2})
Ethanethiol	4.85	0.44	0.60	18.51	21.04
1-propanethiol	4.76	0.44	0.56	19.41	21.31
1-butanethiol	4.53	0.42	0.54	20.03	21.28
Thiophenol	4.08	0.48	0.56	15.11	17.84

The close similarity of the EQE spectra for all solar cells prepared with alkyl thiols showed that the thickness of $AgBiS_2$ CNC layers in these devices were almost identical as the peaks in EQE spectra are formed due to optical resonance which is a strong function of the thickness of the $AgBiS_2$ CNC layer (Figure 3.4a). Thus, the change in efficiency is not a result of a variation in the thickness of $AgBiS_2$ CNC layer, but a result of the length of the alky group of the ligand utilized for film formation.

We also included an aromatic thiol into the ligand study to test the effect of a benzene ring on the charge transfer in the absorber layer. For this purpose, we utilized the simplest aromatic thiol molecule, which is thiophenol. We found that the solar cell

treated with thiophenol gave a V_{OC} of 0.48 V although the devices prepared with alkyl thiols yielded a V_{OC} in the range of 0.42 - 0.44 V. When we examine closely the EQE spectrum of this device we can see that EQE of this device drops faster in the near infrared region compared to the ones prepared with alkyl thiols. This fast drop in the infrared region of the spectrum was also reflected in lower J_{SC} for this device (both the measured one and the one calculated from EQE spectrum). When combined with the observation that the scaled up version of this EQE curve showed a peak at a very similar wavelength with other devices, it is reasonable to claim that the higher V_{OC} and lower PCE of the device prepared with thiophenol did not stem from different thickness of $AgBiS_2$ CNC layer.

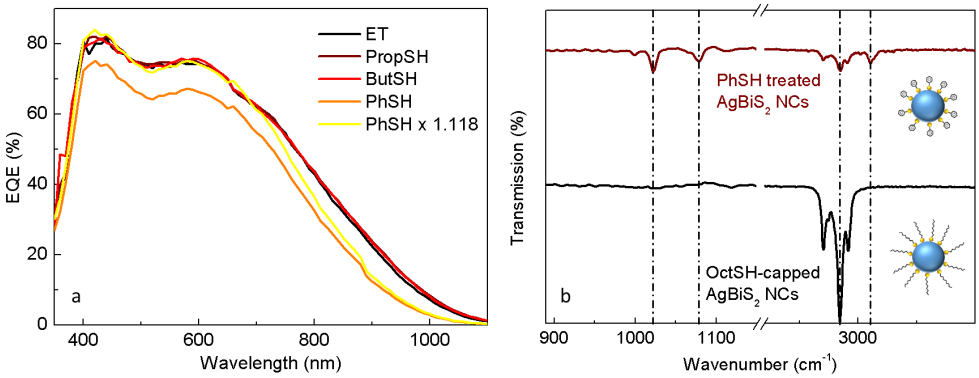

Figure 3.4: Effect of different thiols on the performance of $AgBiS_2$ CNC solar Cells. (a) EQE spectra of devices prepared with different thiols, (b) FTIR spectra showing the exchange of 1-octanethiol (OctSH) with thiophenol (PhSH) (Curves were plotted with offset for ease of viewing.).

A close examination of the film formation via FTIR spectroscopy revealed that thiophenol treatment caused a significant reduction of the C-H peaks in the range 2750-3000 cm^{-1} and introduced new peaks into the spectrum (Figure 3.4b). The presence of the peak at 3050cm^{-1} after thiophenol treatment, which corresponds to the vibrational frequencies of the benzene ring, [141] demonstrated that it was possible to replace most of the bound 1-octanethiol with thiophenol under ambient conditions (Figure 3.4b).

Thus, it can be concluded that the attachment of thiophenol onto the surface of $AgBiS_2$ CNCs can effectively increase V_{OC} of the solar cells, yet this increase in V_{OC} is accompanied by a significant decrease in J_{SC}, causing an overall drop in PCE. Thus, it is evident from the results of this Section that ET is the best performing ligand

for high performance $AgBiS_2$ CNC solar cells although all of the ligands molecules, both alkyl thiols and aromatic thiol used in this ligand study, can yield acceptable performance in $AgBiS_2$ CNC solar cells.

3.3 Thiol−iodide mixed ligands for $AgBiS_2$ CNC solar cells

There are multiple studies in the literature showing that the use of a mixed ligand approach can enhance the device performance effectively. [140] In our case, it is already known that simple iodide ligands, such as TMAI, are not capable of replacing thiols alone (see Section 2.3), although they may behave as co-ligands to enhance the performance of the solar cells as it was demossntrated in previous studies that TMAI could perform as an effective ligand for oleate-capped $AgBiS_2$ CNCs. [110]

Table 3.3: Effect of different thiol iodide mixtures on the performance of $AgBiS_2$ CNC solar cells.

Ligand	Efficiency (%)	V_{OC} (V)	FF	J_{SC} (mA cm^{-2})	$J_{SC,EQE}$ (mA cm^{-2})
ET+TMAI	4.53	0.45	0.61	16.52	19.05
PropSH+TMAI	3.85	0.44	0.63	13.92	15.29
ButSH+TMAI	3.69	0.44	0.6	13.95	15.71
MPA+TMAI	0.003	0.04	0.26	0.29	–

To test this hypothesis, we utilized mixtures of TMAI with different thiols. As it can be seen from Table 3.3, the best efficiency was obtained using ET/TMAI mixture. However, the presence of iodide did not affect the trend in efficiency with respect to the length of the ligand in a noticeable manner. This time, we also included another thiol from a slightly different family, 3-mercaptopropionic acid (MPA), into the study to observe the effect of acidity of the ligand introduced by the carboxylic group present in this molecule on the device performance. For the concentration level used to prepare this ligand solution (0.2 % v/v in methanol), the effect of this ligand was very pronounced compared to the other ligands. Although 1-propanethiol, its thiol analogue without a carboxylate group, gave an efficiency of 3.85 %, MPA effectively quenched the photovoltaic response of the device, possibly introducing significant defect states on the surface of the nanocrystals and increasing recombination rate within the absorber layer due to the presence of a relatively strong acidic group. It was also observed that the films deposited using MPA contained significant amount of cracks, which may be another explanation why we could not achieve any appreciable efficiency under cur-

rent processing conditions. Thus, the results of this study suggests that the presence of iodides in the ligand solution does not affect the photovoltaic performance of the devices to a significant degree, but a relatively acidic ligand solution (MPA) is capable of quenching the photocurrent efficiently.

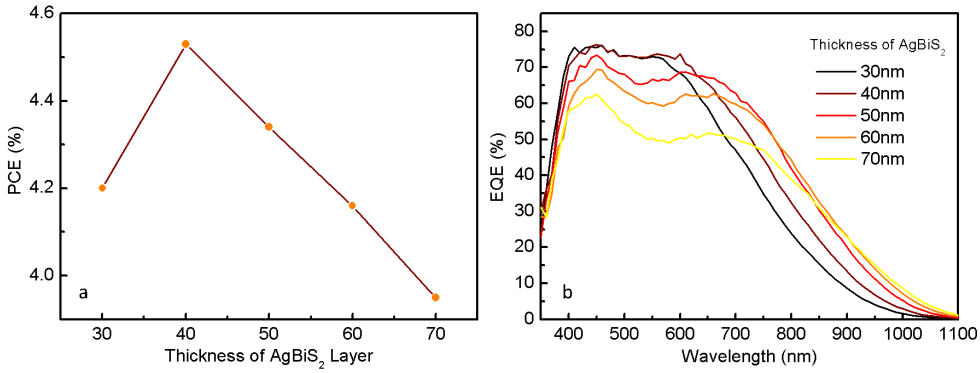

Figure 3.5: Fine-tuning of thickness of $AgBiS_2$ CNC solar cells treated with ET. (a) Change of device efficiency with respect to the thickness of $AgBiS_2$ CNC layer. (b) EQE spectra of the devices in (a).

3.4 Structural optimization of $AgBiS_2$ CNC solar cells

The optimization of the layer thickness plays an important role in thin film solar cells as the optical resonance modes due to the presence of multiple thin layers with different refractive indices in these devices can alter the effective absorption spectrum of the device. As the maximum J_{SC} obtainable from a solar cell is bound by the amount of light absorption of the solar cell, it has utmost importance to maximize the absorption by the device to cover the solar irradiance spectra extensively. Upto this point, we used a thickness of 35-40 nm for $AgBiS_2$ CNC layer, as it was pointed out that 37 nm was the optimal thickness for this device structure with $AgBiS_2$ CNC film in a previous study. [110] After determining the effect of different ligands on device characteristics, we directed our attention from ligand exchange study into the optimization of the thickness of the $AgBiS_2$ CNC layer to confirm the validity of this finding for our devices. In this part, we used a relatively less concentrated dispersion of $AgBiS_2$ CNCs (20 mg ml^{-1}) to deposit multiple layers of $AgBiS_2$ in a more controlled manner. The results of this study are provided in Figure 3.5. According to these results, the best efficiency was obtained when four layers of $AgBiS_2$ CNCs were used (the total thickness of the $AgBiS_2$ CNC layer was close to 40 nm). This showed that room temperature $AgBiS_2$

CNCs behaved in very similar way to Schlenk-line $AgBiS_2$ CNCs in terms of optical behavior. The red shifting of the peaks in EQE spectra with respect to the thickness of $AgBiS_2$ CNC layer confirmed the successful deposition of $AgBiS_2$ CNCs due to strong dependence of peak positions in EQE spectrum on layer thickness for thin-film solar cells as discussed previously.

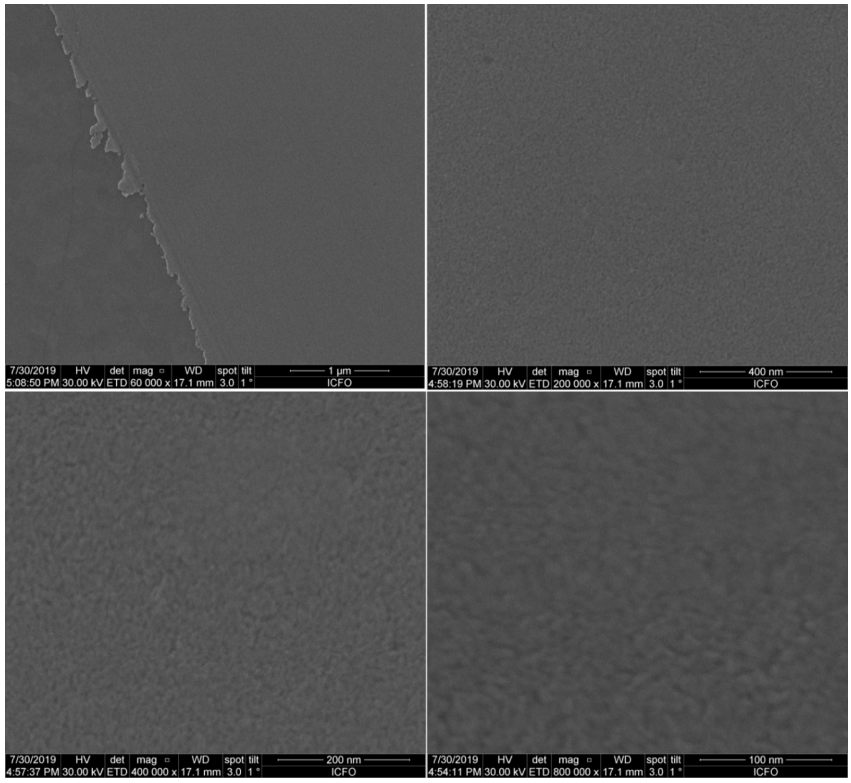

Figure 3.6: Surface morphology of $AgBiS_2$ thin layers deposited on top of ITO glass at different magnification showing the smoothness of the films.

3.5 Characterization of optimized $AgBiS_2$ CNC solar cells

Our previous findings showed that the best result was achieved with the use of the shortest alkyl thiol as the film deposition ligand, ethanethiol (ET), without any need for a co-ligand. Thus, this part is dedicated to the devices prepared by ET treatment only to be able to give the reader a more focused overview of the effects of this molecule on device characteristics. First, we prepared samples using ITO glass as the substrate to check the quality of the film and to verify the absence of any cracks or pinholes as the

defects in the CNC film are detrimental to the device performance. A Scanning Electron Microscope (SEM) examination revealed that ET-treatment could give smooth and dense $AgBiS_2$ CNC thin films (Figure 3.6).

As the next characterization step, a FTIR study was carried out to demonstrate the effective removal of 1-octanethiol from $AgBiS_2$ CNC film after ligand treatment. To ensure that the spectrum does not have any contribution from the unbound 1-octanethiol molecules, the film was rinsed with methanol before treating with ET. No significant change was observed in the C-H peaks (within 2850-3000 cm^{-1} range) after methanol rinsing. After treatment with ET and annealing, the intensity of the C-H peaks decreased significantly, showing removal of most of the 1-octanethiol from the surface of the nanocrystals (Figure 3.7a).

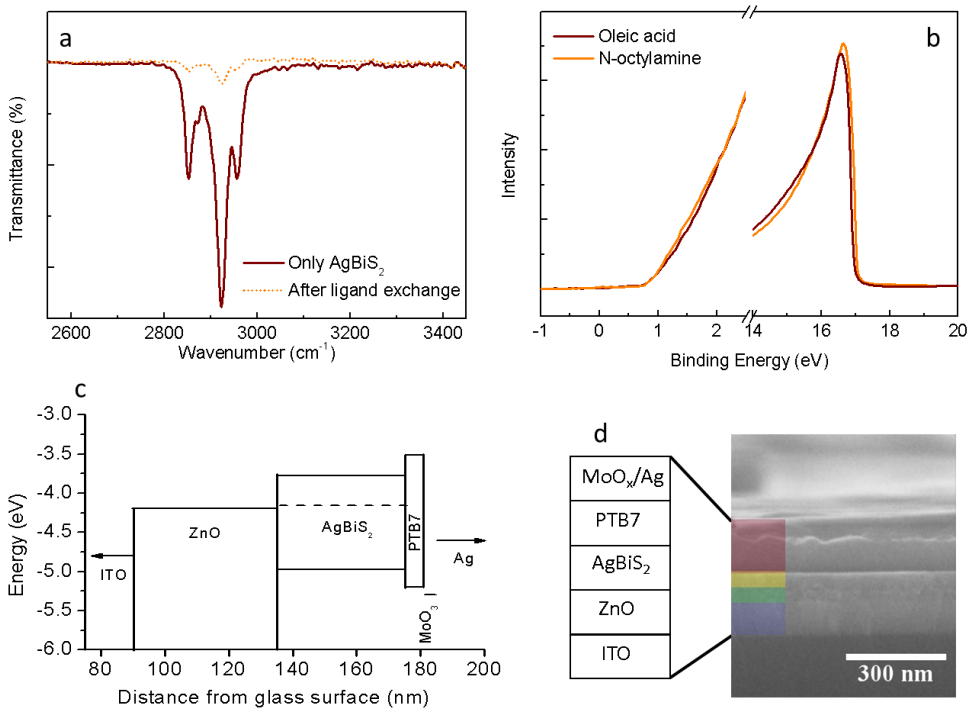

Figure 3.7: Characterization of $AgBiS_2$ CNC layer treated with ET. (a) FTIR results showing the removal of most of the organics from the film (Orange line: before ET and brown dotted line: after ET treatment). (b) UPS scans of room temperature (Orange: n-octylamine, treated with ET) and Schlenk-line (Brown: oleic acid, treated with TMAI) $AgBiS_2$ nanocrystals (under excitation by HeI 21.2 eV photons). (c) Band positions of room-temperature $AgBiS_2$ nanocrystals within the solar cell. (d) Cross sectional SEM image of the solar cell showing individual layers.

In the second part, we focused our attention onto the device fabrication. To test the photovoltaic performance of the nanocrystals, a suitable device structure has to be chosen according to the energy levels of $AgBiS_2$ CNC layer. For this purpose, we utilized UPS technique as it can give reliable results for the energy levels of the semiconductors. For UPS measurement, the samples of Schlenk-line $AgBiS_2$ CNCs and of room-temperature $AgBiS_2$ CNCs were prepared using the solid-state ligand exchange. Yet, we utilized different ligands for these two types of CNCs. We used TMAI treatment to prepare the Schlenk-line $AgBiS_2$ CNCs as an optimized ligand exchange method for Schenk-line $AgBiS_2$ CNCs was already reported in the literature. [110] For room temperature $AgBiS_2$ CNCs, we utilized ET as the ligand due to the results provided by our previous ligand exchange studies. UPS findings indicated that the energy levels of these two types of nanocrystals coincided although different synthesis methods and different ligands were used to prepare the films (Figure 3.7b). As the energy levels of the nanocrystals were found to be close, we employed the previously reported structure as the platform to study the optoelectronic properties of room-temperature $AgBiS_2$ CNCs (Figure 3.7c). [110] A cross sectional SEM image of the fabricated structure is provided in Figure 3.7d. In this structure, a hole blocking 45-nm thick ZnO layer was deposited by sol-gel method (see Appendix B for futher details on device fabrication). On top of this layer, $AgBiS_2$ CNC layer was deposited using ET treatment. After spin coating a very thin layer of electron blocking polymer, PTB7, the device was completed with the thermal evaporation of a very thin (3 nm) layer of MoO_3 and a top contact of 150 nm-thick Ag metal through a metal mask to define the active areas.

The possibility of using ethanethiol for the ligand exchange process allowed us to use a faster single-step deposition process, by using more concentrated CNC dispersion (60 g L^{-1}) to achieve the optimal $AgBiS_2$ thickness of $\sim$ 40 nm, as opposed to previously reported layer-by-layer deposition process for Schlenl-line $AgBiS_2$. [110] With this ligand exchange, our champion $AgBiS_2$ CNC solar cell gave a PCE of 4.62 % just after device fabrication. After storing the solar cell under ambient conditions (24 °C, 50-60 % humidity) for 1 day, the efficiency of the solar cell showed $\sim$ 20 % increase, reaching 5.55 % without a significant hysteresis (Figure 3.8a-b). With a thickness of only $\sim$ 40 nm, a promising V_{OC} of 0.43 V and a J_{SC} of 22.07 mA cm^{-2} with a FF of 0.59 were attained demonstrating the success of our room-temperature technique. In addition, J_{SC} obtained from EQE spectrum was calculated to be 21.13 mA cm^{-2}, which was close to the measured short-circuit current of 22.07 mA cm^{-2} (Figure 3.8c).

We also fabricated solar cells without ET treatment to show the effect of ET treatment on the optimized device structure. The solar cell without ET treatment was

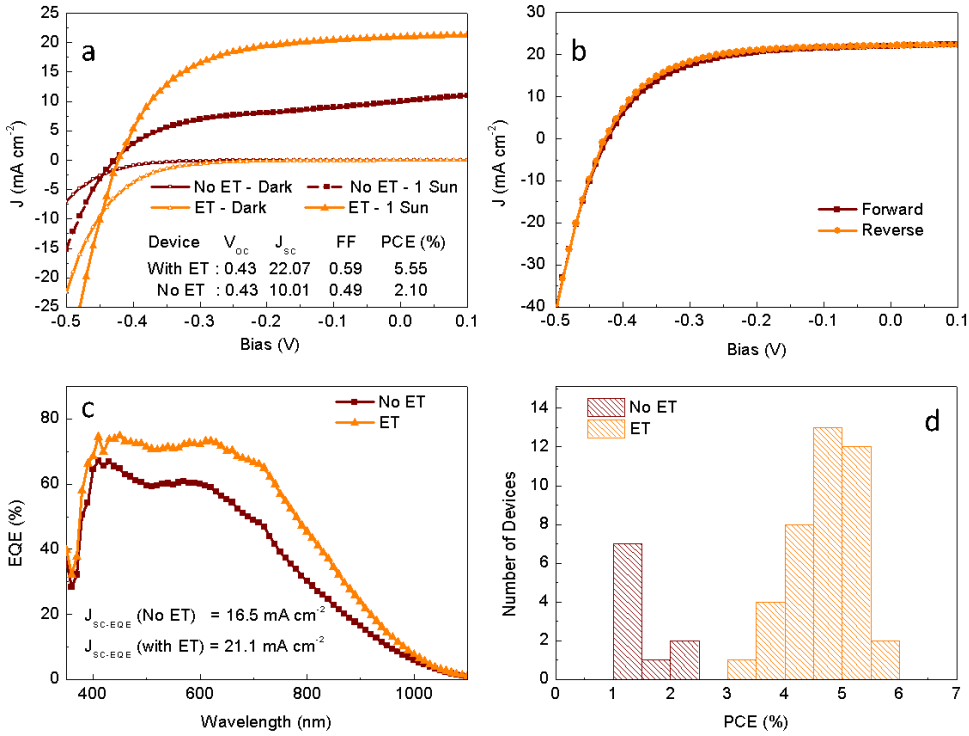

Figure 3.8: Characterization of $AgBiS_2$ CNC solar cell. (a) J-V curves, (c) EQE spectra and (d) device performance statistics of the room-temperature $AgBiS_2$ CNC solar cells with ET (Orange triangles) and without ET (Brown squares) treatment 1 day after device fabrication. (b) J-V scans of $AgBiS_2$ CNC solar cell treated with ET showing the negligible hysteresis of the device.

prepared by spin coating nanocrystal dispersion and rinsing with pure methanol using the same process parameters used to prepare the ET-treated solar cell. As it is seen in Figure 3.8a, the solar cell without ET treatment performed much worse than the one prepared with ET treatment. Although both devices gave very similar V_{OC}, the solar cell without ET treatment yielded a J_{SC} that was less than half that of the device with ET treatment. Furthermore, we found that FF of the solar cell without ET treatment was noticeably lower than that of the solar cell with ET treatment, demonstrating that the extraction efficiency of the charge carriers within the $AgBiS_2$ CNC layer is lower if ET treatment is not performed. This is an expected result as the presence of long alkyl group of 1-octanethiol in the CNC film can effectively hinder charge transfer within $AgBiS_2$ layer, causing a drop in J_{SC} and FF. Moreover, J_{SC} calculated from EQE curve for the solar cell without ET treatment was found to be much higher than the measured J_{SC} (16.5 vs. 10.01 mA cm^{-2}), which hints that increasing recombination rate upon higher photocarrier density may be a contributing factor to low PCE (Figure

3.8c). Overall, the devices produced with ET treatment yielded an average PCE of 4.68 ± 0.55 % while PCE of the devices without ET treatment was found to be 1.51 ± 0.40 % (Figure 3.8d), which verified the necessity of ET treatment in fabrication of $AgBiS_2$ CNC solar cells.

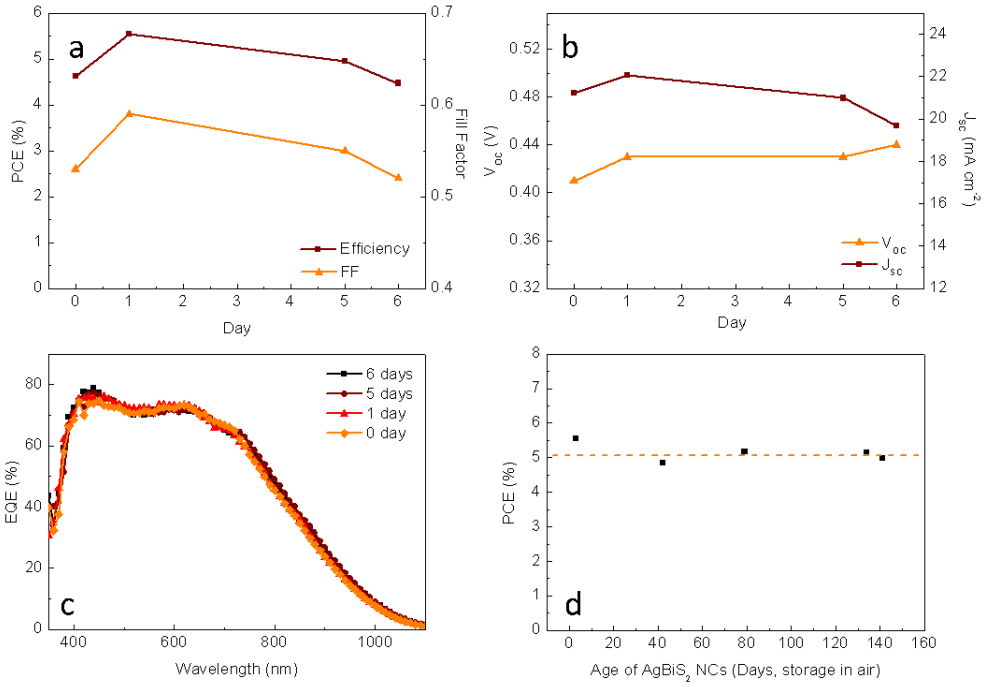

Figure 3.9: Solar cell parameters with respect to storage time in air. Change of (a) PCE (Brown squares) - FF (Orange triangles), (b) V_{OC} (Brown squares) - J_{SC} (Orange triangles), and (c) EQE of the solar cell (Orange diamonds: just after device fabrication, red triangles: after 1 day, brown circles: after 5 days and black squares: after 6 days) after being stored in air. The solar cells preserve ∼ 80 % of their maximum PCE after 6 days of storage under ambient conditions (24 C, 50-60 % humidity). (d) The solar cell efficiency with respect to the age of $AgBiS_2$ CNC dispersion.

After storage in air under ambient conditions for 6 days, the solar cell preserved ∼ 80 % of its maximum PCE (Figure 3.9a-b). It was observed that the change in device efficiency closely followed the change in fill factor of the device. Although V_{OC} increased steadily within this period of 6 days, J_{SC} showed a slightly different behavior. J_{SC} of the device just after fabrication was measured to be 21.2 mA cm^{-2} whereas this value increased to 22.07 mA cm^{-2} after one day of storage in air. However, J_{SC} showed a noticeable drop first to 21.00 and then to 19.67 mA cm^{-2} after 5 and 6 days of storage in air, respectively. Yet, this change in efficiency with respect to storage time

in air was not reflected in EQE spectra. All the measured EQE spectra during the course of this experiment yielded very similar results without any noticeable change in either amplitude or shape of the EQE curves (Figure 3.9c), which may indicate that exposure to air causes an increase in non-radiative recombination rate in these devices, reducing device performance under high light bias. It was also observed that $AgBiS_2$ nanocrystal dispersions in octane exhibited good stability characteristics under long-term storage in air (Figure 3.9d). Even after 140 days of storage in air, the nanocrystals preserved their colloidal stability and the solar cells made of these nanocrystals with ET treatment yielded a PCE of ~ 5 %.

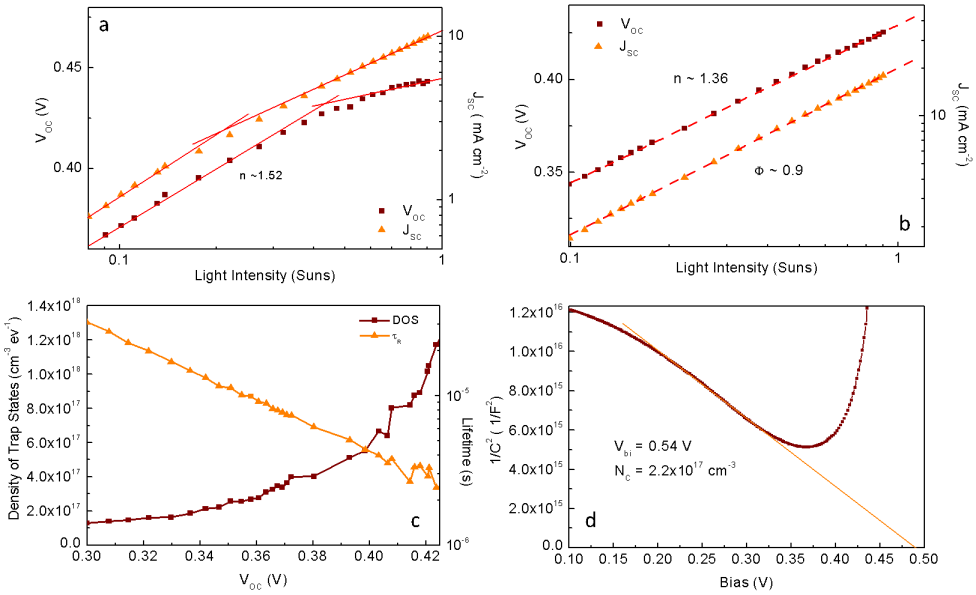

Figure 3.10: Electrical characteristics of the room-temperature $AgBiS_2$ nanocrystals treated with and without ET. Light intensity-dependent V_{OC} (Brown squares) and J_{SC} (Orange triangles) of the $AgBiS_2$ nanocrystal solar cell (a) without and (b) with ET treatment showing saturation at high light intensity for the device prepared without ET treatment. (c) Density of trap states (Brown squares) within the bandgap and carrier lifetime (Orange triangles) with respect to V_{OC} and (d) Mott-Schottky plot of the solar cell showing the effective carrier density (N_C) and built-in potential (V_{bi}) for the device prepared with ET treatment.

To probe the effect of the intensity of light on device performance, we carried out light intensity-dependent V_{OC}/J_{SC} measurements. For the solar cell prepared without ET treatment, the light intensity-dependent V_{OC}/J_{SC} measurements showed saturation at high light bias condition, explaining the origin of lower J_{SC} for this

device at 1 Sun (Figure 3.10a). Also, the ideality factor of this device was found to be 1.52 at low light bias regime, which is an indication for the trap-mediated Shockley-Read-Hall (SRH) recombination. [142] In addition to high ideality factor, the presence of V_{OC} saturation at high light bias level gave hints about high surface recombination at the semiconductor-electrode interface as explained elsewhere. [29] On the other hand, the light intensity-dependent V_{OC} measurement for ET-treated solar cell showed no saturation and yielded an ideality factor of 1.36, showing that ET-treatment was effective at reducing SRH recombination (Figure 3.10b). Considering that the performance of the device was improved significantly by ET-treatment only, it can be asserted that some of the traps involved in carrier loss are surface-related defects that can be passivated by ET-treatment. In addition, light intensity-dependent J_{SC} for ET-treated device gave a power factor of 0.9, showing that the charge carrier extraction in the structure is efficient enough for the proper operation of the solar cell. [143] The light intensity dependence of carrier lifetime showed a single-component decay with an inverse slope of -0.115 V/decade, reaching $\sim$ 2.2 μs at 1 Sun light bias. The density of trap states (DOTS) within bandgap was measured following a method published in the literature. [43] The measured DOTS in the bandgap of $AgBiS_2$ was found to be an order of magnitude higher compared to PbS nanocrystal solar cells, giving hints about the possible causes of the drop in J_{SC} with increasing thickness of the nanocrystal layer (Figure 3.10c). [43, 110] The effective carrier density and the built-in potential were measured to be 2.2×10^{17} cm^{-3} and 0.54 V using Mott-Schottky plot (Figure 3.10d). Using these values, the depletion width in the device was calculated to be $\sim$ 70 nm at zero bias. Hence, these solar cells operate with a depleted $AgBiS_2$ layer, which is in accordance with the apparent match of the measured J_{SC} and J_{SC} predicted by optical (transfer matrix method) simulations (Figure 3.11). Although 40 nm layer of $AgBiS_2$ CNCs is sufficient to achieve a J_{SC} of 22 mA cm^{-2} and a PCE in excess of 5 % with the current structure, this depletion width is not sufficient to reach a J_{SC} more than 25 mA cm^{-2}, which is predicted to be obtainable with an $AgBiS_2$ thickness of more than 150 nm. Thus, there is still some room to improve the PCE of $AgBiS_2$ CNC solar cells by engineering the charge transport in the device.

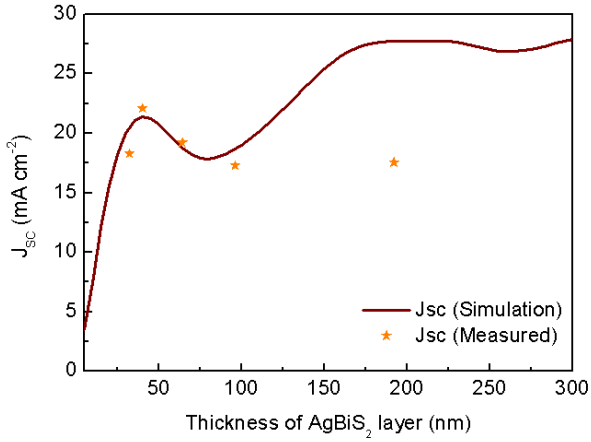

Figure 3.11: Simulated and best measured J_{SC} as a function of $AgBiS_2$ thickness. The difference between the simulated and measured J_{SC} increases for an $AgBiS_2$ thickness of more than 100 nm in accord with the depletion width determined via capacitance-voltage measurement.

Table 3.4: Price of the chemicals for the synthesis cost calculation.

Chemical	Purity	Price [€]	Amount	Cost per unit
HMS	Synthesis grade	465.5	25 gr	3322 €/mol
Ag(OAc)	99.99 %	523	50 gr	1747 €/mol
$Bi(OAc)_3$	99.999 %	340	50 gr	2625 €/mol
Oleic acid	90 %	51	1000 ml	0.051 €/ml
Octadecene	90 %	44.6	1000 ml	0.0446 €/ml
Sulfur	99.998 %	433	250 gr	55.54 €/mol
AgI	99.9 %	207	50 gr	972 €/mol
BiI_3	99 %	325	100 gr	1917 €/mol
N-octylamine	99 %	71.6	500 gr	0.112 €/ml

3.6 A simple cost calculation for $AgBiS_2$ CNCs

Besides ease and simplicity, the synthesis cost of $AgBiS_2$ nanocrystals is also reduced by using our technique. Due to the substitution of expensive and air-sensitive HMS with cheap and abundant elemental sulfur, a cost saving of $\sim$ 98 % is achieved (HMS - synthesis grade: 3322 € mol^{-1}, sulfur - 99.99 %: 55.4 € mol^{-1}, see Table 3.4 for details) for the anion precursor. Our preliminary estimations showed that a 40 nm thick $AgBiS_2$ nanocrystal film costs 11.6 € m^{-2} if hot-injection method is utilized whereas the costs will be reduced to 4.5 € m^{-2} with room-temperature route, showing that an overall cost saving of $\sim$ 60 % can be easily achieved by substituting HMS with

elemental sulfur, metal acetates with metal iodides and oleic acid/octadecene with n-octylamine. Furthermore, it is expected that cost savings be even higher when the cost related to the vacuum, heating and inert reaction environment is also taken into consideration.

As a summary, we have demonstrated a solution-processed solar cell comprising environmentally friendly $AgBiS_2$ CNCs that are synthesized at room-temperature and ambient conditions. We report a new ligand exchange strategy and single-step film deposition method for our $AgBiS_2$ CNCs synthesized at room temperature to remove the long ligands to form a close-packed photovoltaic quality absorber layer. The fabricated devices showed a promising power conversion efficiency in excess of 5 % and confirmed that the synthesis-related cost can be reduced significantly using air-stable chemicals for the synthesis of nanocrystals. Our work paves the way towards solar cell absorbers that are at the same time cheap to produce and environmentally friendly from both a material and production perspectives and address the regulatory concerns and synthetic cost of colloidal nanocrystals based on Schlenk line approaches.

4

An Ambient Condition Synthesis Method for $AgBiSe_2$ CNCs

Having a narrow bandgap suitable for photovoltaics (0.6 eV in bulk [144] and 0.7 - 1.0 eV in nanocrystalline form [145, 146]), silver bismuth selenide ($AgBiSe_2$) is another useful member of the silver bismuth chalcogenide family. Although Ag_2Se and Bi_2Se_3 have been studied extensively in the literature thanks to their attractive optical and thermoelectric properties, the number of reports dealing with this ternary semiconductor is limited. [147–153] This material has recently attracted attention for its potential applications, especially in thermoelectrics. [144, 154, 155] Although various studies have been published, these studies mainly focused on either bulk or in thin films of $AgBiSe_2$. [156–159] Yet, only a few reports have been presented in the literature on the synthesis of colloidal $AgBiSe_2$ nanocrystals. [146, 160] To our knowledge, all of these studies were performed under a controlled environment to protect the precursors from oxidation. This results from the use of either elemental selenium that necessitates high reaction temperature or more reactive precursors, such as $Bi[(N(SiMe_3)_2]_3$ that are also prone to oxidation under ambient conditions. [146, 160] Thus, addressing the oxidation problem of precursors while keeping the reaction temperature as close to

room temperature as possible for a low-cost ambient condition synthesis of $AgBiSe_2$ CNCs still remains as a challenge.

One of the major issues with the synthesis of metal selenide nanocrystals is the availability of an air-stable, cost-effective and sufficiently reactive selenium precursor to replace the combination of elemental selenium-high reaction temperature utilized in the existing reports. Although some alternative selenium precursors have been proposed, such as NaHSe, $(Me_3Si)_2Se$, trioctylphosphine-Se (TOP-Se) and tributylphoshine-Se (TBP-Se), [161–166] they do not offer any viable solution due to their high air-sensitivity and high cost associated with the use of phosphines. Apart from complexes of elemental Se with TOP and TBP, other strategies have been proposed to prepare a viable selenium precursor using elemental selenium. Among those, alky ammonium (poly)selenides were found to be promising thanks to their relatively low cost and high solubility in alkyl amines. One of the early reports on this route used a strong reducing agent, sodium borohydrate ($NaBH_4$), for the reduction of elemental selenium into selenide ions to form the alkyl ammonium (poly)selenides. [167] While colloidal nanocrystals were successfully produced using this Se precursor, the necessity of air-free synthesis techniques remained in place as a result of the air sensitivity of $NaBH_4$ and of the obtained selenium precursor. Furthermore, the possibility of Na-doping of the nanocrystals remained as an open question to be answered due to the byproducts of reaction remaining in the synthesis mixture after the formation of alkyl ammonium (poly)selenides. However, as a result of the ease and effectiveness of amine-assisted Se dissolution in organic solvents, the mixtures of amines with thiols have attracted significant attention thanks to their capacity of forming relatively concentrated solutions of selenium and the absence of foreign cations due to the use of inorganic reducing agents. This strategy has been utilized in different studies published in the literature in various forms. However, the exact mechanism of dissolution and nanocrystal formation via the use of this solvent mixture had remained unclear.

Recently, it was demonstrated that the dissolution of elemental selenium in a mixture of oleylamine and alkyl thiols could occur readily without heating. [168] In the given reaction, it was reported that the alkyl thiols could effectively reduce elemental selenium to selenide anions in the presence of oleylamine and that the oleylamine molecules could bind to selenide ions to form alkyl ammonium (poly)selenide compounds. One of the key findings of this study was that alkyl ammonium (poly)selenides could stay intact under ambient conditions for sufficiently long times if excess thiol was provided into the solution. [168]

In the first part of this Chapter, we extend the results on this selenium precursor and show that the mixed amine-thiol solvent is capable of reducing not only elemental

selenium as shown by a previous report, [168] but also SeO_2 (Se^{4+}) into selenide ions. We also demonstrate that the obtained selenium precursor is sufficiently reactive towards silver and bismuth iodide salts at room temperature to form $AgBiSe_2$ CNCs without requiring a chemically inert reaction environment or heating, unlike the results reported previously. This, in turn, enables the utilization of a much-simplified synthesis setup compared to the hot-injection methods that utilize Schlenk line setup. Thanks to the strong antioxidant property of thiol-amine mixture on this selenide precursor, it is demonstrated that various binary and ternary metal selenides can be obtained within minutes. We make use of binary phases, Ag_2Se and Bi_2Se_3, as references to demonstrate the successful formation of ternary $AgBiSe_2$ phase in the presence of both Ag and Bi halides. The results of the characterization via TEM, XRD, XPS and absorption spectroscopy are provided to show the properties of the resulting colloidal dispersions. In addition, a prototype solar cell made of $AgBiSe_2$ CNCs is presented to highlight the quality of the obtained product. To our knowledge, this solar cell is the first $AgBiSe_2$ CNC solar cell ever to be reported in the literature. In the second part of this Chapter, we present our findings on the possibility of synthesizing alloyed quaternary silver bismuth sulfide-selenide (AgBiSSe) CNCs with varying sulfur/selenium ratio. For this purpose, we combine the synthesis methods of $AgBiS_2$ and $AgBiSe_2$ CNCs developed in this thesis work to produce quaternary AgBiSSe CNCs under ambient conditions. The formation of quaternary CNCs is verified via absorption spectroscopy, XRD and XPS measurements.

4.1 A synthesis route for metal selenides under ambient conditions

In the previous studies, oleylamine was used extensively as the primary alky amine to dissolve elemental selenium via formation of oleylammonium (poly)selenides. However, it is known that the reactivity of a precursor generally decreases if longer groups are attached to the chemically active site due to the steric hindrance effects. For this reason, generally a hot-injection method is utilized to obtain nanocrystals of sufficient size by increasing the reaction rate if bulky precursors are utilized. [145,146,168] In accordance with this general rule, we found advantageous to utilize n-octylamine as a shorter length alkyl amine instead of oleylamine to form the alkyl ammonium poly selenide precursor. In this synthesis route, n-octylamine acts both as the reaction medium for the solvation of the precursors and as a stabilizing agent for $AgBiSe_2$ nanocrystals, similar to the method utilized for $AgBiS_2$ CNCs. [169]

There exist various selenium compounds in the market to be utilized as the selenium precursor. However, it is advantageous to employ a reaction path that can utilize an air-stable Se source as the starting material to eliminate the need for protection of the Se source from degradation. Selenium dioxide (SeO_2) was chosen as the selenium source in our reaction for elemental selenium and selenides are typically prone to oxidation in air forming SeO_2 as the main product of the oxidation. Our experimental findings demonstrated that selenium dioxide could be reduced successfully using a mixture of 1-octanethiol (RSH) and 1-octylamine (RNH_2) at room temperature following the overall reaction given in Eq. 4.1 (See Figure C.1 of Appendix C).

$$2RNH_2 + SeO_2 + 6RSH \longrightarrow (RNH_3)_2Se + 3RS - SR + 2H_2O \tag{4.1}$$

In this reaction, every two molecules of alkyl thiols oxidize and combine to form a dialkyl dithiol molecule in the presence of alkyl amines and SeO_2, yielding an electron pair in the process to reduce Se^{4+} (assuming complete reduction of Se^{4+} to Se^{2-}). After the reduction of Se^{4+}, the obtained selenide ions are dissolved by complexing with alkyl amine molecules forming the main selenium precursor of the reaction. This reaction occurs in a similar fashion given in previous reports, [168] although they used elemental selenium rather than SeO_2 as the selenium source and they utilized different alkyl amines and alkyl thiols for the reduction. After the formation of the Se precursor, the presence of AgI and BiI_3 in the reaction mixture triggers the formation of $AgBiSe_2$ nanocrystals in a simplified reaction route given in Eq. 4.2.

$$AgI + BiI_3 + 2(RNH_3)_2Se \longrightarrow AgBiSe_2 + 4RNH_3I \tag{4.2}$$

In the reactions above, Pearsons hard and soft acids and bases rule (HSAB) dictates that the reaction will be driven to form alkyl ammonium iodide salt as iodide is a harder base and alkyl ammonium is the harder acid in the given reaction. [170] For this reason, it should be noted here that it is possible to synthesize $AgBiSe_2$ nanocrystals using different Ag and Bi halides. However, we utilize metal iodides as the primary cation precursors for the synthesis thanks to their low hygroscopic nature and adequate air-stability.

Although this selenium precursor is sufficiently stable in air in the presence of excess amine-thiol solvent to enable the rapid synthesis of metal chalcogenide CNCs, it

should be noted that this precursor cannot be stored in air indefinitely due to constant loss of amine-thiol solvent through oxidation-reduction cycle of Se in air. [168] The in-situ formed alkyl ammonium (poly)selenide precursor decomposes in air slowly to form elemental Se precipitate (trigonal phase: JCPDS 06-0362) rather than reverting back to white-colored selenium dioxide if no metal cation that can react with the selenium precursor is present in the solution (Figure 4.1). No foreign peaks, which may result from SeO_2, was detected in XRD scans, showing that this solvent mixture was effective enough for the complete reduction of SeO_2 and that it was a strong antioxidant for Se at different oxidation states.

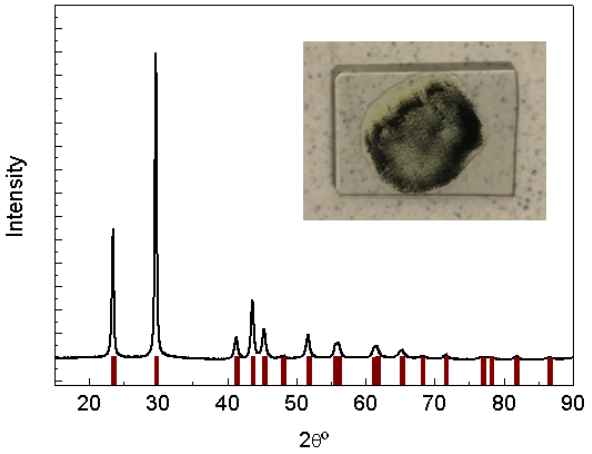

Figure 4.1: XRD scan of the precipitate obtained from Se precursor after cleaning (The brown bars indicate the peak positions of trigonal selenium JCPDS 06-0362. Inset: a picture of the selenium precursor prepared with SeO_2 and n-octylamine/1-octanethiol mixed solvent that is left in air for decomposition.).

4.2 The synthesis and characterization of ternary $AgBiSe_2$ CNCs

As the first step in this part of the study, we synthesized ternary $AgBiSe_2$ CNCs using our ambient synthesis technique (See Appendix C for experimental details). After the synthesis, the resulting CNCs were cleaned via addition of an antisolvent and centrifugation, which is a similar to the purification process used for the cleaning of $AgBiS_2$ CNCs. TEM micrographs showed that $AgBiSe_2$ CNCs had spherical shapes with an average size of 6 nm (Figure 4.2a-c). The crystallinity of the nanocrystals were visible in high-resolution TEM micrographs as given in Figure 4.2b. The selected area electron diffraction (SAED) verified the presence of a crystalline phase, showing that

the formed nanoparticles were not amorphous, but indeed nanocrystalline $AgBiSe_2$ (Figure 4.2d).

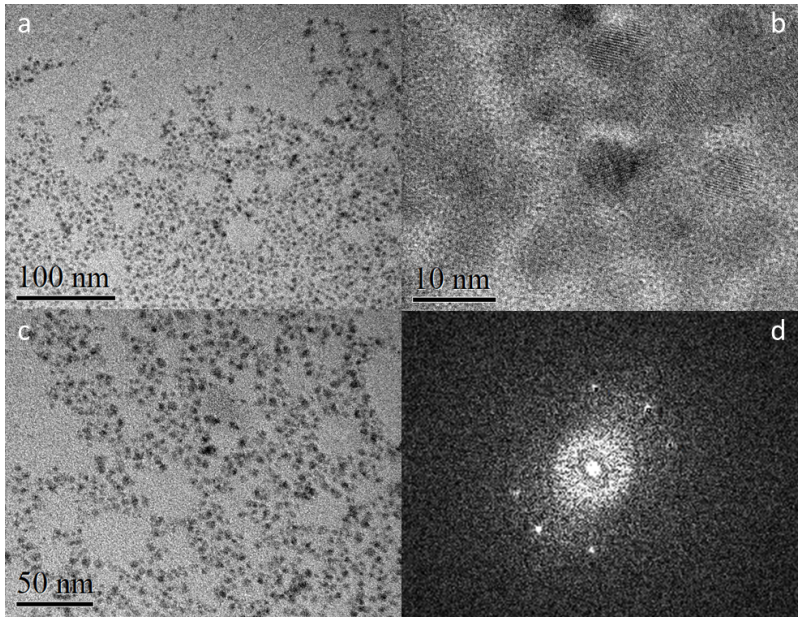

Figure 4.2: TEM and SAED of $AgBiSe_2$ CNCs. (a - c) TEM images of $AgBiSe_2$ CNCs under different magnifications. (d) SAED of $AgBiSe_2$ CNCs showing the nanocrystalline structure of the product.

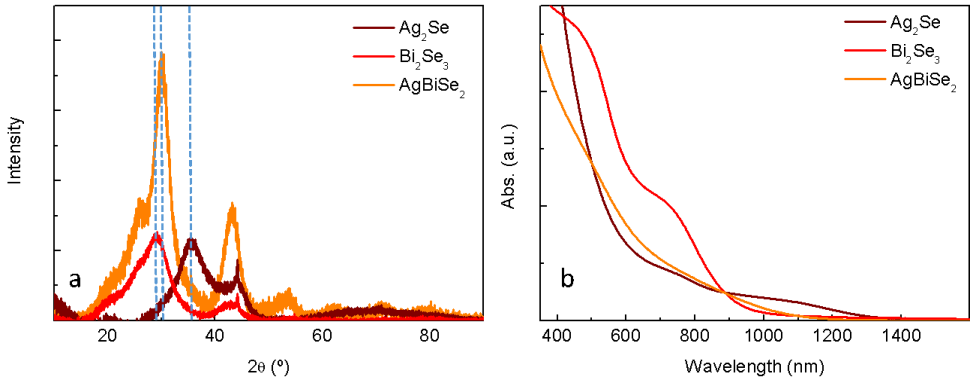

Figure 4.3: Structural and optical characterization of $AgBiSe_2$ CNCs. (a) XRD scans and (b) absorption spectra of the ternary and binary phases (The positions of the main peaks of $AgBiSe_2$, Bi_2Se_3 and Ag_2Se are marked with blue dashed lines.).

As a complementary method, XRD was utilized both to confirm the formation

and to demonstrate the phase purity of $AgBiSe_2$ nanocrystals. For this purpose, we also synthesized silver selenide (Ag_2Se) and bismuth selenide (Bi_2Se_3) CNCs to verify the absence of these binary phases in the final $AgBiSe_2$ CNC dispersion. Our results indicated that in the presence of both silver and bismuth precursors, only the ternary phase was obtained with a quantity detectable by XRD (Figure 4.3a). This finding was also supported by absorption spectroscopy as given in Figure 4.3b. The absorption spectra of both of the binary phases showed distinct features. For Bi_2Se_3 CNCs, an excitonic-like peak was detected around 720 nm. Ag_2Se CNCs showed two broad peaks located close to 730 and 1060 nm. On the other hand, $AgBiSe_2$ CNCs did not exhibit any peak-like feature in the absorption measurements, which is very similar to the absorption spectrum of $AgBiS_2$ CNCs in shape, as already described in Chapter 2.

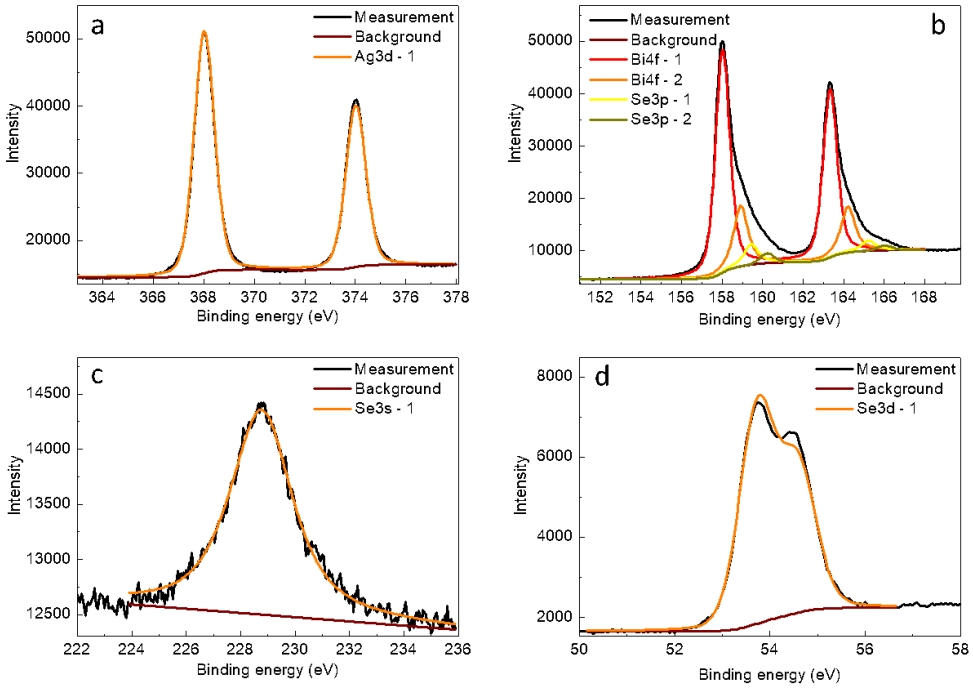

Figure 4.4: XPS spectra of $AgBiSe_2$ CNCs. (a) Ag-3d, (b) Bi-4f, (c) S-2s/Se-3s and (d) Se-3d regions.

The elemental composition of the resulting CNC dispersions were quantified via XPS. XPS analysis of the $AgBiSe_2$ CNCs revealed that the sample contains all three constituent elements (Ag, Bi and Se, see Figure 4.4).A single Ag-3d doublet was located at $\sim$ 368 eV, in line with both those of $AgBiS_2$ CNCs reported in previous chapter and

the literature reports. [160] Two Bi-4f doublets were sufficient to fit Bi-4f spectrum (at $\sim$ 158.0 and $\sim$ 159.0 eV, respectively). Se-3s signal was detected at 228.9 eV in the S-2s/Se-3s spectral region (Figure 4.4c).The position of the Se-3d 5/2 peak (54.6 eV) confirmed that selenium was in 2- state and not oxidized under the conditions that the synthesis and purification steps were carried out as higher oxidation states would result in higher binding energies for Se (Figure 4.4d). [160,171] The evaluation of the XPS data showed that the elemental composition of $AgBiSe_2$ CNCs was 1.00:1.02:1.05 (Table 4.1).

Table 4.1: Elemental analysis of $AgBiSe_2$ CNCs synthesized via metal iodide salts and SeO_2 (Normalized to Ag-3d).

Ag	Bi	Se
1.00	1.02	1.05

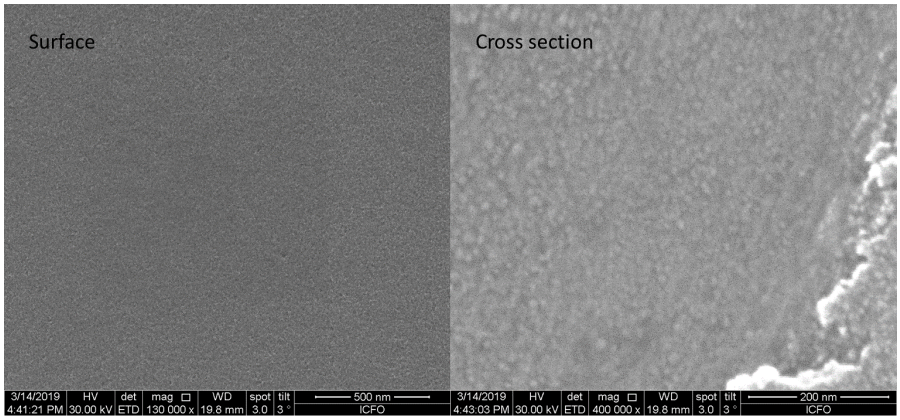

Figure 4.5: SEM of $AgBiSe_2$ NCs. (a) Top view and (b) cross sectional image taken from a scratch in the film.

A SEM investigation of the deposited films demonstrated that the films were smooth and crack-free (Figure 4.5). This is an important factor to be considered in nanocrystal device fabrication as any cracks and pinholes can severely affect the performance of the resulting devices. The cross sectional SEM images also revealed the nanocrystalline nature of the films.

UPS measurements were performed to determine the energy levels of $AgBiSe_2$ CNCs. It was found that the valence band and Fermi level of these CNCs were located around -4.92 and -4.16 eV, respectively (Figure 4.6a). According to these energy level values, P3HT was chosen as the electron blocking layer for the use of an electron blocking

layer with a similar valence band energy can provide an efficient hole transport channel between $AgBiSe_2$ CNC layer and the anode of the solar cell, possibly yielding higher PCE for $AgBiSe_2$ CNC solar cells.

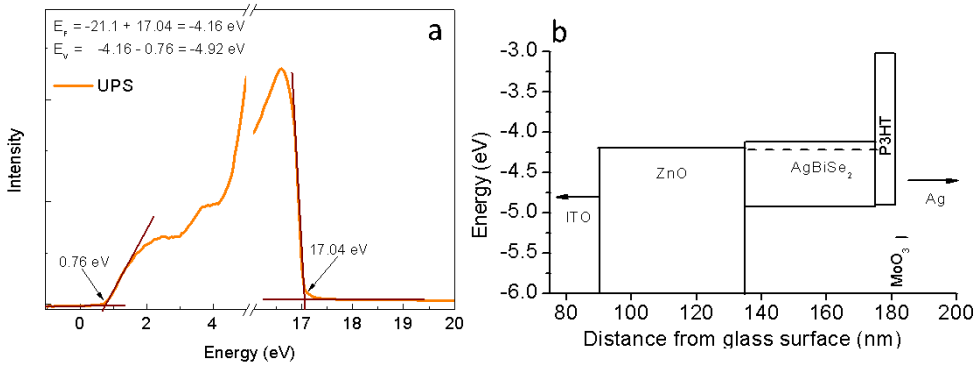

Figure 4.6: (a) UPS of $AgBiSe_2$ CNCs and (b) the energy level alignment in the proposed device structure.

We fabricated prototype solar cells of $AgBiSe_2$ CNCs with different thickness using the structure given in Figure 4.6b. The solar cells yielded a preliminary efficiency of 1.59 % just after the deposition of top contact for the device with 40 nm of $AgBiSe_2$ CNCs (Table 4.2). After 1 day of storage under ambient conditions, the efficiency increased to 2.6 %, which is the highest efficiency reported in the literature for any solar cell based on $AgBiSe_2$ CNCs to the best of our knowledge. This behavior, the increase of efficiency after exposure to air, is not rare and has been reported for different types of CNC solar cells, [73, 172] including $AgBiS_2$ CNC solar cells. [110, 169]

Table 4.2: Performance of solar cells of $AgBiSe_2$ CNCs just after metal deposition and after 1-day storage in air.

Time in Air (Days)	V_{OC} (V)	J_{SC} (mA cm^{-2})	FF	Efficiency (%)	Thickness of $AgBiSe_2$ (nm)
0	0.24	10.57	0.43	1.08	20
0	0.28	14.37	0.40	1.59	40
0	0.27	13.49	0.37	1.34	60
1	0.25	12.52	0.46	1.43	20
1	0.29	18.88	0.47	2.60	40
1	0.32	11.17	0.46	1.65	60

The solar cell with a 40 nm-thick $AgBiSe_2$ CNC layer exhibited a V_{OC} of 0.28 V,

a J_{SC} of 14.37 mA cm^{-2} and a FF of 0.40 just after fabrication. After 1 day of storage in air, J_{SC} showed a significant increase and reached to 18.88 mA cm^{-2}, while V_{OC} increased slightly to 0.29 V. As another observation, the J-V curve demonstrated a dramatic change because of FF increasing from 0.40 to 0.47 after 1-day storage in air (Figure 4.7a), pushing PCE to 2.6 %. Yet, this value of FF is still low in comparison to that of an optimized $AgBiS_2$ CNC cell and that there is still some room for further improvement.

The successful deposition of $AgBiSe_2$ CNC layers can be verified via EQE spectra of the devices. As the thickness of the $AgBiSe_2$ CNC layer increases, the optical resonance peaks in the EQE spectrum shifts toward longer wavelengths (Figure 4.7b). In addition to information about thickness of the films, EQE spectra also gave hints about the possible cause of the change in photovoltaic performance after storage in air. It was observed that the change in the EQE spectra was more pronounced in the shorter wavelength regime compared to the longer wavelengths. When the physical device structure is taken into consideration, it can be deduced that the transport of holes within the $AgBiSe_2$ CNC layer is not as efficient as that of electrons and this, in turn, results in carrier loss. Yet, this problem is partially levitated after storage in air, enabling holes created close to ZnO layer to be transported to P3HT layer with lower carrier loss, thus enhancing the overall device efficiency.

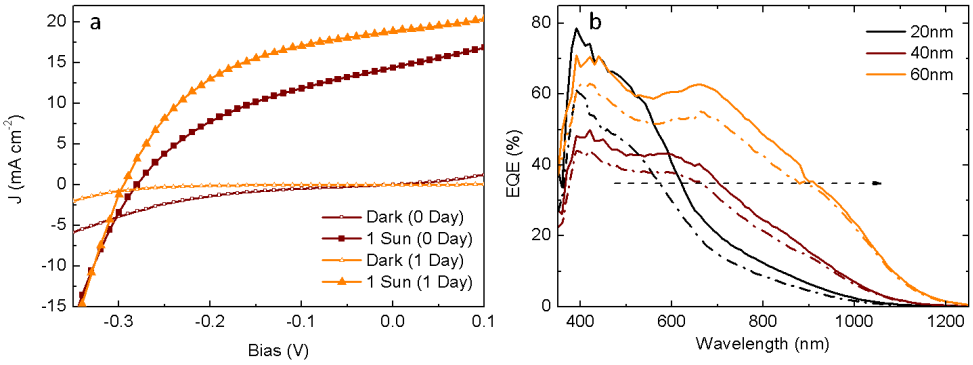

Figure 4.7: (a) J-V measurements of the solar cell with a 40 nm-thick $AgBiSe_2$ CNC layer just after metal deposition and after 1 day storage in air. (b) EQE of solar cells with different $AgBiSe_2$ CNC layer thickness just after metal deposition (dashed lines) and after 1-day storage in air (solid lines).

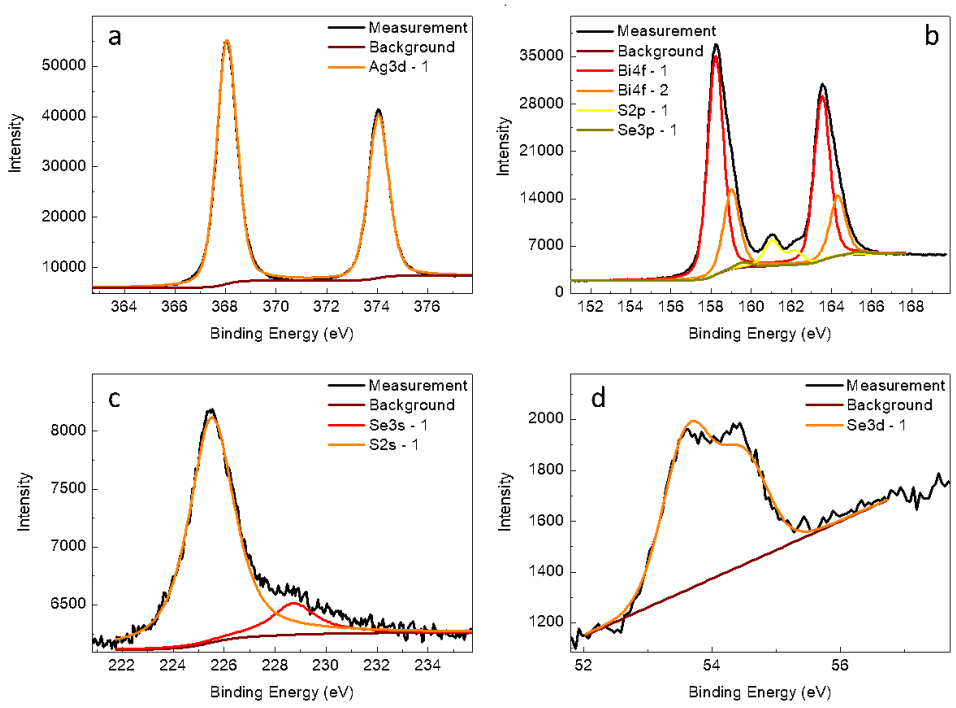

Figure 4.8: XPS spectra of AgBiSSe CNCs synthesized with metal iodide salts and mixed anion precursor (Se/(S+Se) = 0.1). (a) Ag - 3d, (b) Bi - 4f, (c) S-2s/Se-3s and (d) Se -3d regions.

4.3 Alloyed quaternary AgBiSSe CNCs

As the last part in this project, we investigated the possibility of synthesizing alloyed quaternary AgBiSSe CNCs under ambient conditions. This is an important part of this project, both as alloying in Ag-Bi-S-Se system is not investigated in nanocrystal form in depth yet, except very few reports [173], and also as it will give us a means to tune the bandgap of these CNCs due to different bandgaps of the $AgBiS_2$ and $AgBiSe_2$. We utilized a mixed anion precursor approach for the synthesis of the quaternary CNCs. For both sulfur and selenium can be dissolved in alkyl amines via formation of a amine-chalcogenide complex, we found beneficial to employ alkyl amines as the reaction medium for the synthesis of alloyed AgBiSSe CNCs. For the preliminary experiment, the synthesis was performed with Se/(S+Se) precursor ratio of 0.1. XPS spectra of the resulting CNCs confirmed the presence of Se-3d and S-2s/Se-3s peaks in the respective parts of the XPS spectrum, showing the effectiveness of our approach (Figure 4.8). It was sufficient to use a single doublet to fit Ag-3d spectrum similar to the pure ternary

materials (Figure 4.8a). Bi-4f spectrum required the use of two doublet located at 158.3 and 159.0 eV (Figure 4.8b). Moreover, similar to the case of pure $AgBiSe_2$ CNCs, the Se-3d 5/2 peak of AgBiSSe CNCs located at 54.6 eV confirmed that selenium was in 2- state and not oxidized under the conditions that the synthesis and purification steps were performed.

Table 4.3: Elemental analysis of AgBiSSe CNCs synthesized via metal iodide salts and mixed anion precursor (Se/(Se + S) = 0.1).

Ag	Bi	Se	S
1.00	0.70	0.12	0.76

The presence of both selenium and sulfur was verified with the presence of both S-2p and Se-3p peaks in the Bi-4f spectrum, as well as with the presence of Se-3d and S-2s/Se-3s peaks in the respective parts of the XPS spectrum (Figure 4.8c-d). The quantitative analysis of XPS results gave a Bi/Ag ratio of 0.70 and a Se/(S+Se) ratio of 0.12, close to the precursor ratio of 0.1 used for the synthesis (Table 4.3). This verifies that both of the anion precursors could effectively take part in the formation of the nanocrystals, as the final product contained considerable amount of sulfur.

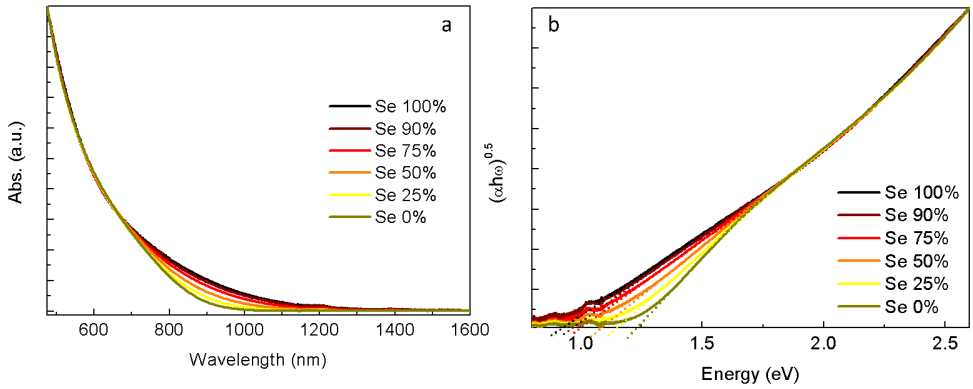

Figure 4.9: Absorption characteristics of AgBiSSe CNCs with respect to sulfur content. (a) Absorbance spectra and (b) Tauc plots of AgBiSSe CNCs.

After verification of the presence of both S and Se in the CNCs, we performed the same synthesis by employing different ratios of Se/S to show the bandgap tunability of the AgBiSSe CNCs. It was observed that the absorption characteristics of the CNCs was not affected significantly in the short wavelength region by alloying (Figure 4.9). This is an expected result since the absorption characteristics of $AgBiS_2$ and

$AgBiSe_2$ CNCs are very similar. Thus, alloying of these two materials does not result in a significant change in the short wavelength part of the absorption spectrum. Yet, the part of the absorption spectra after 700 nm showed a noticeable change with alloying. It was observed that the absorbance of CNCs in the 700-1200 nm region increased when the selenium/sulfur ratio of the nanocrystals increased. The Tauc plots of these alloyed AgBiSSe CNCs yielded a bandgap tuning range of 0.3 eV from 0.92 to 1.23 eV via alloying. This is an important result for this material family as the bandgap tuning for pure $AgBiS_2$ or $AgBiSe_2$ CNCs was found nontrivial via quantum confinement effect unlike other semiconducting CNCs, such as CdSe, CdTe, HgTe and PbS CNCs. [174–177] Thus, this bandgap tuning strategy can pave the way for better optimization of the optoelectronic properties of these CNCs to enhance the performance of the photovoltaics and thermoelectrics technologies based on AgBiSSe CNCs.

Although it is evident from the absorption characteristics of the obtained CNCs, we sought to verify the alloying via alternative methods. As XRD can directly give information about the physical ordering of the atoms in a material, we utilized this method to observe the change in interplanar distances that can result from partial replacement of S with Se. Because of the larger ionic size of selenium compared to that of sulfur, the presence of selenium in the crystal lattice causes an expansion of the lattice and increases the respective lattice parameters. Hence, it becomes possible to determine comparatively the sulfur/selenium ratio in alloyed nanocrystals using the shift of the peaks in the XRD spectra. [109, 178, 179]

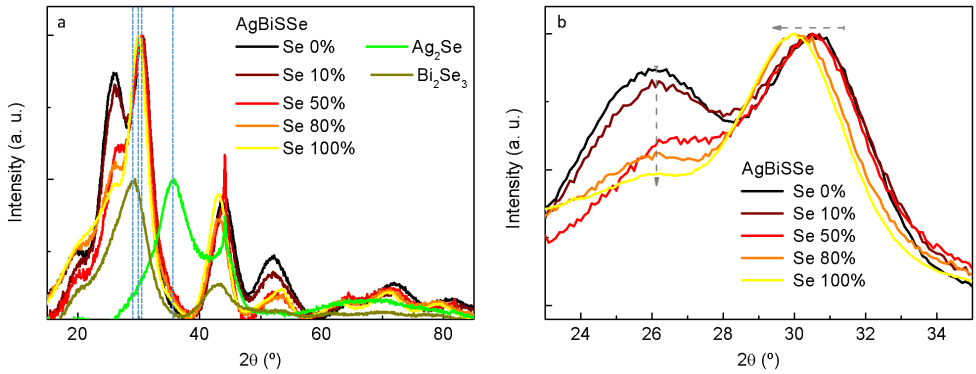

Figure 4.10: XRD of AgBiSSe CNCs with respect to S/Se ratio of the anion precursor. (a) XRD spectra of Ag_2Se, Bi_2Se_3 and AgBiSSe CNCs for various values of Se content (The positions of the main peaks of $AgBiS_2$, $AgBiSe_2$, Bi_2Se_3 and Ag_2Se are marked with blue dashed lines.). (b) A magnified version of (a) showing the shifting/diminishing of the two most prominent peaks of AgBiSSe CNCs for various values of Se content.

According to Bragg equation (Eq. 4.3), [180] it is expected for higher Se/S ratio to yield smaller Bragg angles. Here, λ is the wavelength of the X-ray beam (0.15046 nm for Cu Kα radiation), θ is the Bragg angle, and n is an integer number and d is the lattice spacing.

$$d = \frac{n\lambda}{2\sin(\theta)} \tag{4.3}$$

Table 4.4: Position of the main peak of AgBiSSe CNCs with respect to Se/(Se+S) ratio of the anion precursor and the corresponding lattice spacing calculated using Bragg equation.

Se/(S + Se)	0 %	10 %	50 %	80 %	100 %
2θ [°]	30.6	30.5	30.4	30.0	29.9
d [nm]	0.284	0.285	0.286	0.290	0.291

XRD analysis demonstrated that the peak located around 30° shifts towards lower angles with increasing Se content, as expected due to the larger ionic size of Se^{2-} with respect to S^{2-} (Figure 4.10). In addition, the peak located around 26° decreases gradually with the incorporation of more selenium into CNCs as this peak is strong for pure $AgBiS_2$ yet it has a very small amplitude for pure $AgBiSe_2$. [146, 173] The calculated lattice constant (using Eq. 4.3) is in line with the $< 200 >$ plane of the cubic phase silver bismuth chalcogenides (Table 4.4). For pure $AgBiS_2$ CNCs, the interplanar distance was measured to be 0.284 nm, which is very close to the value reported in the literature (0.282 nm, AMCSD 0009219). For pure $AgBiSe_2$ CNCs, this value was found to be 0.291 nm, which matches well with the values documented in previous studies. [181] In addition, no traces of binary products was detected in the XRD spectra of the alloyed AgBiSSe CNCs for any Se/S ratio. This is in direct accordance with our previous findings on $AgBiS_2$ and $AgBiSe_2$ CNCs. As stated before, although it is possible to form binary products using the same synthesis procedure, these binary products are unlikely to form if both cations are present simultaneously in the synthesis mixture.

TEM investigation of the samples demonstrated the formation of nanocrystals for all selenium ratios utilized in this study (Figure 4.11). High-resolution TEM images of the nanocrystals confirmed that the ambient condition synthesis yielded nanocrystalline material instead of amorphous nanoparticles. The presence of sharp peaks in the SAED image verified the formation of nanocrystalline phase, which is in support of the results obtained by XRD analysis.

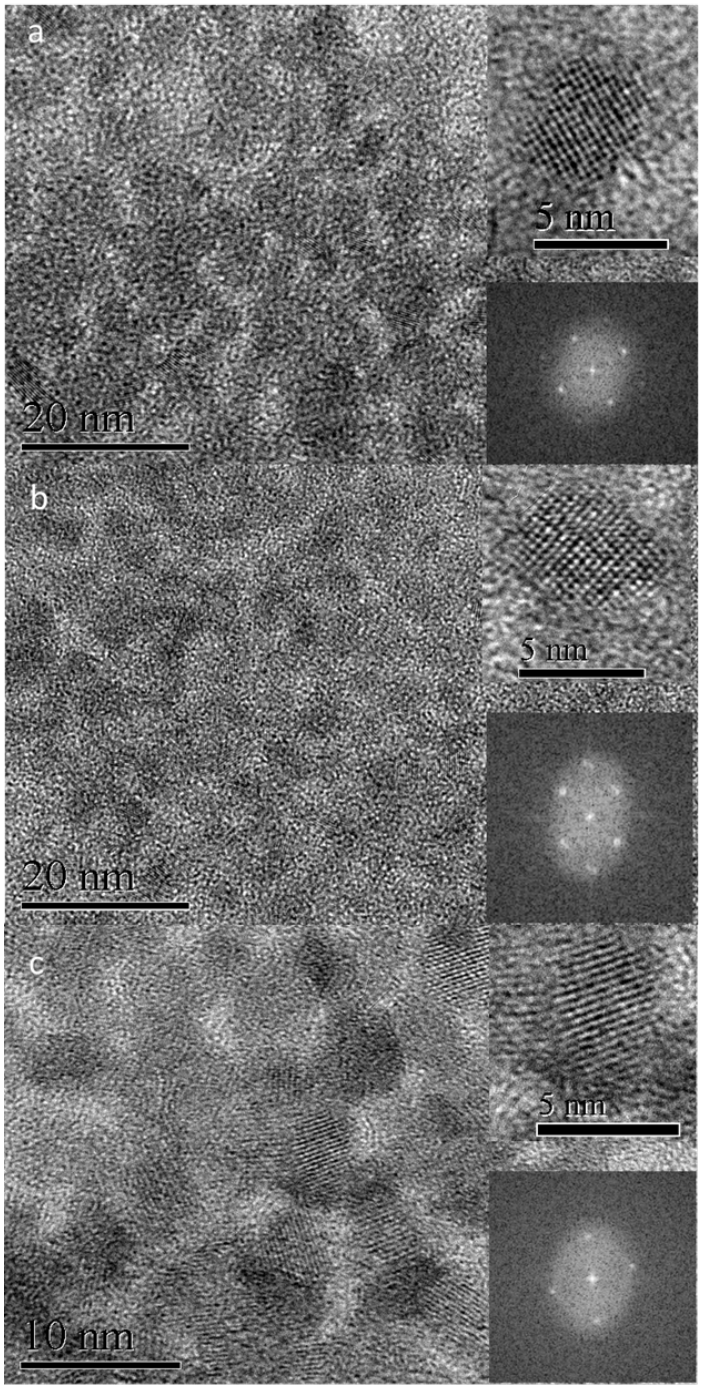

Figure 4.11: TEM images of AgBiSSe CNCs for different Se/(Se + S) ratios of (a) 75 %, (b) 50 % and (c) 25 %. Se (Insets: upper insets are HRTEM scans whereas lower insets show the SAED spectra of the individual nanocrystals.).

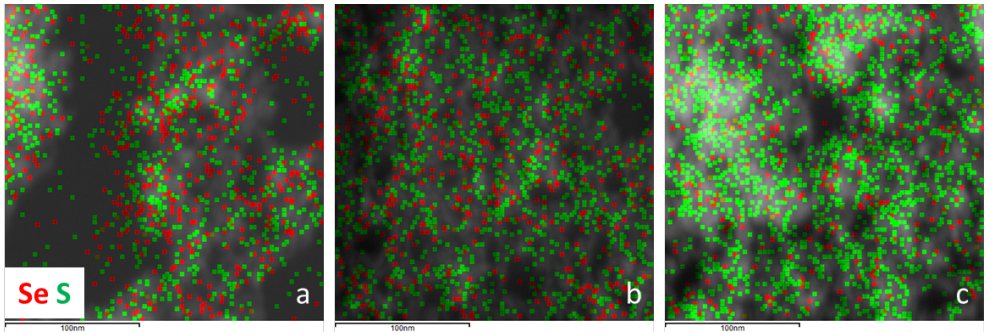

Figure 4.12: EDS elemental mapping (TEM) of AgBiSSe CNCs with (a) 75 %, (b) 50 % and (c) 25 % Se ratio (Red: selenium, green: sulfur).

The elemental mapping of AgBiSSe CNCs with different Se/(Se +S) ratios were carried out using a scanning transmission electron microscope (STEM) equipped with EDS. Elemental mapping images are provided in Figure 4.12 where the EDS signals of S and Se are superimposed on the dark field image to show the distribution of the anions throughout the samples. The results of EDS elemental mapping indicates that the distribution of anions in the samples are uniform and no phase segregation is present, which is in line with XRD results.

The composition analysis of the AgBiSSe CNCs showed that the selenium ratio in the precursor solution had a direct effect on the Se/S ratio of the resulting CNCs (Figure 4.13). The S-2s/Se-3s spectra of the all samples were fitted using one and two Gaussian - Lorentzian mixed curves for pure ($AgBiS_2$ and $AgBiSe_2$) and alloyed CNCs (AgBiSSe), respectively. The comparative analysis of the peak(s) present in these spectra demonstrated that Se/S ratio of the CNCs was in good agreement with the Se/S ratio of the precursor solution. By examining the spectra, it can be deduced that the peak located at $\sim$ 226 eV originates from S-2s orbital whereas the peak at $\sim$ 229 eV results from Se-3s orbital. The relation between the Se ratio of the precursor and the measured Se ratio of the resulting CNCs is given in Figure 4.13f. Ag-3d doublet of the samples were positioned around 368 eV, similar to the previous samples (Figure 4.14a-c). The change in Se ratio in these samples can also be confirmed via side-by-side analysis of Bi-4f spectra as both S-2p and Se-3p doublets are located within Bi-4f XPS window. The Se-3d doublet of the samples showed the same trend with varying precursor Se ratio. Thus, it can be concluded that the Se content of the resulting product can be tuned by controlling the selenium content of the precursor solution. For further comparison of the content of the samples, the elemental ratios of the CNCs (normalized to Ag-3d) are also provided in Table 4.5.

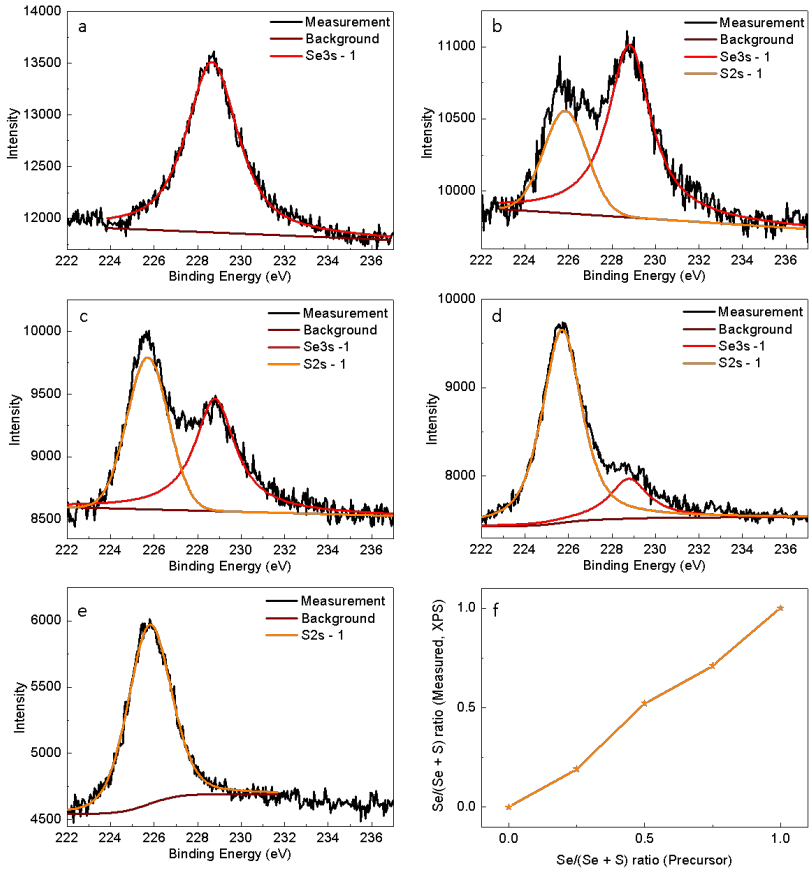

Figure 4.13: S-2s/Se-3s spectra of AgBiSSe nanocrystals for varying amounts of Se/(Se + S) ratios. (a) 100 %, (b) 75 %, (c) 50 %, (d) 25 % and (e) 0%. (f) The effect of Se/(Se+S) precursor ratio on the Se/(Se+S) ratio of the resulting CNCs.

Table 4.5: Elemental composition of the AgBiSSe CNCS synthesized with precursors of different Se/(Se + S) ratios.

Se/(Se+S)	Ag	Bi	Se	S
75 %	1.00	0.89	0.69	0.28
50 %	1.00	0.95	0.56	0.52
25 %	1.00	0.90	0.28	1.17

As a summary, we have demonstrated a simple yet effective room-temperature synthesis method for the environmentally friendly $AgBiSe_2$ nanocrystals that can be easily performed under ambient conditions using alkyl amine - alkyl thiol chemistry. In

addition, we have also shown the first solution-processed solar cell based on $AgBiSe_2$ CNCs. The fabricated devices show a preliminary power conversion efficiency of 2.6 %. Furthermore, we have provided a detailed study on the synthesis of alloyed AgBiSSe CNCs and proved that the bandgap of these CNCs can be tuned by simply changing the Se/S ratio. The formation of quaternary AgBiSSe CNCs has been verified via absorption and XRD measurements. This work paves the way towards photovoltaics-quality absorbers that are cheaper to produce and environmentally friendly from both a material and production perspectives and address the regulatory concerns and synthetic cost of colloidal nanocrystals based on Schlenk line approaches.

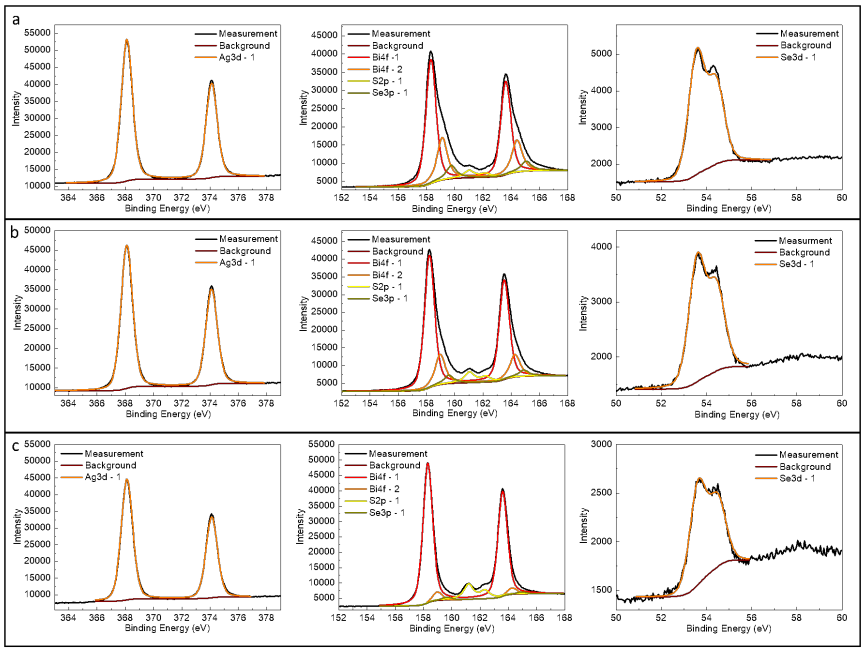

Figure 4.14: XPS scans of Ag-3d, Bi-4f and Se-3d orbitals for AgBiSSe CNCs with varying Se/(Se +S) ratios. (a) 75 %, (b) 50 % and (c) 25 % Se.

5

Conclusions and Outlook

Because of the negative effects of fossil fuel-based energy production, the need for low-carbon footprint energy production methods has gained importance. The future of renewable energy is supported by the fact that their carbon emission to the environment is virtually zero, which makes them an ideal solution for the global warming problem. Photovoltaics, being one of the promising renewable energy resources, offers an immense potential thanks to the unlimited energy of the Sun. Although various attempts have been made to overcome the efficiency, cost and toxicity problems, no solution to the photovoltaics that is both economically viable and environmentally friendly has been found so far. Yet, the current research trend in the field makes it clear that solution-processed solar cells may be the key to unlock the green energy problem of the world. In this thesis, we aimed to bring silver bismuth chalcogenide CNC solar cells closer to the photovoltaics market by addressing the following three major issues:

Synthesis Complexity: By eliminating the inert reaction environment and heating from the synthesis, we have been able to reduce the complexity of the setup used for the synthesis that originates from the hot-injection methods. The simplifications of the synthesis setup also relieves the scale constraints on the synthesis resulting from

the maintenance of inert atmosphere and low thermal fluctuations within the reaction flask. For the synthesis of silver bismuth chalcogenide CNCs, it has become possible to reduce the reaction setup down to a simple plastic reaction vessel and a magnetic stirrer.

Cost: One of the major challenges that has to be dealt with in photovoltaics is the unit cost. Due to the involvement of complex reaction setups and inert reaction conditions, the hot injection-based synthesis methods are inherently costlier than expectations. In addition, the scale constraint imposed by the hot-injection methods, as explained before, imposes further limits on the attainable minimum unit cost. With the elimination of the hot-injection methods in the synthesis of $AgBiS_2$ CNCs, it becomes possible to obtain at least 60 % reduction in CNC synthesis cost.

Film deposition: The prior state-of-the-art $AgBiS_2$ CNC solar cells require use of the layer-by-layer deposition method. This method, although convenient for lab-scale fabrication, is not suitable for industry scale manufacturing due to high material loss resulting from repeated spin coating cycles. By performing the film deposition in a single step with the use of the new ligand, ethanethiol, we reduced both the amount of the required $AgBiS_2$ CNCs and the fabrication time of CNC solar cells. It was also shown that the same method could be used for the fabrication of $AgBiSe_2$ CNC solar cells.

Although promising progress in silver bismuth chalcogenide CNC photovoltaics has been made with the introduction of the ambient synthesis method, the material properties limiting the device performance still stand as the major obstacle preventing the achievement of higher PCE. The major limiting property of $AgBiS_2$ CNC solar cells is the upper limit on the thickness of $AgBiS_2$ CNC layer that allows sufficient carrier extraction (typically less than 100 nm). Considering that this material has good optical characteristics, such as a bandgap of 1.1 - 1.3 eV and an absorption coefficient as high as 10^5 cm^{-1}, it is expected to obtain higher PCE with the enhancement of the drift and diffusion lengths via increasing mobility-lifetime product of this material. Doping and alloying strategies can be used to improve the charge carrier lifetime and mobility. For $AgBiS_2$, this can be achieved by substitution of S with either Se or Te.[159,172] The same strategy can also be utilized by substitution of Ag and Bi with Cu, and Sb, respectively. As another remedy, physical structure of the solar cell can be optimized to obtain both high absorption of the light and short distance for carrier transport. From this point, the use of bulk heterojunction can be a good strategy to employ to increase the device performance.[73,181]

In short, we have shown that a low-cost environmentally friendly solution can

be made possible with the use of ambient condition synthesis methods. Via careful selection of the precursors and by meticulous design and optimization of the reaction, it has been demonstrated that $AgBiS_2$ CNC solar cells are capable of giving a PCE as high as 5.5 % only for a fraction of the cost of $AgBiS_2$ CNCs synthesized via Schlenk-line setup. Following the strategy that was used for $AgBiS_2$ CNCs, we also developed an ambient synthesis method for $AgBiSe_2$ CNCs. The properties of the resulting $AgBiSe_2$ CNCs were demonstrated via both optical and structural characterization methods. The solution-processed $AgBiSe_2$ CNC solar cells showed a PCE up to 2.6 %. We demonstrated that the two methods shown so far could be combined for the synthesis of alloyed AgBiSSe CNCs. It was verified via optical spectroscopy that the bandgap of the alloyed CNCs could be tuned simply by changing the ratio of selenium-to-sulfur ratio of the precursor solution. Although this work is focused on silver bismuth chalcogenides, the same methods can be applied for the synthesis of other CNCs, which may bring the long-lasting dream of green energy one-step closer to being a reality.

Appendices

A

Supplementary Data for Chapter 2

Chemicals and Materials: All reagents were purchased from Sigma-Aldrich, except $Bi(OAc)_3$ which was purchased from Alfa Aesar and AgI which was obtained from Strem Chemicals. PTB7 (poly[(4,8-bis(2-ethylhexyloxy)-benzo(1,2-b:4,5-b)dithiophene)-2,6-diyl-alt-(4-(2-ethylhexyl)-3-fluorothieno[3,4-b]thiophene-)-2-carboxylate-2-6-diyl)]) was purchased from 1-material.

Synthesis of $AgBiS_2$ CNCs Based on Hot Injection: For hot-injection synthesis, silver acetate (0.8 mmol), bismuth(III) acetate (1 mmol), and oleic acid (17 mmol) were charged into a three-neck flask, as described previously. [110]The flask was pumped down at 90 °C to eliminate the air and moisture from the reaction environment. After the formation of metal-oleates, the flask was filled with argon gas, and the temperature was ramped up to 100 °C. Then, a solution of HMS (1 mmol) in 1-octadecene (5 mL) was prepared in a drybox and swiftly injected into the flask. The flask was left to cool down to room temperature. $AgBiS_2$ CNCs were separated from the reaction mixture with addition of ethanol and centrifugation. The nanocrystals were dispersed in toluene with a concentration of 20 g/L and the dispersion was filtered through 0.22 μm PTFE filter and used as it is.

Synthesis of $AgBiS_2$ Nanocrystals Based on Room Temperature and Ambient Atmosphere: For room-temperature synthesis, AgI (0.2 mmol) and BiI_3 (0.2 mmol) were dissolved in amines (4 mL) and stirred. In a separate vial, a sulfur-amine solution (4 M) was prepared. A suitable portion of this solution (80 μL) was swiftly injected into vigorously stirring AgI-BiI_3 mixture. Then, 1-octanethiol (0.15 mL) was added, and the $AgBiS_2$ nanocrystals were separated by the addition of acetonitrile and centrifugation. Nanocrystals were dispersed in octane with a concentration of 60 g/L and filtered through 0.22 μm PTFE filter. The recipe above can be easily upscaled to obtain more $AgBiS_2$ CNCs per batch. For an upscaled synthesis, we use AgI (1.0 mmol), BiI_3(1.0 mmol) and S precursor (0.5 ml, 4 M). Also, the amount of 1-octanethiol is increased to 0.5 ml. The cleaning of CNCs are carried out using the same method given above.

Material Characterization: UV-vis absorption spectrum was measured using a Cary 5000 spectrophotometer using 1 cm optical path cuvettes using dilute nanocrystal dispersions in octane. TEM was performed using a JEOL 2100 microscope with an acceleration voltage of 200 kV at the Scientific and Technological Center of the University of Barcelona (CCiT-UB). Samples were prepared by dropcasting dilute $AgBiS_2$ dispersions onto carbon-coated copper grids. XRD spectra were obtained using a PANalytical XPert PRO MPD Alpha1 powder diffractometer with Cu Kα radiation (λ = 1.5406 Å, 45 kV, 40 mA). The samples were prepared by dropcasting a concentrated dispersion of $AgBiS_2$ nanocrystals onto glass slides. X-ray and Ultraviolet photoelectron spectroscopy (XPS/UPS) were performed with a Phoibos 150 instrument equipped with a monochromatic Kα X-ray source (1486.74 eV) at the Institut Catala de Nanociencia i Nanotechnologia (ICN2). The spectra were corrected in energy by using the adventitious carbon peak (C 1s, 284.8 eV) as the reference. Atomic ratios were calculated by integrating elemental peaks with Shirley background profile. For fitting of peaks a combination of Lorentzian and Gaussian functions were utilized. XPS and UPS samples were prepared by treating the films with either TMAI (1 g/L in methanol for Schlenk-line $AgBiS_2$) or ET (0.2 % in methanol for n-octylamine $AgBiS_2$). Fourier transform infrared spectroscopy (FTIR) was performed with a Cary 600 FTIR instrument. For all FTIR measurements, double side polished silicon wafers were used as the substrate. The samples were prepared by spin coating. To evaporate the unbound amines and/or solvents, the samples were annealed on a hot plate at 90 °C. Iodine-amine solution was prepared by dissolving elemental iodine (0.8 mmol) in n-octylamine (1 mL) in air. N-octylammonium iodide was prepared by the reaction of n-octylamine with hyriodic acid in ethanol. For FTIR measurements, the obtained white powder was spun-coated from ethanol solution.

B

Supplementary Data for Chapter 3

Device Fabrication: ITO substrates were cleaned by sonication in soapy water, DI water, acetone, and isopropanol sequentially. Then, a solution of Zn^{2+} was prepared in a glovebox by dissolving $Zn(acetate)_2{\cdot}2H_2O$ (500 mg) in 2-methoxyethanol (5 mL) and ethanolamine (142 μL). This solution was spread on cleaned ITO substrates via spin coating at 3000 rpm for 30 s. After spin coating, the substrates were placed on top of a hot plate at 200 °C. After 30 min of annealing, the substrates were left to cool down and the same procedure was repeated one more time to obtain a ZnO thickness of 45 nm. TMAI-treated $AgBiS_2$ films were deposited via multiple spin coating steps following the recipe of the previously published study. [110] For the deposition of the ET-treated solar cells, we utilized a faster route. Basically, one drop of concentrated $AgBiS_2$ dispersion was dropped onto ZnO-coated substrate spinning at 2000 rpm. Then, the spinning was stopped and ethanethiol (ET; 0.2 % in methanol, 5 drops) was dispensed. After 15 s of soaking, the sample was spun to dryness. Then, the sample was rinsed with methanol and spun to dryness. After the deposition, $AgBiS_2$ film was annealed on a hot plate in air at 100 °C for 10 min. Then, a hole transport layer was deposited by spin coating a PTB7 solution (5 g/L in dichlorobenzene) at 2000 rpm. Top contact was formed by thermally evaporating MoO_3 (3 nm) and Ag (150 nm) using a Kurt J. Lesker Nano36

thermal evaporator. A shadow mask with 2 mm circular holes was used to define the top contact profile.

Device Characterization: Solar cell characterization was performed using a Newport Oriel Sol3A solar simulator equipped with an AM1.5 filter in air. Current-voltage data were collected by a Keithley 2400 source meter. For the external quantum efficiency (EQE) measurement, a Stanford Research SR570 transimpedance amplifier connected to a Stanford Research SR830 lock-in amplifier was used. The monochromatic light was generated by a Newport Cornerstone 260 monochromator and the spectrum was corrected using calibrated Newport photodetectors (UV-818 and IR-818) as the reference. A FiberTech Optica LED lightsource and an Agilent 4000X oscilloscope were used to measure J_{SC} and V_{OC} as a function of light intensity. For J_{SC} and V_{OC}, 50 Ω and 1 MΩ input terminals of the oscilloscope were utilized, respectively. A Vortran Stradus laser with a wavelength of 637 nm was used as the excitation source for transient photovoltage (TPV) and transient photocurrent (TPC) measurements for the calculation of density of trap states (DOTS). The thickness of the films was measured using a KLA-Tencor Alpha-Step IQ Surface Profilometer. The films were prepared by spin coating the material on ITO glass, and the measurement point is formed by scratching the film with a sharp metal tip.

C

Supplementary Data for Chapter 4

Chemicals and Materials: All reagents were purchased from Sigma-Aldrich, AgI which was obtained from Strem Chemicals. P3HT (poly[3-hexylthiophene-2,5-diyl]) was purchased from Rieke materials.

Synthesis of $AgBiSe_2$ CNCs: Se precursor used in this study is prepared by dissolving SeO_2 in methanol with a concentration of 2 M. In a separate container AgI (0.2 mmol) and BiI_3 (0.2 mmol) powders are dissolved in 4 ml of n-octylamine. Then, Se precursor solution is added to the vigorously stirring AgI-BiI_3 solution. At this stage, no nucleation occurs for n-octylamine alone is not sufficient to reduce SeO_2 (See Figure C.1). When 0.5 ml of 1-octanethiol is injected into the reaction mixture the solution obtains a dark color due to the formation of $AgBiSe_2$ CNCs. After the synthesis, $AgBiSe_2$ CNCs are purified by addition of acetonitrile and centrifugation. After purification, $AgBiSe_2$ CNCs are dispersed in octane and filtered through 0.22 μm PTFE filters. For device fabrication, a dispersion of $AgBiSe_2$ CNCs with a concentration of 30 mg ml^{-1} is used. For the synthesis of Ag_2Se and Bi_2Se_3 CNCs, only the respective metal iodide is dissolved in n-octylamine and the amount of Se precursor is adjusted accordingly.

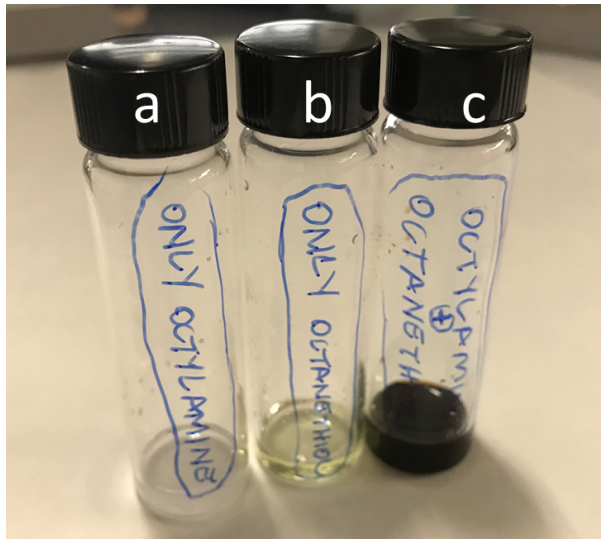

Figure C.1: Dissolution of SeO_2 in (a) only n-octylamine, (b) only 1-octanethiol and (c) a mixture of n-octylamine and 1-octanethiol.

Synthesis of alloyed AgBiSSe CNCs: The synthesis of AgBiSSe CNCs are carried out similar to $AgBiSe_2$ CNCs. A Se precursor is prepared by dissolving SeO_2 in methanol with a concentration of 2 M. In a separate container AgI (0.2 mmol) and BiI_3 (0.2 mmol) powders are dissolved in 4 ml of n-octylamine. Then, Se precursor solution is added to the vigorously stirring AgI-BiI_3 solution. To initiate the nucleation a sulfur solution in 0.5 ml of 1-octanethiol is injected into the metal iodide solution. The color of the solution darkens quickly after the injection due to the formation of AgBiSSe CNCs. After the synthesis, AgBiSSe CNCs are purified similar to $AgBiSe_2$ CNCs.

Material Characterization: UV-vis absorption spectrum was measured using a Cary 5000 spectrophotometer using 1 cm optical path cuvettes using dilute nanocrystal dispersions in octane. TEM was performed using a JEOL 2100 microscope with an acceleration voltage of 200 kV at the Scientific and Technological Center of the University of Barcelona (CCiT-UB). Samples were prepared by dropcasting dilute AgBiSSe dispersions onto carbon-coated copper grids. XRD spectra were obtained using a Rigaku SmartLab II powder diffractometer with Cu Kα radiation (λ = 1.5406 Å, 45 kV, 40 mA). The samples were prepared by dropcasting a concentrated dispersion of $AgBiSe_2$ nanocrystals onto glass slides. X-ray and Ultraviolet photoelectron spectroscopy (XPS/UPS) were performed with a Phoibos 150 instrument equipped with a monochromatic Kα X-ray source (1486.74 eV) at the Institut Catala de Nanociencia i Nanotechnologia (ICN2). The spectra were corrected in energy by using the adven-

titious carbon peak (C 1s, 284.8 eV) as the reference. Atomic ratios were calculated by integrating elemental peaks with Shirley background profile. For fitting of peaks a combination of Lorentzian and Gaussian functions were utilized. XPS and UPS samples were prepared by treating the films with ethanethiol in methanol (0.2 % v/v).

Fabrication of $AgBiSe_2$ CNC solar cells: After cleaning by sonication in soapy water, deionized water, acetone and isopropanol, a 45 nm-thick ZnO layer is deposited on ITO substrates by sol-gel process. A solution of $Zn(acetate)_2{\cdot}2H_2O$ (500 mg in 5 ml of 2-methoxyethanol and 142 μl of ethanolamine) is spun coated on clean ITO substrates at 3000 rpm. Then, then substrates are annealed at 200 °C for 30 minutes. After cooling to room temperature, one more ZnO layer is deposited using the same process to obtain a 45 nm-thick ZnO layer. After the deposition of ZnO, $AgBiSe_2$ CNCs are spun coated at 2000 rpm. Then, 5 drops of thiophenol (0.2 % v/v in ethanol) is dropped on $AgBiSe_2$ CNC layer. After rinsing excess thiophenol with ethanol, 5 drops of TMAI solution in methanol (1 mg ml^{-1}) is dropped onto the layer. Then, $AgBiSe_2$ CNC layer is rinsed with methanol. To complete the device, a PTB7 layer is spun coated at 2000 rpm using a P3HT solution in dichlorobenzene (2.5 mg ml^{-1}) and MoO_3 (3 nm) and Ag (150 nm) layers are deposited by thermal evaporation.

Device Characterization: Solar cell characterization was performed using a Newport Oriel Sol3A solar simulator equipped with an AM1.5 filter in air. Current-voltage data were collected by a Keithley 2400 source meter. For the external quantum efficiency (EQE) measurement, a Stanford Research SR570 transimpedance amplifier connected to a Stanford Research SR830 lock-in amplifier was used. The monochromatic light was generated by a Newport Cornerstone 260 monochromator and the spectrum was corrected using calibrated Newport photodetectors (UV-818 and IR-818) as the reference.

Bibliography

[1] P. Friedlingstein, M. W. Jones, and et. al, "Global Carbon Budget 2019," *Earth Syst. Sci. Data*, vol. 11, no. 4, pp. 1783–1838, 2019. (see p. 2)

[2] B. J. Henley and A. D. King, "Trajectories toward the 1.5 C Paris target: Modulation by the Interdecadal Pacific Oscillation," *Geophys. Res. Lett.*, vol. 44, no. 9, pp. 4256–4262, 2017. (see p. 2)

[3] T. S. Ledley, E. T. Sundquist, S. E. Schwartz, D. K. Hall, J. D. Fellows, and T. L. Killeen, "Climate change and greenhouse gases," *EOS., Trans. AGU.*, vol. 80, no. 39, pp. 453–458, 1999. (see p. 2)

[4] World Energy Council, "World Energy Insights Brief 2019," 2020. https://www.worldenergy.org/assets/downloads/WEInsights-Brief-Global-Energy-Scenarios-Comparison-Review-R02.pdf. (see p. 2)

[5] W. A. Hermann, "Quantifying global exergy resources," *Energy*, vol. 31, no. 12, pp. 1685–1702, 2006. (see p. 2)

[6] B. M. Kayes, H. Nie, R. Twist, S. G. Spruytte, F. Reinhardt, I. C. Kizilyalli, and G. S. Higashi, "27.6% Conversion efficiency, a new record for single-junction solar cells under 1 sun illumination," in *2011 37th IEEE Photovoltaic Specialists Conference*, pp. 000004–000008, 2011. (see p. 2)

[7] W. Shockley and H. J. Queisser, "Detailed Balance Limit of Efficiency of pn Junction Solar Cells," *J. Appl. Phys*, vol. 32, no. 3, pp. 510–519, 1961. (see p. 2)

[8] J. F. Geisz, R. M. France, K. L. Schulte, M. A. Steiner, A. G. Norman, H. L. Guthrey, M. R. Young, T. Song, and T. Moriarty, "Six-junction IIIV solar cells with 47.1% conversion efficiency under 143 Suns concentration," *Nat. Energy.*, vol. 5, no. 4, pp. 326–335, 2020. (see p. 2)

[9] Renewable Energy Agency (IRENA), "Renewable Power Generation Costs in 2018," 2019. https://www.irena.org/publications/2019/May/Renewable-power-generation-costs-in-2018. (see p. 2)

[10] M. Vellini, M. Gambini, and V. Prattella, "Environmental impacts of PV technology throughout the life cycle: Importance of the end-of-life management for Si-panels and CdTe-panels," *Energy*, vol. 138, pp. 1099–1111, 2017. (see p. 3)

[11] J. Wu, X. Che, H.-C. Hu, H. Xu, B. Li, Y. Liu, J. Li, Y. Ni, X. Zhang, and X. Ouyang, "Organic solar cells based on cellulose nanopaper from agroforestry residues with an efficiency of over 16% and effectively wide-angle light capturing," *J. Mater. Chem. A*, vol. 8, no. 11, pp. 5442–5448, 2020. (see p. 3)

[12] D. R. Pernik, M. Gutierrez, C. Thomas, V. R. Voggu, Y. Yu, J. van Embden, A. J. Topping, J. J. Jasieniak, D. A. Vanden Bout, R. Lewandowski, and B. A. Korgel, "Plastic Microgroove Solar Cells Using $CuInSe_2$ Nanocrystals," *ACS Energy Lett.*, vol. 1, no. 5, pp. 1021–1027, 2016. (see p. 3)

[13] The European Parliament and the Council of the European Union, "Directive 2002/95/EC of the European Parliament and of the Council of 27 January 2003 on the restriction of the use of certain hazardous substances in electrical and electronic equipment," *OJEU*, vol. L37, pp. 19–23, 2003. (see p. 3)

[14] A. Ramos-Ruiz, J. V. Wilkening, J. A. Field, and R. Sierra-Alvarez, "Leaching of cadmium and tellurium from cadmium telluride (CdTe) thin-film solar panels under simulated landfill conditions," *J. Hazard. Mater*, vol. 336, pp. 57–64, 2017. (see p. 3)

[15] P. Nain and A. Kumar, "Identifying Issues in Assessing Environmental Implications of Solar PVs-Related Waste," in *Recent Developments in Waste Management* (A. S. Kalamdhad, ed.), Lecture Notes in Civil Engineering, pp. 71–90, Springer, 2020. (see p. 3)

[16] J. W. Morgan and E. Anders, "Chemical composition of Earth, Venus, and Mercury," *PNAS*, vol. 77, no. 12, pp. 6973–6977, 1980. (see pp. 4 and 18)

[17] W. Smith, "Effect of Light on Selenium During the Passage of An Electric Current*," *Nature*, vol. 7, no. 173, pp. 303–303, 1873. (see p. 4)

[18] W. G. Adams and R. E. Day, "The action of light on selenium," *Proc. R. Soc. Lond.*, vol. 25, no. 171-178, pp. 113–117, 1877. (see p. 4)

[19] A. Einstein, "ber einen die Erzeugung und Verwandlung des Lichtes betreffenden heuristischen Gesichtspunkt," *Ann. Phys.*, vol. 322, no. 6, pp. 132–148, 1905. (see p. 4)

[20] APS News, "Bell Labs Demonstrates the First Practical Silicon Solar Cell," 2020-03-24. http://www.aps.org/publications/apsnews/200904/physicshistory.cfm. (see p. 4)

[21] D. K. Schroder, *Semiconductor Material and Device Characterization.* John Wiley & Sons, Inc., 3 ed., 2005. (see pp. 6, 9, and 15)

[22] J. Dron, Q. Jeangros, J. Cattin, J. Haschke, L. Antognini, C. Ballif, and M. Boccard, "23.5%-efficient silicon heterojunction silicon solar cell using molybdenum oxide as hole-selective contact," *Nano Energy*, vol. 70, p. 104495, 2020. (see p. 7)

[23] K. Yoshikawa, H. Kawasaki, W. Yoshida, T. Irie, K. Konishi, K. Nakano, T. Uto, D. Adachi, M. Kanematsu, H. Uzu, and K. Yamamoto, "Silicon heterojunction solar cell with interdigitated back contacts for a photoconversion efficiency over 26%," *Nat. Energy*, vol. 2, no. 5, pp. 1–8, 2017. (see pp. 7 and 17)

[24] M. M. Tavakoli, D. Bi, L. Pan, A. Hagfeldt, S. M. Zakeeruddin, and M. Grtzel, "Adamantanes Enhance the Photovoltaic Performance and Operational Stability of Perovskite Solar Cells by Effective Mitigation of Interfacial Defect States," *Adv. Energy Mater*, vol. 8, no. 19, p. 1800275, 2018. (see p. 7)

[25] N. J. Jeon, J. H. Noh, Y. C. Kim, W. S. Yang, S. Ryu, and S. I. Seok, "Solvent engineering for high-performance inorganicorganic hybrid perovskite solar cells," *Nat. Mater.*, vol. 13, no. 9, pp. 897–903, 2014. (see p. 7)

[26] M. Wei, K. Xiao, G. Walters, R. Lin, Y. Zhao, M. I. Saidaminov, P. Todorovi, A. Johnston, Z. Huang, H. Chen, A. Li, J. Zhu, Z. Yang, Y.-K. Wang, A. H. Proppe, S. O. Kelley, Y. Hou, O. Voznyy, H. Tan, and E. H. Sargent, "Combining Efficiency and Stability in Mixed TinLead Perovskite Solar Cells by Capping Grains with an Ultrathin 2D Layer," *Adv. Mater.*, vol. 32, no. 12, p. 1907058, 2020. (see p. 7)

[27] G. Hodes and P. V. Kamat, "Understanding the Implication of Carrier Diffusion Length in Photovoltaic Cells," *J. Phys. Chem. Lett.*, vol. 6, no. 20, pp. 4090–4092, 2015. (see p. 8)

[28] V. K. Khanna, "Physical understanding and technological control of carrier lifetimes in semiconductor materials and devices: A critique of conceptual develop-

ment, state of the art and applications," *Prog. Quantum. Electron.*, vol. 29, no. 2, pp. 59–163, 2005. (see p. 9)

[29] W. Tress, M. Yavari, K. Domanski, P. Yadav, B. Niesen, J. P. Correa Baena, A. Hagfeldt, and M. Graetzel, "Interpretation and evolution of open-circuit voltage, recombination, ideality factor and subgap defect states during reversible light-soaking and irreversible degradation of perovskite solar cells," *Energy Environ. Sci.*, vol. 11, no. 1, pp. 151–165, 2018. (see pp. 9, 14, and 59)

[30] K. Chen, A. J. Barker, F. L. C. Morgan, J. E. Halpert, and J. M. Hodgkiss, "Effect of Carrier Thermalization Dynamics on Light Emission and Amplification in Organometal Halide Perovskites," *J. Phys. Chem. Lett.*, vol. 6, no. 1, pp. 153–158, 2015. (see p. 9)

[31] J. M. Richter, F. Branchi, F. Valduga de Almeida Camargo, B. Zhao, R. H. Friend, G. Cerullo, and F. Deschler, "Ultrafast carrier thermalization in lead iodide perovskite probed with two-dimensional electronic spectroscopy," *Nat. Commun.*, vol. 8, no. 1, 2017. (see p. 9)

[32] T. Tiedje, E. Yablonovitch, G. Cody, and B. Brooks, "Limiting efficiency of silicon solar cells," *IEEE Trans Electron Devices*, vol. 31, no. 5, pp. 711–716, 1984. (see p. 9)

[33] W. Shockley and W. T. Read, "Statistics of the Recombinations of Holes and Electrons," *Phys. Rev.*, vol. 87, no. 5, pp. 835–842, 1952. (see p. 9)

[34] O. J. Sandberg, A. Sundqvist, M. Nyman, and R. sterbacka, "Relating Charge Transport, Contact Properties, and Recombination to Open-Circuit Voltage in Sandwich-Type Thin-Film Solar Cells," *Phys. Rev. Appl*, vol. 5, no. 4, 2016. (see p. 10)

[35] D. Long and J. Myers, "Ionized-Impurity Scattering Mobility of Electrons in Silicon," *Phys. Rev.*, vol. 115, no. 5, pp. 1107–1118, 1959. (see p. 10)

[36] S. Qin, S. A. Prussin, J. Reyes, Y. J. Hu, and A. McTeer, "Study of Carrier Mobility of Low-Energy High-Dose Ion Implantations," *IEEE Trans. Plasma Sci.*, vol. 39, no. 1, pp. 587–592, 2011. (see p. 10)

[37] P. Norton, T. Braggins, and H. Levinstein, "Impurity and Lattice Scattering Parameters as Determined from Hall and Mobility Analysis in n -Type Silicon," *Phys. Rev. B*, vol. 8, no. 12, pp. 5632–5653, 1973. (see p. 10)

[38] M. Courel, J. Andrade-Arvizu, and O. Vigil-Galn, "Loss mechanisms influence on Cu_2ZnSnS_4/CdS-based thin film solar cell performance," *Solid State Electron.*, vol. 111, pp. 243–250, 2015. (see p. 12)

[39] T. Kirchartz and J. Nelson, "Meaning of reaction orders in polymer:fullerene solar cells," *Phys. Rev. B*, vol. 86, no. 16, 2012. (see p. 14)

[40] X. Miao, S. Tongay, M. K. Petterson, K. Berke, A. G. Rinzler, B. R. Appleton, and A. F. Hebard, "High Efficiency Graphene Solar Cells by Chemical Doping," *Nano Lett.*, vol. 12, no. 6, pp. 2745–2750, 2012. (see p. 14)

[41] W. Schottky, "Vereinfachte und erweiterte theorie der randschicht-gleichrichter," *Z. Physik*, vol. 118, no. 9, pp. 539–592, 1942. (see p. 14)

[42] J. P. Clifford, K. W. Johnston, L. Levina, and E. H. Sargent, "Schottky barriers to colloidal quantum dot films," *Appl. Phys. Lett.*, vol. 91, no. 25, p. 253117, 2007. (see p. 14)

[43] A. H. Ip, S. M. Thon, S. Hoogland, O. Voznyy, D. Zhitomirsky, R. Debnath, L. Levina, L. R. Rollny, G. H. Carey, A. Fischer, K. W. Kemp, I. J. Kramer, Z. Ning, A. J. Labelle, K. W. Chou, A. Amassian, and E. H. Sargent, "Hybrid passivated colloidal quantum dot solids," *Nat. Nanotechnol.*, vol. 7, no. 9, pp. 577–582, 2012. (see pp. 15 and 59)

[44] F. J. Morin and J. P. Maita, "Electrical Properties of Silicon Containing Arsenic and Boron," *Phys. Rev*, vol. 96, no. 1, pp. 28–35, 1954. (see p. 17)

[45] J. Benick, A. Richter, R. Mller, H. Hauser, F. Feldmann, P. Krenckel, S. Riepe, F. Schindler, M. C. Schubert, M. Hermle, A. W. Bett, and S. W. Glunz, "High-Efficiency n-Type HP mc Silicon Solar Cells," *IEEE J. Photovolt.*, vol. 7, no. 5, pp. 1171–1175, 2017. (see p. 17)

[46] M. Izu and T. Ellison, "Roll-to-roll manufacturing of amorphous silicon alloy solar cells with in situ cell performance diagnostics," *Sol. Energy Mater Sol.*, vol. 78, no. 1-4, pp. 613–626, 2003. (see p. 17)

[47] D. Carlson, "Amorphous silicon solar cells," *IEEE Trans Electron Devices*, vol. 24, no. 4, pp. 449–453, 1977. (see p. 17)

[48] N. Zhao, T. P. Osedach, L.-Y. Chang, S. M. Geyer, D. Wanger, M. T. Binda, A. C. Arango, M. G. Bawendi, and V. Bulovic, "Colloidal PbS Quantum Dot Solar Cells with High Fill Factor," *ACS Nano*, vol. 4, no. 7, pp. 3743–3752, 2010. (see p. 18)

[49] J. Gao, J. M. Luther, O. E. Semonin, R. J. Ellingson, A. J. Nozik, and M. C. Beard, "Quantum Dot Size Dependent J - V Characteristics in Heterojunction ZnO/PbS Quantum Dot Solar Cells," *Nano Lett.*, vol. 11, no. 3, pp. 1002–1008, 2011. (see p. 18)

[50] J. Dore, D. Ong, S. Varlamov, R. Egan, and M. A. Green, "Progress in Laser-Crystallized Thin-Film Polycrystalline Silicon Solar Cells: Intermediate Layers, Light Trapping, and Metallization," *IEEE J. Photovolt.*, vol. 4, no. 1, pp. 33–39, 2014. (see p. 18)

[51] Solar Frontier, "Solar Frontier Achieves World Record Thin-Film Solar Cell Efficiency of 23.35%," 2017. http://www.solar-frontier.com/eng/news/2019/0117_press.html. (see p. 18)

[52] C. Yan, J. Huang, K. Sun, S. Johnston, Y. Zhang, H. Sun, A. Pu, M. He, F. Liu, K. Eder, L. Yang, J. M. Cairney, N. J. Ekins-Daukes, Z. Hameiri, J. A. Stride, S. Chen, M. A. Green, and X. Hao, "Cu_2ZnSnS_4 solar cells with over 10% power conversion efficiency enabled by heterojunction heat treatment," *Nat. Energy*, vol. 3, no. 9, pp. 764–772, 2018. (see p. 18)

[53] M. Powalla, S. Paetel, E. Ahlswede, R. Wuerz, C. D. Wessendorf, and T. Magorian Friedlmeier, "Thinfilm solar cells exceeding 22% solar cell efficiency: An overview on CdTe-, Cu(In,Ga)Se_2 -, and perovskite-based materials," *Appl. Phys. Rev.*, vol. 5, no. 4, p. 041602, 2018. (see p. 18)

[54] D. P. McMeekin, S. Mahesh, N. K. Noel, M. T. Klug, J. Lim, J. H. Warby, J. M. Ball, L. M. Herz, M. B. Johnston, and H. J. Snaith, "Solution-Processed All-Perovskite Multi-junction Solar Cells," *Joule*, vol. 3, no. 2, pp. 387–401, 2019. (see p. 18)

[55] L. Meng, Y. Zhang, X. Wan, C. Li, X. Zhang, Y. Wang, X. Ke, Z. Xiao, L. Ding, R. Xia, H.-L. Yip, Y. Cao, and Y. Chen, "Organic and solution-processed tandem solar cells with 17.3% efficiency," *Science*, vol. 361, no. 6407, pp. 1094–1098, 2018. (see p. 18)

[56] Y. Lin, B. Adilbekova, Y. Firdaus, E. Yengel, H. Faber, M. Sajjad, X. Zheng, E. Yarali, A. Seitkhan, O. M. Bakr, A. ElLabban, U. Schwingenschlgl, V. Tung, I. McCulloch, F. Laquai, and T. D. Anthopoulos, "17% Efficient Organic Solar Cells Based on Liquid Exfoliated WS_2 as a Replacement for PEDOT:PSS," *Adv. Mater.*, vol. 31, no. 46, p. 1902965, 2019. (see p. 18)

[57] Y. Yuan, G. Giri, A. L. Ayzner, A. P. Zoombelt, S. C. B. Mannsfeld, J. Chen, D. Nordlund, M. F. Toney, J. Huang, and Z. Bao, "Ultra-high mobility transparent

organic thin film transistors grown by an off-centre spin-coating method," *Nat. Commun.*, vol. 5, no. 1, p. 3005, 2014. (see p. 19)

[58] J. Ajayan, D. Nirmal, P. Mohankumar, D. Kuriyan, A. S. A. Fletcher, L. Arivazhagan, and B. S. Kumar, "GaAs metamorphic high electron mobility transistors for future deep space-biomedical-millitary and communication system applications: A review," *Microelectronics J.*, vol. 92, p. 104604, 2019. (see p. 19)

[59] NREL, "Best Research-Cell Efficiency Chart," 2020. https://www.nrel.gov/pv/assets/pdfs/best-research-cell-efficiencies.20200406.pdf. (see p. 19)

[60] D. Luo, W. Yang, Z. Wang, A. Sadhanala, Q. Hu, R. Su, R. Shivanna, G. F. Trindade, J. F. Watts, Z. Xu, T. Liu, K. Chen, F. Ye, P. Wu, L. Zhao, J. Wu, Y. Tu, Y. Zhang, X. Yang, W. Zhang, R. H. Friend, Q. Gong, H. J. Snaith, and R. Zhu, "Enhanced photovoltage for inverted planar heterojunction perovskite solar cells," *Science*, vol. 360, no. 6396, pp. 1442–1446, 2018. (see p. 19)

[61] M. M. Tavakoli, W. Tress, J. V. Mili, D. Kubicki, L. Emsley, and M. Grtzel, "Addition of adamantylammonium iodide to hole transport layers enables highly efficient and electroluminescent perovskite solar cells," *Energy Environ. Sci.*, vol. 11, no. 11, pp. 3310–3320, 2018. (see p. 19)

[62] F. Bella, G. Griffini, J.-P. Correa-Baena, G. Saracco, M. Gratzel, A. Hagfeldt, S. Turri, and C. Gerbaldi, "Improving efficiency and stability of perovskite solar cells with photocurable fluoropolymers," *Science*, vol. 354, no. 6309, pp. 203–206, 2016. (see p. 19)

[63] K. Tanabe, D. Guimard, D. Bordel, R. Morihara, M. Nishioka, and Y. Arakawa, "High-efficiency InAs/GaAs quantum dot solar cells by MOCVD," in *2012 38th IEEE Photovoltaic Specialists Conference*, pp. 001929–001930, 2012-06. (see p. 19)

[64] S. Suraprapapich, S. Thainoi, S. Kanjanachuchai, and S. Panyakeow, "Quantum dot integration in heterostructure solar cells," *Sol. Energy Mater. Sol. Cells*, vol. 90, no. 18, pp. 2968–2974, 2006. (see p. 19)

[65] I. Moreels, K. Lambert, D. Smeets, D. De Muynck, T. Nollet, J. C. Martins, F. Vanhaecke, A. Vantomme, C. Delerue, G. Allan, and Z. Hens, "Size-Dependent Optical Properties of Colloidal PbS Quantum Dots," *ACS Nano*, vol. 3, no. 10, pp. 3023–3030, 2009. (see p. 19)

[66] X. Dai, Z. Zhang, Y. Jin, Y. Niu, H. Cao, X. Liang, L. Chen, J. Wang, and X. Peng, "Solution-processed, high-performance light-emitting diodes based on quantum dots," *Nature*, vol. 515, no. 7525, pp. 96–99, 2014. (see p. 20)

[67] V. Wood and V. Bulovi, "Colloidal quantum dot light-emitting devices," *Nano Reviews*, vol. 1, no. 1, p. 5202, 2010. (see p. 20)

[68] C. Dang, J. Lee, C. Breen, J. S. Steckel, S. Coe-Sullivan, and A. Nurmikko, "Red, green and blue lasing enabled by single-exciton gain in colloidal quantum dot films," *Nat. Nanotechnol.*, vol. 7, no. 5, pp. 335–339, 2012. (see p. 20)

[69] K. Roh, C. Dang, J. Lee, S. Chen, J. S. Steckel, S. Coe-Sullivan, and A. Nurmikko, "Surface-emitting red, green, and blue colloidal quantum dot distributed feedback lasers," *Opt. Express*, vol. 22, no. 15, p. 18800, 2014. (see p. 20)

[70] C. She, I. Fedin, D. S. Dolzhnikov, P. D. Dahlberg, G. S. Engel, R. D. Schaller, and D. V. Talapin, "Red, Yellow, Green, and Blue Amplified Spontaneous Emission and Lasing Using Colloidal CdSe Nanoplatelets," *ACS Nano*, vol. 9, no. 10, pp. 9475–9485, 2015. (see p. 20)

[71] Y. Bi, S. Pradhan, M. Z. Akgul, S. Gupta, A. Stavrinadis, J. Wang, and G. Konstantatos, "Colloidal Quantum Dot Tandem Solar Cells Using Chemical Vapor Deposited Graphene as an Atomically Thin Intermediate Recombination Layer," *ACS Energy Lett.*, vol. 3, no. 7, pp. 1753–1759, 2018. (see p. 20)

[72] J. Kim, O. Ouellette, O. Voznyy, M. Wei, J. Choi, M.-J. Choi, J. W. Jo, S.-W. Baek, J. Fan, M. I. Saidaminov, B. Sun, P. Li, D.-H. Nam, S. Hoogland, Z.-H. Lu, F. P. G. de Arquer, and E. H. Sargent, "Butylamine-Catalyzed Synthesis of Nanocrystal Inks Enables Efficient Infrared CQD Solar Cells," *Adv. Mater.*, vol. 30, no. 45, p. 1803830, 2018. (see pp. 20 and 39)

[73] Z. Yang, J. Z. Fan, A. H. Proppe, F. P. G. de Arquer, D. Rossouw, O. Voznyy, X. Lan, M. Liu, G. Walters, R. Quintero-Bermudez, B. Sun, S. Hoogland, G. A. Botton, S. O. Kelley, and E. H. Sargent, "Mixed-quantum-dot solar cells," *Nat. Commun.*, vol. 8, no. 1, p. 1325, 2017. (see pp. 20 and 71)

[74] S.-Y. Bae, S. Y. Lee, J.-w. Kim, H. N. Umh, J. Jeong, S. Bae, J. Yi, Y. Kim, and J. Choi, "Hazard potential of perovskite solar cell technology for potential implementation of safe-by-design approach," *Sci. Rep*, vol. 9, no. 1, p. 4242, 2019. (see p. 20)

[75] Y. G. Yoo, J. Park, H. N. Umh, S. Y. Lee, S. Bae, Y. H. Kim, S. E. Jerng, Y. Kim, and J. Yi, "Evaluating the environmental impact of the lead species in

perovskite solar cells via environmental-fate modeling," *J Ind Eng Chem.*, vol. 70, pp. 453–461, 2019. (see pp. 20 and 27)

[76] X. Wang, S. Wang, Y. Xie, Y. Jiao, J. Liu, X. Wang, W. Zhou, Z. Xing, and K. Pan, "Facet-Dependent SnS Nanocrystals as the High-Performance Counter Electrode Materials for Dye-Sensitized Solar Cells," *ACS Sustain. Chem. Eng.*, vol. 7, no. 17, pp. 14353–14360, 2019. (see p. 20)

[77] E. Jokar, C.-H. Chien, C.-M. Tsai, A. Fathi, and E. W.-G. Diau, "Robust Tin-Based Perovskite Solar Cells with Hybrid Organic Cations to Attain Efficiency Approaching 10%," *Adv. Mater.*, vol. 31, no. 2, p. 1804835, 2019. (see p. 20)

[78] J. Li, C. C. Stoumpos, G. G. Trimarchi, I. Chung, L. Mao, M. Chen, M. R. Wasielewski, L. Wang, and M. G. Kanatzidis, "Air-Stable Direct Bandgap Perovskite Semiconductors: All-Inorganic Tin-Based Heteroleptic Halides AxSnClyIz (A = Cs, Rb)," *Chem. Mater*, vol. 30, no. 14, pp. 4847–4856, 2018. (see p. 20)

[79] Q. Tai, X. Guo, G. Tang, P. You, T.-W. Ng, D. Shen, J. Cao, C.-K. Liu, N. Wang, Y. Zhu, C.-S. Lee, and F. Yan, "Antioxidant Grain Passivation for AirStable TinBased Perovskite Solar Cells," *Angew. Chem. Int. Ed.*, vol. 58, no. 3, pp. 806–810, 2019. (see p. 20)

[80] M. Chen, M.-G. Ju, H. F. Garces, A. D. Carl, L. K. Ono, Z. Hawash, Y. Zhang, T. Shen, Y. Qi, R. L. Grimm, D. Pacifici, X. C. Zeng, Y. Zhou, and N. P. Padture, "Highly stable and efficient all-inorganic lead-free perovskite solar cells with native-oxide passivation," *Nat. Commun.*, vol. 10, no. 16, p. 16, 2019. (see p. 20)

[81] A. Wang, X. Yan, M. Zhang, S. Sun, M. Yang, W. Shen, X. Pan, P. Wang, and Z. Deng, "Controlled Synthesis of Lead-Free and Stable Perovskite Derivative Cs_2SnI_6 Nanocrystals via a Facile Hot-Injection Process," *Chem. Mater.*, vol. 28, no. 22, pp. 8132–8140, 2016. (see p. 20)

[82] H. McDaniel, N. Fuke, J. M. Pietryga, and V. I. Klimov, "Engineered $CuInSe_xS_{2x}$ Quantum Dots for Sensitized Solar Cells," *J. Phys. Chem. Lett.*, vol. 4, no. 3, pp. 355–361, 2013. (see pp. 20 and 27)

[83] D. Aldakov, A. Lefranois, and P. Reiss, "Ternary and quaternary metal chalcogenide nanocrystals: Synthesis, properties and applications," *J. Mater. Chem. C*, vol. 1, no. 24, p. 3756, 2013. (see p. 20)

[84] J. E. Halpert, F. S. F. Morgenstern, B. Ehrler, Y. Vaynzof, D. Credgington, and N. C. Greenham, "Charge Dynamics in Solution-Processed Nanocrystalline $CuInS_2$ Solar Cells," *ACS Nano*, vol. 9, no. 6, pp. 5857–5867, 2015. (see p. 20)

[85] L. Li, N. Coates, and D. Moses, "Solution-Processed Inorganic Solar Cell Based on in Situ Synthesis and Film Deposition of $CuInS_2$ Nanocrystals," *J. Am. Chem. Soc.*, vol. 132, no. 1, pp. 22–23, 2010. (see p. 20)

[86] Y. Cao, M. S. Denny, J. V. Caspar, W. E. Farneth, Q. Guo, A. S. Ionkin, L. K. Johnson, M. Lu, I. Malajovich, D. Radu, H. D. Rosenfeld, K. R. Choudhury, and W. Wu, "High-Efficiency Solution-Processed $Cu_2ZnSn(S,Se)_4$ Thin-Film Solar Cells Prepared from Binary and Ternary Nanoparticles," *J. Am. Chem. Soc.*, vol. 134, no. 38, pp. 15644–15647, 2012. (see p. 20)

[87] J. Du, Z. Du, J.-S. Hu, Z. Pan, Q. Shen, J. Sun, D. Long, H. Dong, L. Sun, X. Zhong, and L.-J. Wan, "ZnCuInSe Quantum Dot Solar Cells with a Certified Power Conversion Efficiency of 11.6%," *J. Am. Chem. Soc.*, vol. 138, no. 12, pp. 4201–4209, 2016. (see p. 20)

[88] A. de Kergommeaux, A. Fiore, N. Bruyant, F. Chandezon, P. Reiss, A. Pron, R. de Bettignies, and J. Faure-Vincent, "Synthesis of colloidal $CuInSe_2$ nanocrystals films for photovoltaic applications," *Sol. Energy Mater Sol.*, vol. 95, pp. S39–S43, 2011. (see p. 20)

[89] C. Rein, S. Engberg, and J. Andreasen, "Stable, carbon-free inks of Cu_2ZnSnS_4 nanoparticles synthesized at room temperature designed for roll-to-roll fabrication of solar cell absorber layers," *J. Alloys Compd*, vol. 787, pp. 63–71, 2019. (see p. 21)

[90] J. Xu, Z. Hu, J. Zhang, W. Xiong, L. Sun, L. Wan, R. Zhou, Y. Jiang, and C.-S. Lee, "Cu_2ZnSnS_4 and $Cu_2ZnSn(S_{1-x}Se_x)_4$ nanocrystals: Room-temperature synthesis and efficient photoelectrochemical water splitting," *J. Mater. Chem. A*, vol. 5, no. 48, pp. 25230–25236, 2017. (see p. 21)

[91] Y. Liu, M. Liu, D. Yin, D. Zhu, and M. T. Swihart, "A general and rapid room-temperature synthesis approach for metal sulphide nanocrystals with tunable properties," *Nanoscale*, vol. 11, no. 1, pp. 136–144, 2019. (see p. 21)

[92] Y. Hwang, B.-I. Park, B.-S. Lee, J. Y. Kim, J.-H. Jeong, H. Kim, M. J. Ko, B. Kim, H. J. Son, S. Y. Lee, J.-S. Lee, J.-K. Park, S.-H. Cho, and D.-K. Lee, "Influences of Extended Selenization on $Cu_2ZnSnSe_4$ Solar Cells Prepared from Quaternary Nanocrystal Ink," *J. Phys. Chem. C*, vol. 118, no. 48, pp. 27657–27663, 2014. (see p. 21)

[93] Q. Guo, G. M. Ford, W.-C. Yang, B. C. Walker, E. A. Stach, H. W. Hillhouse, and R. Agrawal, "Fabrication of 7.2% Efficient CZTSSe Solar Cells Using CZTS

Nanocrystals," *J. Am. Chem. Soc.*, vol. 132, no. 49, pp. 17384–17386, 2010. (see p. 21)

[94] Y. Qu, G. Zoppi, and N. S. Beattie, "The role of nanoparticle inks in determining the performance of solution processed $Cu_2ZnSn(S,Se)_4$ thin film solar cells," *Prog Photovolt*, vol. 24, no. 6, pp. 836–845, 2016. (see p. 21)

[95] G. M. Ford, Q. Guo, R. Agrawal, and H. W. Hillhouse, "$CuIn(S,Se)_2$ thin film solar cells from nanocrystal inks: Effect of nanocrystal precursors," *Thin Solid Films*, vol. 520, no. 1, pp. 523–528, 2011. (see p. 21)

[96] J. van Embden, A. S. R. Chesman, and J. J. Jasieniak, "The Heat-Up Synthesis of Colloidal Nanocrystals," *Chem. Mater.*, vol. 27, no. 7, pp. 2246–2285, 2015. (see p. 21)

[97] X. Wang, J. Zhuang, Q. Peng, and Y. Li, "A general strategy for nanocrystal synthesis," *Nature*, vol. 437, no. 7055, pp. 121–124, 2005. (see p. 21)

[98] J. Deng, H. Wang, J. Xun, J. Wang, X. Yang, W. Shen, M. Li, and R. He, "Room-temperature synthesis of excellent-performance $CsPb_{1-x}Sn_xBr_3$ perovskite quantum dots and application in light emitting diodes," *Mater. Des.*, vol. 185, p. 108246, 2020. (see p. 21)

[99] F. Di Stasio, S. Christodoulou, N. Huo, and G. Konstantatos, "Near-Unity Photoluminescence Quantum Yield in $CsPbBr_3$ Nanocrystal Solid-State Films via Postsynthesis Treatment with Lead Bromide," *Chem. Mater.*, vol. 29, no. 18, pp. 7663–7667, 2017. (see p. 21)

[100] N. M. Abdelazim, Q. Zhu, Y. Xiong, Y. Zhu, M. Chen, N. Zhao, S. V. Kershaw, and A. L. Rogach, "Room Temperature Synthesis of HgTe Quantum Dots in an Aprotic Solvent Realizing High Photoluminescence Quantum Yields in the Infrared," *Chem. Mat.*, vol. 29, no. 18, pp. 7859–7867, 2017. (see p. 21)

[101] Y. Wang, Z. Liu, N. Huo, F. Li, M. Gu, X. Ling, Y. Zhang, K. Lu, L. Han, H. Fang, A. G. Shulga, Y. Xue, S. Zhou, F. Yang, X. Tang, J. Zheng, M. Antonietta Loi, G. Konstantatos, and W. Ma, "Room-temperature direct synthesis of semi-conductive PbS nanocrystal inks for optoelectronic applications," *Nat. Commun.*, vol. 10, no. 1, p. 5136, 2019. (see p. 21)

[102] O. M. Primera-Pedrozo, Z. Arslan, B. Rasulev, and J. Leszczynski, "Room temperature synthesis of PbSe quantum dots in aqueous solution: Stabilization by interactions with ligands," *Nanoscale*, vol. 4, no. 4, p. 1312, 2012. (see p. 21)

[103] H. Lu and R. L. Brutchey, "Tunable Room-Temperature Synthesis of Coinage Metal Chalcogenide Nanocrystals from *N* -Heterocyclic Carbene Synthons," *Chem. Mater*, vol. 29, no. 3, pp. 1396–1403, 2017. (see p. 21)

[104] W. Wang, Y. Geng, P. Yan, F. Liu, Y. Xie, and Y. Qian, "A Novel Mild Route to Nanocrystalline Selenides at Room Temperature," *J. Am. Chem. Soc.*, vol. 121, no. 16, pp. 4062–4063, 1999. (see p. 21)

[105] S. K. Saha, A. Guchhait, and A. J. Pal, "Cu_2ZnSnS_4 (CZTS) nanoparticle based nontoxic and earth-abundant hybrid pn-junction solar cells," *Phys. Chem. Chem. Phys*, vol. 14, no. 22, p. 8090, 2012. (see p. 22)

[106] D. So, S. Pradhan, and G. Konstantatos, "Solid-state colloidal $CuInS_2$ quantum dot solar cells enabled by bulk heterojunctions," *Nanoscale*, vol. 8, no. 37, pp. 16776–16785, 2016. (see p. 22)

[107] N. Reilly, M. Wehrung, R. A. O'Dell, and L. Sun, "Ultrasmall colloidal PbS quantum dots," *Mater. Chem. Phys*, vol. 147, no. 1, pp. 1–4, 2014. (see p. 22)

[108] N. Gaponik, D. V. Talapin, A. L. Rogach, K. Hoppe, E. V. Shevchenko, A. Kornowski, A. Eychmller, and H. Weller, "Thiol-Capping of CdTe Nanocrystals: An Alternative to Organometallic Synthetic Routes," *J. Phys. Chem. B*, vol. 106, no. 29, pp. 7177–7185, 2002. (see p. 22)

[109] Y. Zheng, Z. Yang, and J. Y. Ying, "Aqueous Synthesis of Glutathione-Capped ZnSe and $Zn_{1-x}Cd_xSe$ Alloyed Quantum Dots," *Adv. Mater.*, vol. 19, no. 11, pp. 1475–1479, 2007. (see pp. 22 and 75)

[110] M. Bernechea, N. C. Miller, G. Xercavins, D. So, A. Stavrinadis, and G. Konstantatos, "Solution-processed solar cells based on environmentally friendly $AgBiS_2$ nanocrystals," *Nat. Photonics*, vol. 10, no. 8, pp. 521–525, 2016. (see pp. 27, 31, 39, 43, 44, 45, 51, 52, 55, 59, 71, 85, and 87)

[111] J. Jean, J. Xiao, R. Nick, N. Moody, M. Nasilowski, M. Bawendi, and V. Bulovi, "Synthesis cost dictates the commercial viability of lead sulfide and perovskite quantum dot photovoltaics," *Energy Environ. Sci.*, vol. 11, no. 9, pp. 2295–2305, 2018. (see p. 27)

[112] J. T. Oh, S. Y. Bae, S. R. Ha, H. Cho, S. J. Lim, D. W. Boukhvalov, Y. Kim, and H. Choi, "Water-resistant $AgBiS_2$ colloidal nanocrystal solids for eco-friendly thin film photovoltaics," *Nanoscale*, vol. 11, no. 19, pp. 9633–9640, 2019. (see p. 28)

[113] P. Lei, R. An, X. Zheng, P. Zhang, K. Du, M. Zhang, L. Dong, X. Gao, J. Feng, and H. Zhang, "Ultrafast synthesis of ultrasmall polyethylenimine-protected $AgBiS_2$ nanodots by rookie method for *in vivo* dual-modal CT/PA imaging and simultaneous photothermal therapy," *Nanoscale*, vol. 10, no. 35, pp. 16765–16774, 2018. (see pp. 28 and 29)

[114] C. H. Mak, J. Qian, L. Roge, W. K. Lai, and S. P. Lau, "Facile synthesis of $AgBiS_2$ nanocrystals for high responsivity infrared detectors," *RSC Adv.*, vol. 8, no. 68, pp. 39203–39207, 2018. (see p. 28)

[115] J. Joo, H. B. Na, T. Yu, J. H. Yu, Y. W. Kim, F. Wu, J. Z. Zhang, and T. Hyeon, "Generalized and Facile Synthesis of Semiconducting Metal Sulfide Nanocrystals," *J. Am. Chem. Soc.*, vol. 125, no. 36, pp. 11100–11105, 2003. (see p. 28)

[116] X. Zhong, S. Liu, Z. Zhang, L. Li, Z. Wei, and W. Knoll, "Synthesis of high-quality CdS, ZnS, and $Zn_xCd_{1-x}S$ nanocrystals using metal salts and elemental sulfur," *J. Mater. Chem.*, vol. 14, no. 18, pp. 2790–2794, 2004. (see p. 28)

[117] D. M. Roberts, A. R. Landin, T. G. Ritter, J. D. Eaves, and C. R. Stoldt, "Nanocrystalline Iron Monosulfides Near Stoichiometry," *Sci. Rep.*, vol. 8, no. 6591, p. 6591, 2018. (see p. 28)

[118] P. O'Brien, D. J. Otway, and J. R. Walsh, "Novel precursors for the growth of a - In_2S_3: Trisdialkyldithiocarbamates of indium," *Thin Solid Films*, vol. 315, no. 1, pp. 57–61, 1998. (see p. 28)

[119] C. Wang, X. Zhang, X. Qian, W. Wang, and Y. Qian, "Ultrafine powder of silver sulfide semiconductor prepared in alcohol solution," *Mater. Res. Bull*, vol. 33, no. 7, pp. 1083–1086, 1998. (see p. 28)

[120] S. Liu, X. Qian, J. Yin, L. Hong, X. Wang, and Z. Zhu, "Synthesis and Characterization of Ag_2S Nanocrystals in Hyperbranched Polyurethane at Room Temperature," *Journal of Solid State Chemistry*, vol. 168, no. 1, pp. 259–262, 2002. (see p. 28)

[121] J. Yang and J. Y. Ying, "Room-temperature synthesis of nanocrystalline Ag_2S and its nanocomposites with gold," *ChemComm*, no. 22, pp. 3187–3189, 2009. (see p. 31)

[122] W. Zhang, "Synthesis of nanocrystalline Ag2S in aqueous solution," *Solid State Ion.*, vol. 130, no. 1-2, pp. 111–114, 2000. (see p. 31)

[123] H. Doh, S. Hwang, and S. Kim, "Size-Tunable Synthesis of Nearly Monodisperse Ag_2S Nanoparticles and Size-Dependent Fate of the Crystal Structures

upon Cation Exchange to $AgInS_2$ Nanoparticles," *Chem. Mater.*, vol. 28, no. 22, pp. 8123–8127, 2016. (see p. 31)

[124] P. Han, A. Mihi, J. Ferre-borrull, J. Pallars, and L. F. Marsal, "Interplay Between Morphology, Optical Properties, and Electronic Structure of Solution-Processed Bi_2S_3 Colloidal Nanocrystals," *J. Phys. Chem. C*, vol. 119, no. 19, pp. 10693–10699, 2015. (see p. 31)

[125] J. Wang, L. Li, H. Yu, F. Guan, and D. Wang, "BinaryTernary $Bi_2S_3AgBiS_2$ Rod-to-Rod Transformation via Anisotropic Partial Cation Exchange Reaction," *Inorg. Chem.*, vol. 58, no. 19, pp. 12998–13006, 2019. (see p. 31)

[126] M. Chen, Y.-G. Feng, X. Wang, T.-C. Li, J.-Y. Zhang, and D.-J. Qian, "Silver Nanoparticles Capped by Oleylamine: Formation, Growth, and Self-Organization," *Langmuir*, vol. 23, no. 10, pp. 5296–5304, 2007. (see p. 33)

[127] M. Yamamoto, Y. Kashiwagi, and M. Nakamoto, "Size-Controlled Synthesis of Monodispersed Silver Nanoparticles Capped by Long-Chain Alkyl Carboxylates from Silver Carboxylate and Tertiary Amine," *Langmuir*, vol. 22, no. 20, pp. 8581–8586, 2006. (see p. 33)

[128] I. C. Baek, S. I. Seok, N. C. Pramanik, S. Jana, M. A. Lim, B. Y. Ahn, C. J. Lee, and Y. J. Jeong, "Ligand-dependent particle size control of PbSe quantum dots," *J. Colloid Interface Sci.*, vol. 310, no. 1, pp. 163–166, 2007. (see p. 35)

[129] J. W. Thomson, K. Nagashima, P. M. Macdonald, and G. A. Ozin, "From Sulfur-Amine Solutions to Metal Sulfide Nanocrystals: Peering into the Oleylamine-Sulfur Black Box," *J. Am. Chem. Soc.*, vol. 133, pp. 5036–5041, 2011. (see p. 39)

[130] S. Nagakura, "Molecular Complexes and their Spectra. VIII. The Molecular Complex between Iodine and Triethylamine," *J. Am. Chem. Soc.*, vol. 80, no. 3, pp. 520–524, 1958. (see p. 39)

[131] N. Ahn, D.-Y. Son, I.-H. Jang, S. M. Kang, M. Choi, and N.-G. Park, "Highly Reproducible Perovskite Solar Cells with Average Efficiency of 18.3% and Best Efficiency of 19.7% Fabricated via Lewis Base Adduct of Lead(II) Iodide," *J. Am. Chem. Soc.*, vol. 137, no. 27, pp. 8696–8699, 2015. (see p. 39)

[132] H. Yada, J. Tanaka, and S. Nagakura, "Charge-transfer Complexes between Iodine and Various Aliphatic Amines," *Bull. Chem. Soc. Jpn.*, vol. 33, no. 12, pp. 1660–1667, 1960. (see p. 40)

[133] V. Sayevich, C. Guhrenz, V. M. Dzhagan, M. Sin, M. Werheid, B. Cai, L. Borchardt, J. Widmer, D. R. Zahn, E. Brunner, V. Lesnyak, N. Gaponik, and A. Eychmller, "Hybrid *N* -Butylamine-Based Ligands for Switching the Colloidal Solubility and Regimentation of Inorganic-Capped Nanocrystals," *ACS Nano*, vol. 11, no. 2, pp. 1559–1571, 2017. (see p. 45)

[134] W. Fu, Y. Shi, W. Qiu, L. Wang, Y. Nan, M. Shi, H. Li, and H. Chen, "High efficiency hybrid solar cells using post-deposition ligand exchange by monothiols," *Phys. Chem. Chem. Phys.*, vol. 14, no. 35, pp. 12094–12098, 2012. (see p. 45)

[135] P. Reiss, M. Protire, and L. Li, "Core/Shell Semiconductor Nanocrystals," *Small*, vol. 5, no. 2, pp. 154–168, 2009. (see p. 47)

[136] N. Gaponik, "Assemblies of thiol-capped nanocrystals as building blocks for use in nanotechnology," *J. Mater. Chem.*, vol. 20, no. 25, p. 5174, 2010. (see p. 48)

[137] A. L. Rogach, A. Kornowski, M. Gao, A. Eychmller, and H. Weller, "Synthesis and Characterization of a Size Series of Extremely Small Thiol-Stabilized CdSe Nanocrystals," *J. Phys. Chem. B*, vol. 103, no. 16, pp. 3065–3069, 1999. (see p. 48)

[138] D. A. R. Barkhouse, A. G. Pattantyus-Abraham, L. Levina, and E. H. Sargent, "Thiols Passivate Recombination Centers in Colloidal Quantum Dots Leading to Enhanced Photovoltaic Device Efficiency," *ACS Nano*, vol. 2, no. 11, pp. 2356–2362, 2008. (see p. 48)

[139] K. S. Jeong, J. Tang, H. Liu, J. Kim, A. W. Schaefer, K. Kemp, L. Levina, X. Wang, S. Hoogland, R. Debnath, L. Brzozowski, E. H. Sargent, and J. B. Asbury, "Enhanced Mobility-Lifetime Products in PbS Colloidal Quantum Dot Photovoltaics," *ACS Nano*, vol. 6, no. 1, pp. 89–99, 2012. (see p. 48)

[140] S. Pradhan, A. Stavrinadis, S. Gupta, Y. Bi, F. D. Stasio, and G. Konstantatos, "Trap-State Suppression and Improved Charge Transport in PbS Quantum Dot Solar Cells with Synergistic Mixed-Ligand Treatments," *Small*, vol. 13, no. 21, p. 1700598, 2017. (see pp. 48 and 51)

[141] S. K. Coulter, M. P. Schwartz, and R. J. Hamers, "Sulfur Atoms as Tethers for Selective Attachment of Aromatic Molecules to Silicon(001) Surfaces," *J. Phys. Chem. B*, vol. 105, no. 15, pp. 3079–3087, 2001. (see p. 50)

[142] T. Kirchartz, F. Deledalle, P. S. Tuladhar, J. R. Durrant, and J. Nelson, "On the Differences between Dark and Light Ideality Factor in Polymer:Fullerene Solar Cells," *J. Phys. Chem. Lett.*, vol. 4, no. 14, pp. 2371–2376, 2013. (see p. 59)

[143] S. R. Cowan, A. Roy, and A. J. Heeger, "Recombination in polymer-fullerene bulk heterojunction solar cells," *Physical review. B*, vol. 82, no. 24, 2010. (see p. 59)

[144] S. N. Guin, V. Srihari, and K. Biswas, "Promising thermoelectric performance in n-type $AgBiSe_2$: Effect of aliovalent anion doping," *J. Mater. Chem. A*, vol. 3, no. 2, pp. 648–655, 2015. (see p. 63)

[145] O. Yarema, M. Yarema, A. Moser, O. Enger, and V. Wood, "Composition- and Size-Controlled IVVI Semiconductor Nanocrystals," *Chem. Mater.*, vol. 32, no. 5, pp. 2078–2085, 2020. (see pp. 63 and 65)

[146] A. Das, B. Hsu, A. Shamirian, Z. Yang, and P. T. Snee, "Synthesis of High-Quality $AgSbSe_2$ and $AgBiSe_2$ Nanocrystals with Antimony and Bismuth Silylamide Reagents," *Chem. Mater.*, vol. 29, no. 10, pp. 4597–4602, 2017. (see pp. 63, 65, and 76)

[147] Y. Yang, D. Pan, Z. Zhang, T. Chen, H. Xie, J. Gao, and X. Guo, "Ag_2Se quantum dots for photovoltaic applications and ligand effects on device performance," *J. Alloys Compd.*, vol. 766, pp. 925–932, 2018. (see p. 63)

[148] Y. Ding, Y. Qiu, K. Cai, Q. Yao, S. Chen, L. Chen, and J. He, "High performance n-type Ag_2Se film on nylon membrane for flexible thermoelectric power generator," *Nat. Commun.*, vol. 10, no. 1, 2019. (see p. 63)

[149] H. Zhang, X. Zhang, C. Liu, S.-T. Lee, and J. Jie, "High-Responsivity, High-Detectivity, Ultrafast Topological Insulator Bi_2Se_3/Silicon Heterostructure Broadband Photodetectors," *ACS Nano*, vol. 10, no. 5, pp. 5113–5122, 2016. (see p. 63)

[150] H. Xie, Z. Li, Z. Sun, J. Shao, X.-F. Yu, Z. Guo, J. Wang, Q. Xiao, H. Wang, Q.-Q. Wang, H. Zhang, and P. K. Chu, "Metabolizable Ultrathin Bi_2Se_3 Nanosheets in Imaging-Guided Photothermal Therapy," *Small*, vol. 12, no. 30, pp. 4136–4145, 2016. (see p. 63)

[151] C.-N. Zhu, G. Chen, Z.-Q. Tian, W. Wang, W.-Q. Zhong, Z. Li, Z.-L. Zhang, and D.-W. Pang, "Near-Infrared Fluorescent $Ag_2SeCetuximab$ Nanoprobes for Targeted Imaging and Therapy of Cancer," *Small*, vol. 13, no. 3, p. 1602309, 2017. (see p. 63)

[152] F. Wang, L. Li, W. Huang, L. Li, B. Jin, H. Li, and T. Zhai, "Submillimeter 2D Bi_2Se_3 Flakes toward High-Performance Infrared Photodetection at Optical

Communication Wavelength," *Adv. Funct. Mater*, vol. 28, no. 33, p. 1802707, 2018. (see p. 63)

[153] J.-Y. Zhao, G. Chen, Y.-P. Gu, R. Cui, Z.-L. Zhang, Z.-L. Yu, B. Tang, Y.-F. Zhao, and D.-W. Pang, "Ultrasmall Magnetically Engineered Ag_2Se Quantum Dots for Instant Efficient Labeling and Whole-Body High-Resolution Multimodal Real-Time Tracking of Cell-Derived Microvesicles," *J. Am. Chem. Soc.*, vol. 138, no. 6, pp. 1893–1903, 2016. (see p. 63)

[154] C. Xiao, J. Xu, B. Cao, K. Li, M. Kong, and Y. Xie, "Solid-Solutioned Homojunction Nanoplates with Disordered Lattice: A Promising Approach toward Phonon Glass Electron Crystal Thermoelectric Materials," *J. Am. Chem. Soc.*, vol. 134, no. 18, pp. 7971–7977, 2012. (see p. 63)

[155] L. Pan, D. Brardan, and N. Dragoe, "High Thermoelectric Properties of n-Type $AgBiSe_2$," *J. Am. Chem. Soc.*, vol. 135, no. 13, pp. 4914–4917, 2013. (see p. 63)

[156] F. Bcher, S. P. Culver, J. Peilstcker, K. S. Weldert, and W. G. Zeier, "Vacancy and anti-site disorder scattering in $AgBiSe_2$ thermoelectrics," *Dalton Trans.*, vol. 46, no. 12, pp. 3906–3914, 2017. (see p. 63)

[157] H.-J. Wu, P.-C. Wei, H.-Y. Cheng, J.-R. Deng, and Y.-Y. Chen, "Ultralow thermal conductivity in n-type Ge-doped $AgBiSe_2$ thermoelectric materials," *Acta Mater.*, vol. 141, pp. 217–229, 2017. (see p. 63)

[158] X. Liu, D. Jin, and X. Liang, "Enhanced thermoelectric performance of n-type transformable $AgBiSe_2$ polymorphs by indium doping," *Applied Physics Letters*, vol. 109, no. 13, p. 133901, 2016. (see p. 63)

[159] Y. Goto, A. Nishida, H. Nishiate, M. Murata, C. H. Lee, A. Miura, C. Moriyoshi, Y. Kuroiwa, and Y. Mizuguchi, "Effect of Te substitution on crystal structure and transport properties of $AgBiSe_2$ thermoelectric material," *Dalton Trans.*, vol. 47, no. 8, pp. 2575–2580, 2018. (see p. 63)

[160] C. Xiao, X. Qin, J. Zhang, R. An, J. Xu, K. Li, B. Cao, J. Yang, B. Ye, and Y. Xie, "High Thermoelectric and Reversible *p-n-p* Conduction Type Switching Integrated in Dimetal Chalcogenide," *J. Am. Chem. Soc.*, vol. 134, no. 44, pp. 18460–18466, 2012. (see pp. 63 and 70)

[161] D. Pan, Q. Wang, S. Jiang, X. Ji, and L. An, "Low-Temperature Synthesis of Oil-Soluble CdSe, CdS, and CdSe/CdS Core-Shell Nanocrystals by Using Various Water-Soluble Anion Precursors," *J. Phys. Chem. C*, vol. 111, no. 15, pp. 5661–5666, 2007. (see p. 64)

[162] P. M. Allen and M. G. Bawendi, "Ternary I-III-VI Quantum Dots Luminescent in the Red to Near-Infrared," *J. Am. Chem. Soc.*, vol. 130, no. 29, pp. 9240–9241, 2008. (see p. 64)

[163] Y. Jiang, W.-S. Ojo, B. Mahler, X. Xu, B. Abcassis, and B. Dubertret, "Synthesis of CdSe Nanoplatelets without Short-Chain Ligands: Implication for Their Growth Mechanisms," *ACS Omega*, vol. 3, no. 6, pp. 6199–6205, 2018. (see p. 64)

[164] A. Polovitsyn, A. H. Khan, I. Angeloni, J. Q. Grim, J. Planelles, J. I. Climente, and I. Moreels, "Synthesis of Anisotropic CdSe/CdS Dot-in-Giant-Rod Nanocrystals with Persistent Blue-Shifted Biexciton Emission," *ACS Photonics*, vol. 5, no. 11, pp. 4561–4568, 2018. (see p. 64)

[165] N. Pradhan and X. Peng, "Efficient and Color-Tunable Mn-Doped ZnSe Nanocrystal Emitters: Control of Optical Performance via Greener Synthetic Chemistry," *J. Am. Chem. Soc.*, vol. 129, no. 11, pp. 3339–3347, 2007. (see p. 64)

[166] P. D. Cozzoli, L. Manna, M. L. Curri, S. Kudera, C. Giannini, M. Striccoli, and A. Agostiano, "Shape and Phase Control of Colloidal ZnSe Nanocrystals," *Chem. Mater.*, vol. 17, no. 6, pp. 1296–1306, 2005. (see p. 64)

[167] Y. Wei, J. Yang, A. W. H. Lin, and J. Y. Ying, "Highly Reactive Se Precursor for the Phosphine-Free Synthesis of Metal Selenide Nanocrystals," *Chem. Mater.*, vol. 22, no. 20, pp. 5672–5677, 2010. (see p. 64)

[168] Y. Liu, D. Yao, L. Shen, H. Zhang, X. Zhang, and B. Yang, "Alkylthiol-Enabled Se Powder Dissolution in Oleylamine at Room Temperature for the Phosphine-Free Synthesis of Copper-Based Quaternary Selenide Nanocrystals," *Journal of the American Chemical Society*, vol. 134, no. 17, pp. 7207–7210, 2012. (see pp. 64, 65, 66, and 67)

[169] M. Z. Akgul, A. Figueroba, S. Pradhan, Y. Bi, and G. Konstantatos, "Low-Cost RoHS Compliant Solution Processed Photovoltaics Enabled by Ambient Condition Synthesis of $AgBiS_2$ Nanocrystals," *ACS Photonics*, vol. 7, no. 3, pp. 588–595, 2020. (see pp. 65 and 71)

[170] R. G. Pearson, "Hard and Soft Acids and Bases," *J. Am. Chem. Soc.*, vol. 85, no. 22, p. 7, 1963. (see p. 66)

[171] Y. Cui, A. Abouimrane, J. Lu, T. Bolin, Y. Ren, W. Weng, C. Sun, V. A. Maroni, S. M. Heald, and K. Amine, "(De)Lithiation Mechanism of Li/SeS_x ($x =$ 07) Batteries Determined by in Situ Synchrotron X-ray Diffraction and X-ray

Absorption Spectroscopy," *J. Am. Chem. Soc.*, vol. 135, no. 21, pp. 8047–8056, 2013. (see p. 70)

[172] Y. Bi, S. Pradhan, S. Gupta, M. Z. Akgul, A. Stavrinadis, and G. Konstantatos, "Infrared Solution-Processed Quantum Dot Solar Cells Reaching External Quantum Efficiency of 80 % at 1.35 {m} and Jsc in Excess of 34 mA cm-2," *Adv. Mater.*, vol. 30, no. 7, p. 1704928, 2018. (see p. 71)

[173] S. N. Guin, S. Banerjee, D. Sanyal, S. K. Pati, and K. Biswas, "Nanoscale Stabilization of Nonequilibrium Rock Salt BiAgSeS: Colloidal Synthesis and Temperature Driven Unusual Phase Transition," *Chem. Mater.*, vol. 29, no. 8, pp. 3769–3777, 2017. (see pp. 73 and 76)

[174] O. Chen, X. Chen, Y. Yang, J. Lynch, H. Wu, J. Zhuang, and Y. C. Cao, "Synthesis of MetalSelenide Nanocrystals Using Selenium Dioxide as the Selenium Precursor," *Angew. Chem. Int. Ed.*, vol. 47, no. 45, pp. 8638–8641, 2008. (see p. 75)

[175] M. V. Kovalenko, E. Kaufmann, D. Pachinger, J. Roither, M. Huber, J. Stangl, G. Hesser, F. Schffler, and W. Heiss, "Colloidal HgTe Nanocrystals with Widely Tunable Narrow Band Gap Energies: From Telecommunications to Molecular Vibrations," *J. Am. Chem. Soc.*, vol. 128, no. 11, pp. 3516–3517, 2006. (see p. 75)

[176] A. L. Rogach, T. Franzl, T. A. Klar, J. Feldmann, N. Gaponik, V. Lesnyak, A. Shavel, A. Eychmller, Y. P. Rakovich, and J. F. Donegan, "Aqueous Synthesis of Thiol-Capped CdTe Nanocrystals: State-of-the-Art," *J. Phys. Chem. C*, vol. 111, no. 40, pp. 14628–14637, 2007. (see p. 75)

[177] M. A. Hines and G. D. Scholes, "Colloidal PbS Nanocrystals with Size-Tunable Near-Infrared Emission: Observation of Post-Synthesis Self-Narrowing of the Particle Size Distribution," *Adv. Mater.*, vol. 15, no. 21, pp. 1844–1849, 2003. (see p. 75)

[178] D. Pan, D. Weng, X. Wang, Q. Xiao, W. Chen, C. Xu, Z. Yang, and Y. Lu, "Alloyed semiconductor nanocrystals with broad tunable band gaps," *ChemComm*, no. 28, pp. 4221–4223, 2009. (see p. 75)

[179] Y. C. Li, M. F. Ye, C. H. Yang, X. H. Li, and Y. F. Li, "Composition- and Shape-Controlled Synthesis and Optical Properties of $Zn_xCd_{1-x}S$ Alloyed Nanocrystals," *Adv. Funct. Mater*, vol. 15, no. 3, pp. 433–441, 2005. (see p. 75)

[180] W. H. Bragg and W. L. Bragg, "The reflection of X-rays by crystals," *Proc. R. Soc. Lond. A*, vol. 89, no. 610, p. 246, 1913. (see p. 76)

[181] S. Geller and J. H. Wernick, "Ternary semiconducting compounds with sodium chloride-like structure: $AgSbSe_2$, $AgSbTe_2$, $AgBiS_2$, $AgBiSe_2$," *Acta Cryst.*, vol. 12, no. 1, pp. 46–54, 1959. (see p. 76)

List of Publications

List of Publications

This thesis is based on the following works:

"Low-Cost RoHS Compliant Solution Processed Photovoltaics Enabled by Ambient Condition Synthesis of $AgBiS_2$ Nanocrystals"
M. Z. Akgul, A. Figueroba, S. Pradhan, Y. Bi, and G. Konstantatos
ACS Photonics, vol. 7, no. 3, pp. 588-595, 2020

"A Room-temperature Ambient Condition Synthesis Method enables Low-cost Quaternary $AgBiS_xSe_{2-x}$ Nanocrystals "
M. Z. Akgul, and G. Konstantatos, *in preparation.*

Other publications:

"Colloidal $AgBiS_2$ nanocrystals with reduced recombination yield 6.4 % power conversion efficiency in solution-processed solar cells"
I. Burgus-Ceballos, Y. Wang, M. Z. Akgul, and G. Konstantatos
Nano Energy, vol. 75, pp. 104961, 2020.

"Cation Disorder and Local Structural Distortions in $Ag_xBi_{1-x}S_2$ Nanoparticles"
J. Kopula Kesavan, F. dAcapito, P. Scardi, A. Stavrinadis, M. Z. Akgul, I. Burgus-Ceballos, G. Konstantatos, F. Boscherini
Nanomaterials, vol. 10, no. 2, pp. 316, 2020.

"Solution processed infrared- and thermo-photovoltaics based on 0.7 eV bandgap PbS colloidal quantum dots"
Y. Bi, A. Bertran, S. Gupta, I. Ramiro, S. Pradhan, S. Christodoulou, S.-Naidu Majji, M. Z. Akgul, and G. Konstantatos
Nanoscale, vol. 11, pp. 838-843, 2019.

"Colloidal quantum dot tandem solar cells using chemical vapor deposited graphene as an atomically thin intermediate recombination layer"
Y. Bi, S. Pradhan, M. Z. Akgul, S. Gupta, A. Stavrinadis, J. Wang, G. Konstantatos
ACS Energy Letters, vol. 3, no. 7, pp. 1753-1759, 2018

"Infrared SolutionProcessed Quantum Dot Solar Cells Reaching External Quantum Efficiency of 80 % at 1.35 μm and J_{SC} in Excess of 34 mA cm^{-2}"
Y. Bi, S. Pradhan, S. Gupta, M. Z. Akgul, A. Stavrinadis, G. Konstantatos
Advanced Materials, vol. 30, no. 7, pp. 1704928, 2018

"Low-temperature colloidal synthesis of $CuBiS_2$ nanocrystals for optoelectronic devices"
J. Wang, M. Z. Akgul, Y. Bi, S. Christodoulou, and G. Konstantatos
Journal of Materials Chemistry A, vol. 5, no. 47, pp. 24621-24625, 2017